IFP ENERGIES NOUVELLES **BTU COTTBUS-SENFTENBERG**

Large Eddy Simulations Modelling of Flameless Combustion

Von der Fakultät für Umweltwissenschaften und Verfahrenstechnik
der Brandenburgischen Technischen Universität Cottbus zur Erlangung des
akademischen Grades eines Doktor-Ingenieurs
genehmigte Dissertation

vorgelegt von

Diplom-Ingenieur

Carlo Locci
aus Cagliari (Italien)

Vorsitzender:	Prof. Dr. R.Herd
Gutachter:	Prof. Dr.-Ing. F.Mauss
Gutachter:	Prof. Dr.-Ing. L.Vervisch
IFPEN Supervisor:	Dr.-Ing. O.Colin

Tag der mündlichen Prüfung: 20. Juni 2014

Large Eddy Simulations Modelling of Flameless Combustion

Von der Fakultät für Umweltwissenschaften und Verfahrenstechnik
der Brandenburgischen Technischen Universität Cottbus zur Erlangung des
akademischen Grades eines Doktor-Ingenieurs
genehmigte Dissertation

vorgelegt von

Diplom-Ingenieur

Carlo Locci

aus Cagliari (Italien)

Vorsitzender:	Prof. Dr. R.Herd
Gutachter:	Prof. Dr.-Ing. F.Mauss
Gutachter:	Prof. Dr.-Ing. L.Vervisch
IFPEN Supervisor:	Dr.-Ing. O.Colin

Tag der mündlichen Prüfung: 20. Juni 2014

Acknowledgments

Everything in a Ph.D is about learning. So, the time to say a big *Thank You* to the people who have taught me something during the past 4 years has finally arrived.
First on the list: Olivier Colin. I had the chance of having him as a supervisor at IFPEN: during this time, he has been a precious, encouraging and constant guide. Not only he introduced me to the fine art of coding and combustion; he also instructed me to give effective presentations and, last but not the least, I am now able to speak in the language of Moliere with a weird mix of italian/parisien accent!
I would also wish to thank Prof. Fabian Mauss in the double role of thesis director and reviewer. Thank you very much for your competent remarks in the final phase of the manuscript review and for your numerous travels from Cottbus to Paris.
Thanks a lot also to the second reviewer of this work, Prof. Luc Vervisch; thank you a lot for having appreciated my works and for your competent remarks during my defense.
I would also like to thank Prof. Herd, Prof. Schmidt and Dr. Jehring for being part of the jury of my defense and for having read my manuscript.

Still on the IFPEN side, I would like to express my gratitude to Christian Angelberger, Scientific Director of the modeling department. I will say you thank you a thousand times for your careful attention in smoothing the administrative process during the last months.
Now, who says tabulated chemistry, says JB Michel! Thank you a lot for the technical help you've been able to give me and for your not-funny but brilliant jokes.
Thanks a lot also to Antonio Pires da Cruz for giving me the honor and pleasure of letting me being part of the department.
Of course, this thesis would not have been the same without my dear Ph.D colleagues. I really need to name all of you: Bejoy, Benjamin, Betty, Damien, Elias, Emre, Haifa, Hubert, JB May-Carle, Lama, Oguz, Sabre, Sophie, Stavros. And then the guys from the (in)famous CB/309: Adam (Thank you a lot for the farewell party and for your kindness!), Anthony (the draw against you is by far my best tennis performance of all time), Julien (Thank you for having introduced me to the AVBP code and for helping me out with Fortran at the beginning!), Nicolas (t'es un vrai rital..quoi dire de plus?), Stephane (Your jokes were as much brilliant as unexpected..bravo!).

Far from the CFD field, Thomas! Thanks a lot for reviewing the english of this manuscript. As for my M.Sc. thesis, you're once again responsible for any linguistic crime I might have committed.
And then a very special *Thank you* to a person so present during my Parisian years: Silvia! In these years, she's been very close to me sharing the same nostalgic moments when watching the *Squadra Azzurra*, sharing the same joys/disappointments typical of a Ph.D as well as the same love for the *Quartier Opera*. Only flaw: she's never been able to fully convince me about the superiority of the impressionist art compared to the italian *Rinascimento*. Who knows, one day I'll maybe prefer Monet to Michelangelo, but we are still quite far from that!
And finally, my parents and my sister. It has been so hard seeing them less than I would have wanted during these years. And yet, the sound of your voices at the phone was able to cheer me up during the un-productive moments. Questa tesi la dedico a voi.

Résumé

L'émergence environnementale a amené au développement de nouvelles technologies de combustion. Dans ce contexte, la combustion sans flamme (CsF) représente une technologie à la fois moins polluante et plus efficace. Dans la CsF, les gaz brulés sont fortement recirculés, permettant de réduire la teneur en oxygène et les pics de température, tout en réduisant les émissions d'oxydes d'azote. La CsF étant une technologie relativement nouvelle, son développement demande encore de la recherche et de l'optimisation, et nécessite donc d'importants investissements financiers. Potentiellement, les simulations numériques aux grandes échelles apparaissent comme un outil prometteur pour le développement de cette technologie. Cette thèse traite donc de la modélisation numérique de la CsF. Dans un premier temps, la CsF a été simulée en utilisant une nouvelle approche tabulée, qui utilise des réacteurs homogènes dilués (DHR). Le modèle, déjà exploité dans le contexte du projet EC-KIAI, a été adapté pour la CsF dans ce travail. Le modèle prend en compte les pertes d'enthalpie des gaz brulés sous adiabatiques ainsi que le mélange ternaire (carburant - air - gaz brulés). Cette approche a été d'abord validée sur une configuration académique, la Flamme D, et sur le bruleur de Verissimo pour la CsF dans un second temps. Dans la seconde partie de la thèse, un nouveau modèle de prédiction des NOx, DF-NORA, a été développé. La relaxation vers l'équilibre des taux de réaction dans une flammelette stationnaire est tabulée. Comme dans la première partie, le modèle a été validé sur la Flamme D et sur le brûleur de Verissimo. Les résultats encourageants de ce travail, ouvrent à la possibilité d'utiliser ces développements sur de vraies configurations industrielles.

Summary

The environmental emergency has led to the development of new combustion technologies. In this context, flameless combustion (FC in this manuscript) offers the prospect of a less polluting and more efficient technology. In FC, combustion is strongly diluted with recirculated burnt gases. Consequently the oxygen content is reduced and temperature peaks are smoothed, yielding reduced heat release. These conditions dramatically reduce the conditions of NO pollutant formation and increase the efficiency of the combustion process. Being FC a relatively new technology, it still needs optimization and R&D, which can be expensive and time consuming. Potentially, CFD can reduce both the financial costs as well as the R&D projects length. The context in which this thesis is inserted is exactly the numerical modeling of FC, by using Large Eddy Smulations for its better prediction of the turbulent ternary mixing (fuel - burnt gases -air), compared to RANS. This work has been divided into two main parts. In the first, combustion in FC has been investigated by means of a new tabulated combustion model initially written in the context of the EC-KIAI project and developed and adapted to FC in this thesis. The model uses diluted homogeneous reactors DHR to simulate FC and it was developed to account for under adiabatic enthalpy losses and the ternary mixing typical of FC. The model was firstly validated on a non-premixed flame academical configuration called Flame D and subsequently on a real FC combustor from the work of Verissimo et al. The results obtained for these configurations are quite correct although some discrepancies in CO prediction are observed. In the second part of the thesis, the NO pollutant modeling in FC is investigated. With this aim, the Diffusion Flame - NO relaxation approach DF-NORA was developed. It consists in tabulating the NO relaxation towards equilibrium of the NO source term in a flamelet structure. As done in the first part, the model was first validated on Flame D and then employed in a real FC configuration. Results are quite satisfactory in both configurations. The encouraging results obtained in this work open the possibility of applying the proposed developments to real industrial configurations in the future.

Contents

Contents

General context

1

1.1 Research on fossil fuels

1.1.1 Fossil fuel exploitation today

Most activities of modern societies rely on the availability of energy supplies. For example, transport, lighting and house heating are only a few of the human activities which require large amounts of energy. Historically, fossil fuels have represented the main supply for all these kind of activities. Furthermore, it is broadly acknowledged that the rapid development of western countries in the 20th century is due to the opportunities offered by fossil fuels. In Fig.1.1, from a report of the International Energy Agency of 2010, the world total primary energy supply evolution is shown from 1971 to 2008. It can be seen that 12267 Mtoe were supplied in the world in 2008. Of that quantity, 81.3% was from fossil fuels. Another key fact of Figure.1.1 is that world energy need is constantly increasing and so is fossil fuel demand. Energy portfolio are not the same for all countries. Fig.1.2 shows the energy supplies of USA, China and France, three countries belonging to the G8. The USA and China, the two largest energy consuming countries, report respectively an 83% and 93% energy supply share from fossil fuels. However, there exist some exceptions. For instance, France preferred to address its energy production towards nuclear technologies (Fig.1.2). Germany on the other hand, is making strong efforts to reduce its dependence on fossil fuels, trying its best to exploit renewable energy sources (in 2011 renewable resources in Germany topped a 20% quota in the energy mix of the country, as far as electricity consuming is concerned [2]). Apart from countries like France and Germany, it is evident that fossil fuels are more common and exploited than any other energy sources worldwide. It is also important to recall the reasons which have strongly favoured the spread of fossil fuels:

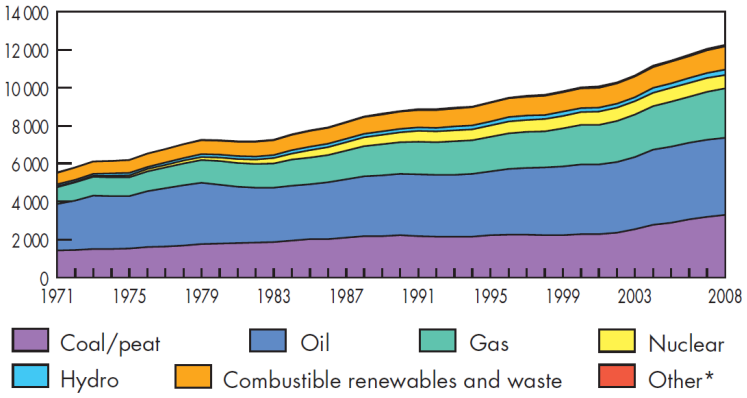

Figure 1.1 – *Evolution from 1971 to 2008 of world total primary energy supply by fuel (Mtoe) [1]*

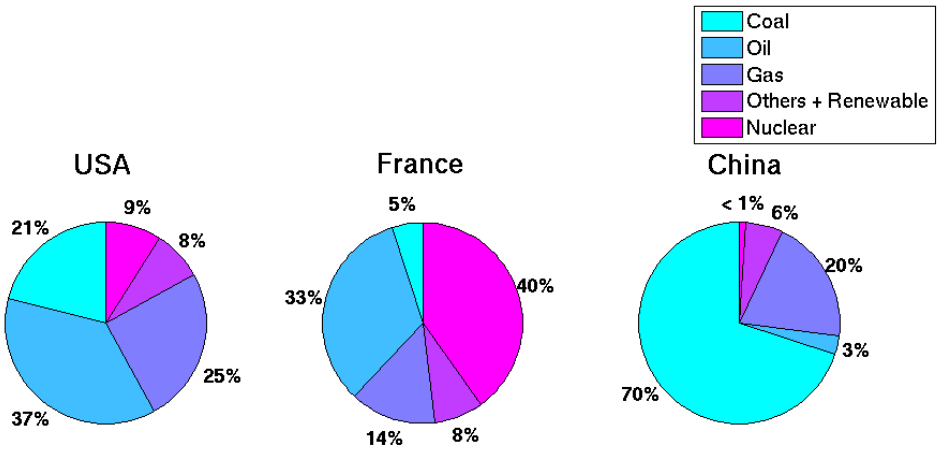

Figure 1.2 – *Share of the several energy sources for USA ([3]), France ([4]) and China [5]*

- Fossil fuels are abundant and they are present on almost every continent on the planet;
- Their abundance has also allowed their costs to be contained, allowing competitive prices in the energy market;
- Fossil fuels, above all in the case of the transport sector, offer a much higher energy density than other technologies like electrical vehicles;
- Still, in the transportation sector, fossil fuels such as liquid fuels are more practical and safer to transport. This is another reason for the success of fossil fuels in the transport sector, to the detriment of hydrogen as a fuel for instance. Today, hydrogen and plug-in electrical cars represent only a 5% share of the vehicle market [6];

On the other hand, there are several negative facets and aspects concerning fossil fuels. The controversies surrounding fossil fuels arise both form an economic and technological point of view:

- Greenhouse and global warming issues. It is the most negative aspect of fossil fuels. The main products (in mass) of fossil fuels combustion are CO_2 and H_2O. In particular, CO_2 is commonly considered as the main culprit in the average temperature increase of the planet [7]. With reference to figure 1.1, the energy demand is increasing. This leads to a still increasing emission of CO_2 in the atmosphere, then leading to global warming. Commonly the critical limit of CO_2 in the atmosphere is fixed at 550 ppm as declared in the Stern's report of 2007 [7]. Most likely, if no legislation and no remedies are put into effect, CO_2 will continue to increase as today and this limit will be reached in the near future.
- From an economic point of view, fossil fuels enjoy a monopoly in the energy market. Attempts to reduce this unfair competition, such as cap and trade or carbon tax solutions, were carried out but proved to be unsuccessful. In particular, if cap and trade solutions were successful in reducing NO_x and SO_x emissions, they ended up being less efficient in regulating carbon emissions [8].
- Fossil fuels are not clean technologies. As a matter of fact, soot, NO_x and SO_x are the main pollutants produced by fossil fuels which originate from the chemical reactions of fossil fuels combustion. Consequently, on smaller living scales such as metropolises and cities, these pollutants cause breathing issues and cancer [9].
- Fossil fuels do not meet the criteria for sustainable development. As a matter of fact, they still do not promise a long-lasting prosperity as they are going to disappear in 5-6 decades (oil and gas) or 2 centuries (coal).

If all these negative aspects exist and are now acknowledged, why does basing energy production on new forms of production such as renewable technologies seem to be such a difficult challenge? Many reasons exist:

- Neither nuclear nor renewable energies are at the present time capable of replacing 80% of energy supplied by fossil fuels;
- A possible solution to consume less fossil fuels, would be to produce less. If a country decided to produce less, this would certainly affect its economic development and result in economic collapse. This would be possible only in the case of a common agreement with other concurrent countries.
- If it is not easy to switch to other energy resources, the second way to reduce fossil fuels addiction would be to use the energy available in a more efficient and rational way. Many authors have theorized on these new approaches: one of the first examples was the concept of NegaWatt introduced by Lovins [10], where MegaWatts are not produced but rather saved (negatives Watts).

To conclude, humanity is confronting itself with a great challenge as far as energy is concerned. Nowadays, there is still a lot of uncertainty about the real potential of new technologies. Consequently, today's current situation can be resumed in these following points:

- for the moment, renewable energies are not exploitable on a large scale. their limits concern both technical and economic aspects [11];
- fossil fuels will continue to sustain human societies and prosperity until newer technologies are able to replace combustion based technologies;
- fossil fuels are threatening and are potentially dangerous for the eco-systems of the planet if we continue to use traditional technologies;
- as a consequence, it is mandatory to make fossil fuels technologies more efficient and less pollutant.

Now, several solutions are potentially available or almost ready to exploit. In section 1.1.2, some of these main new technologies for fossil fuels are presented.

1.1.2 Technologies to reduce pollutants and global warming

This section is dedicated to outlining some of the main fossil fuel based technologies for energy supply. In this sense, all the technologies for transportation will not be considered. As said in the previous section, for the future it is desirable to develop technologies which emit less CO_2. These two objectives might be achieved either by designing more efficient devices (which indirectly reduce the CO_2 per KWh produced) or by avoiding the emissions of CO_2 directly into the atmosphere (Carbon Capture and Storage technologies CCS).

More efficient technologies In this section, some of the more interesting technologies which can offer a more efficient way of burning fossil fuels, are described. They aim to reduce the specific emission of CO_2 per KWh.

- super critical power plants. This technology, which mainly uses coal, consists of new power plants with steam at temperatures up to $600^{\circ}C$. If compared to a traditional coal power plant, which efficiency is on the order of $35-40\%$, a super critical power plant can work with an efficiency up to 50%
- flameless combustion. Flameless combustion refers to a new type of combustion where the fuel burns with a strong burnt gas dilution and pre-heated air. This technology is known to be less pollutant and more efficient

- Combined cycle power plants. This technology combines a traditional power plant with a gas turbine. The residual heat from the gas turbine is recovered to heat water for domestic or industrial purposes. The combined cycles have an efficiency of 55% to 60%
- Biofuels. Biofuels represent a wide category of fuel obtained from living organisms, which exploit carbon fixation. Crops or algae are cultivated in order to obtain biomasses, which are then converted into biofuels. As plants absorb CO_2 during their life-cycle, these technologies have attracted much interest as they are considered CO_2 neutral. It is argued that the CO_2 is absorbed from the atmosphere and that an equivalent quantity is then released after combustion. Critics argue that this is not true as transportation and fertilization products in the production chain produce CO_2 and that biofuels are far from being CO_2 neutral [11].

Sequestration of CO_2 The second option to reduce the CO_2 in the atmosphere, is to avoid the direct emission of it. To do so, CO_2 should be separated from the final gases after combustion and then stored in an appropriate geological site. Three options are available:

- Separation of CO_2 from the exhaust gases. CO_2 is separated by means of chemical solvents from the exhaust gases. In the case of combustion with air, this process is very expensive. In fact, exhaust gases are mainly composed of N_2 (both in mass and in volume), so that trapping CO_2 becomes more difficult.
- Oxy−combustion. If separating CO_2 from exhaust burnt gases can be very expensive in terms of process efficiency, it is more efficient to separate the nitrogen from the air before combustion. In this way, fuel is burnt with pure oxygen. Burnt gases only contain water and CO_2.
- Integrated Gasification Combined Cycle IGCC. The fuel (mainly coal) is gasified with oxygen. The gasification produces a gas mainly composed of CO and H_2 which is then burnt in a gas turbine. Final gases for this technology are also mainly composed of water and CO_2.

For these three technologies, the common final step is to separate water by condensation and to store CO_2 in a geological site rather than in the atmosphere. Three main arguments are usually against CCS technologies:

- they are expensive. Costs concern the research of a suitable geological site, pumping of CO_2, maintenance and monitoring of the site;
- the technology is not totally developed and ready to use on a full scale. Fig.1.3 depicts two different tracks towards CO_2 reduction. The first one is represented by biomass utilization and the second by CCS technologies. It can be seen that the objectives are far from being accomplished and that they will not be ready until 2030;
- the technology is not totally mastered. As a matter of fact, there are concerns about possible leakages of CO_2 into the atmosphere from the geological sites.

1.1.3 Introduction to flameless combustion and organization of the manuscript

In section 1.1.1 the environmental emergency was explained and described whereas in section 1.1.2 the recent technologies to put a possible remedy on this issue, were briefly presented. It was shown that manifold solutions are potentially exploitable either in the short and in the long term. Among the technologies illustrated, flameless combustion offers the perspective of a less polluting and more efficient technology. Furthermore, it offers desirable characteristics which are sought in some industrial applications. It is certainly promising but relatively recent (the pioneering work of Wunning appeared in 1997 [13]). For this reason, many ongoing works

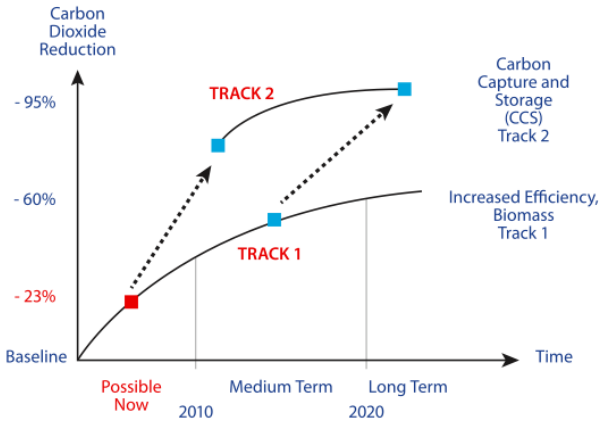

Figure 1.3 – *Different tracks (CCS and BIomass) for CO_2 abatement [12]*

focusing on this technology, have been carried out. This thesis is meant to make a contribution to the development of flameless combustion. As a matter of fact, being FC a new type of combustion, it is not completely defined and understood. The main target of this thesis is to broaden and widen the knowledge of FC by means of modelling and developing numerical simulations. In this thesis, three years of research on the subject are reported on six chapters:

- in the first chapter, the general context and the environmental issue related to the use of fossil fuels were presented;
- in the second chapter, the technology known as Flameless Combustion, will be presented in further detail. In particular, we will focus on its definition from literature and on the main industrial achievements already present in industry;
- the third chapter is dedicated to presenting the state of the art of numerical modelling of Flameless Combustion. Above all, we will explain the main differences between several combustion approaches to modelling FC;
- in the fourth chapter, the model used and developed during this thesis will be presented. In particular, the results obtained with the model on the test case of Verissimo et al.[14], will be shown;
- in the fifth chapter, a model developed during this thesis to predict NO_x in FC will be presented. The model has also been validated in the Verissimo configuration [14];
- in the sixth and final chapter, the main conclusions from this work will be presented and explained.

Flameless combustion

2

2.1 Introduction to Flameless Combustion

Flameless combustion is a new promising technology as it offers an interesting combination of lower pollutant emissions and increased efficiency. In order to understand the main features to carry out FC conditions in a furnace, it will be first compared to a classical diffusion flame. In the diffusion flame sketched in figure 2.1, fuel and mixture are mixed together. Fuel and air burn as soon as they come in contact with each other. Combustion is continuously ignited by the high temperature present in the chamber and the reactive zone is very well defined. A peak of temperature is clearly distinguished. Burnt gases are present, but in a very low fraction inside the flame structure. With regard to the second figure, a flameless combustion process is also sketched. In the most common flameless combustion process, a central jet of pre-heated air is surrounded by two or more fuel jets. Before mixing with the pre-heated air, the fuel is mixed with burnt gases. One of the main features of FC is that the mixing of these three components produces a gas above its auto-ignition temperature. Afterwards, the auto-ignited combustion occurs in an oxygen poor environment, due to the burnt gases dilution. Furthermore, this low oxygen fraction strongly limits the temperature increase. In fact, no peak of temperature is distinguished and after the first ignition part, the temperature profile remains constant.

Flameless combustion is also very peculiar from a physical point of view as no visible flame is present in the furnace. This is the reason why it has been defined as *flameless* by Wunning[13]. Image 2.2 shows how different the combustion phenomenon appears under flameless conditions. No reacting zone is observed and a uniform temperature is present in the furnace in FC conditions (b) whilst in non-flameless conditions (a) temperature gradients are clearly visible. This is one of the most remarkable features of FC, as the reaction rate is not well defined, but volumetric.

Another peculiar characteristic of FC is that it produces lower noise and that fluctuations of temperature are lower in magnitude than a normal combustion regime [13]. Experiments in this sense are reported in figure 2.3 where the temperature fluctuations are reported for the burner working in normal combustion regime (green), lifted flame (blue) and FC regime (red). It can be noticed that Flameless combustion, compared to the normal regime, presents a different level of sound, very close to the normal noise of the air alone.

This brief description, will be expounded upon in this chapter in order to give a complete overview of the technology. In order to do so, the chapter has been structured as follows:

- As for FC a unique definition does not exist, an overview of the main definitions in the existing literature for FC will be reported;
- Once FC is described, the main advantages from an industrial point of view will be presented;
- Finally, the importance of CFD in developing new combustion technologies will be explained as well as the main contributions CFD might give to develop FC.

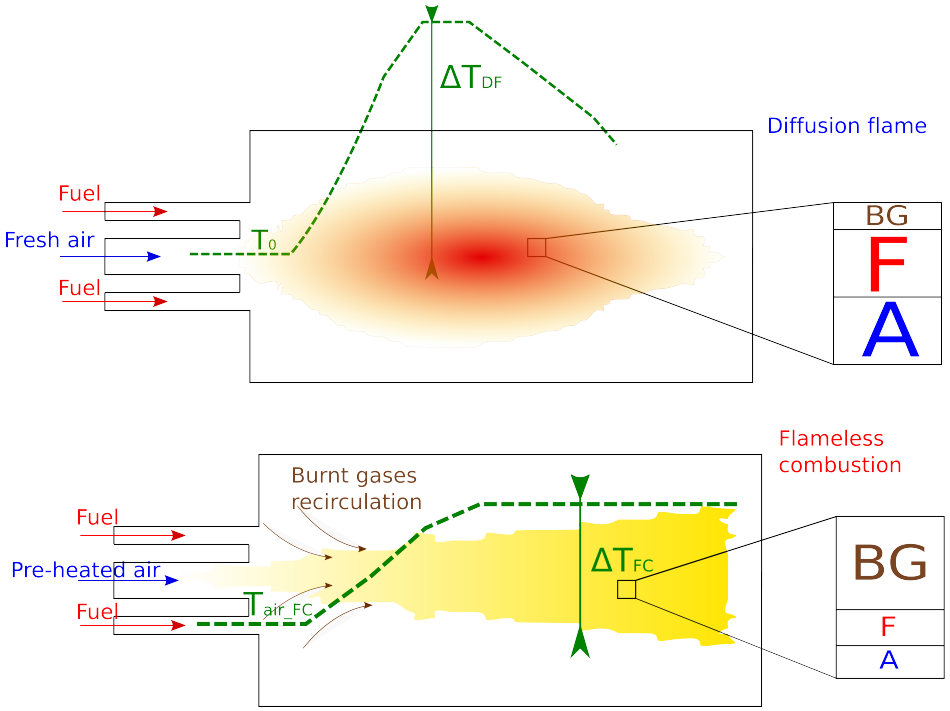

Figure 2.1 – *A diffusion flame sketch compared to a flameless configuration.*

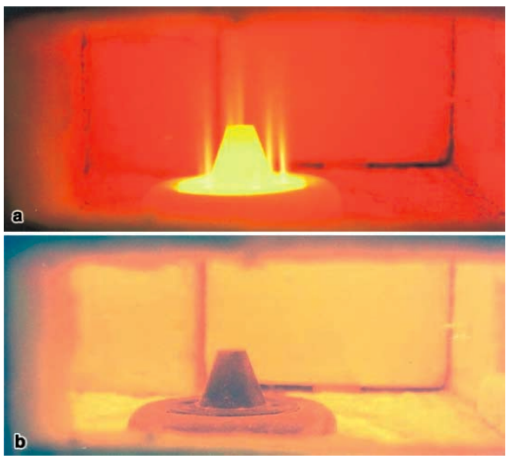

Figure 2.2 – *Visualisation of combustion (a) and flameless (b) for the furnace of Plessing et al.[15]. Image from [16]*

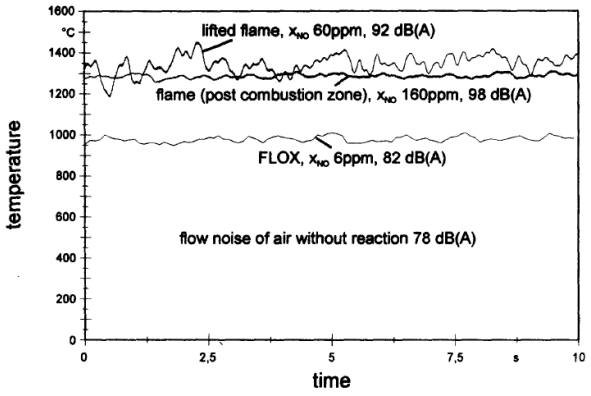

Figure 2.3 – *Temperature and NO fluctuations for the furnace investigated in Wünning et al. [13]*

2.2 Definitions of Flameless Combustion

In this section, some of the main definitions in FC studies will be reported along with a definition proposed in thesis.

- **Flameless Combustion in Borghi's diagram**: In order to better understand FC, we will now refer to Borghi's diagram ([17],[18]). In Borghi's diagram, combustion regimes are identified depending on Damkhöler's and Karlovitz's numbers, which are briefly recalled here:

  - **Damkhöler's number** is the ratio between the time needed for the dissipation of the turbulent eddies (τ_{mix}, turbulent mixing time scale), with the one for the chemical reactions (τ_c, reaction time scale). It reads:

    $$Da = \frac{\tau_{mix}}{\tau_c} \tag{2.1}$$

    A larger Damkhöler number means that the turbulent micro mixing time scale, that is the time needed for the reactants to come in contact with each other, is greater than the reactions time scale. In this case supposing that the chemical reaction advancement depending only on the turbulent times and not on the chemical kinetics (chemical reactions infinitely fast) is allowed. This condition is verified when the chemical reactions occur in a very thin front flame (flamelet). On the contrary, if the Damkhöler number tends to zero, it means that the chemical reactions occur more slowly than the mixing of the reactants and the reaction rate is determined only by chemistry.

  - On the other hand, the **Karlovitz's number** Ka is the ratio between the chemical time τ_c and the Kolmogorov time $\tau_k = \frac{\nu}{\epsilon}^{\frac{1}{2}}$ where ν is the kinematic viscosity and ϵ is the local dissipation rate of turbulent kinetic energy. Karlovitz's number equation is expressed as follows:

    $$Ka = \frac{\tau_c}{\tau_k} \tag{2.2}$$

    If $Ka > 1$, it means that chemical time is faster than the Kolmgorov time. In other words, the flame front (including the preheat zone) is thinner than the the Kolmogorov eddies (the smallest eddies in energy cascade of turbulence) and impossible to be penetrated by turbulent eddies. On the contrary, if $Ka < 1$ the Kolmogorov time is larger than chemical time and the Kolmogorov turbulent structures are able to penetrate the flame front. On Borghi's diagram, depending on

these two numbers, several combustion regimes are individuated as a function of the ratio between the fluctuation velocity $u' = \sqrt{k}$ and the laminar flame speed s_l^0 and the ratio between the turbulent length scale l_I and flame thickening l_c.

With regard to FC, the mixing of the three streams (fuel air and burnt gases) is usually promoted before combustion, contrarily to a diffusion flames where reactants start to burn as soon as they enter in contact with each other. In this case, the mixing time $\tau_{mix} < \tau_c$, so that FC can be placed on Borghi's diagram for $Da < 1$. For the same reason, a parallelism of FC with HCCI (Homogeneous charge compression ignition) was proposed in Cavaliere et al.[19]. In fact, in the HCCI engines, combustion is also promoted after an optimal mixing between air and fuel.

- **Definition from Wünning et al. [13]**: Wünning et al. analyze the effect of burnt gases recirculation in a flame. First of all a recirculation rate is defined as follows:

$$K_v = \frac{\dot{M}_E}{\dot{M}_F + \dot{M}_A}$$

where $\dot{M}_E$, $\dot{M}_F$ and $\dot{M}_A$ are the mass flows of exhausted gases recirculated, fuel and air respectively. In Fig.2.4(b), three flames are shown: the first flame (A) is a classic stable flame with little or no gas recirculation ($K_v \leq 0.3$); the second flame (B) is a flame diluted with hot burnt gases but unstable due to high recirculation; the third one (C) is a stable flame even with high recirculation rates and belongs to the category of flameless oxidation. In order to understand when a flame can be stable even when strongly diluted, it is useful to report on a diagram $T_f - K_v$ (where T_f is the furnace temperature) the existence fields of the three flames (Fig.2.4(a)). In this figure, the flame (A) exists for low K_v regardless the furnace temperature. If the flame is diluted and the temperature of the furnace is not high enough, the flame blows off due to the high amount of the inserts present in the burnt gases (*No reaction* region). Flame (B) is a transient region which occurs when K_v is increased but the furnace temperature is not high enough to sustain the process. Finally region (C) correspond to the flameless combustion. K_v is higher than 3 (strong recirculation), but due to the high temperature of the furnace, the fresh gases burn in a stable form. Therefore, in their work, it is declared that for FC to occur, i.e. to obtain a stable form of combustion for high K_v ($K_v \geq 3$), the furnace has to be heated up to sustain the combustion of the reactants.

- **Definition from Oberlack et al.[20]**: In this work the physical and mathematical proof of the existence of the FC is given. First of all, a homogeneous flow reactor is mathematically defined as a function of several parameters, among which one finds the activation energy E from Arrenhius' law and the Damköhler number Da. The mathematical system proposed, allows the description of the PDF of T, which depends on the stochastic variation of Da. The higher the value of the PDF as function of T, the higher the possibility of finding a physical state for a given T. An interesting aspect of classic combustion is the strong duality of the unburned−burned states. States in between are unstable, so that such a system can be represented by a S-Shape curve. Furthermore, common combustion appears only when the condition (13) of [20] exists, which is the condition that allows two singularity points. With regard to FC, this condition is not realized so that, differently to the classical condition, a univocal curve (not S-Shaped) is shown, as if more states were possible. In other words, this mathematical definition, allows the retrieval of an interesting definition: if on the one hand in classical combustion one finds two physical states well defined and very different from each other, on the other hand the line between the two states in FC condition is less defined, without a net distinction between burnt and unburnt states.

- **Definition from Cavaliere et al.[19]**: In the work of Cavaliere et al. a more rigorous definition of FC combustion is given, even though it is based on a well stirred reactor. This work relies partially on the work of Oberlack et al. seen above. In Fig.2.5(b), the temperature of a well stirred reactor T_{WSR} is shown as a function of the initial temperature

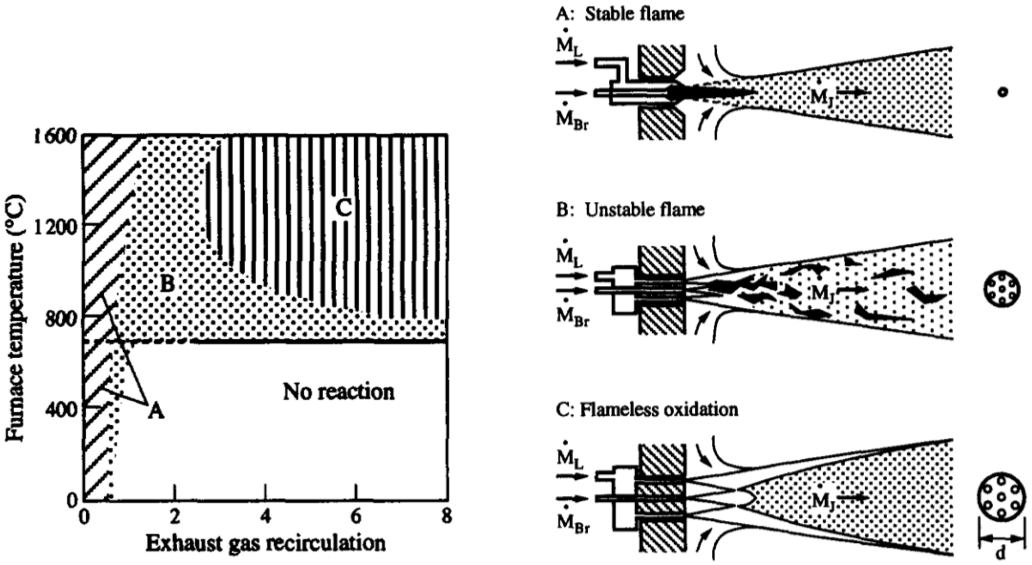

(a) (b)

Figure 2.4 – *From Wunning et al.[13]: The combustion diagram (T_f-K_v) and different kind of flames*

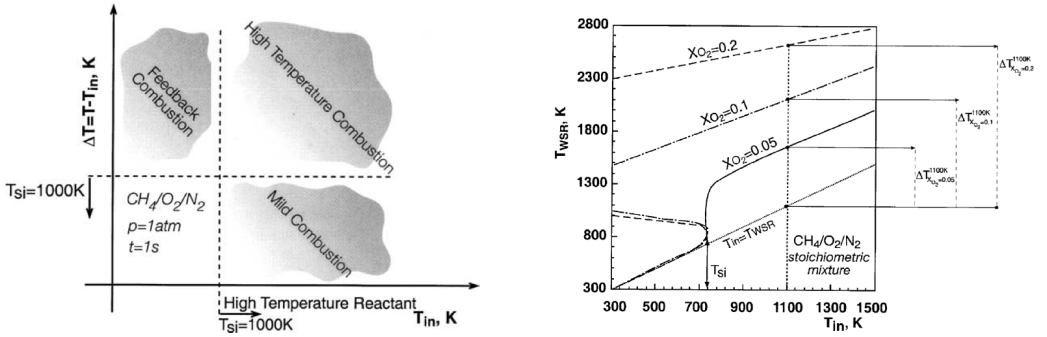

(a) (b)

Figure 2.5 – *From Cavaliere et al.[19]: Working points and diagram of FC*

of the reactants. The iso−oxygen−concentration curves are plotted. For high concentrations of oxygen, $x = 0.2$ or $x = 0.1$ for instance, a S-Shape curve can be identified. This curve represents a transitional state between low temperatures (unburnt state) and high temperatures (burnt state). The states of the S-Shape curve are unstable, and have a very small probability. If the oxygen concentration is further reduced, the S-Shaped curve is not observed; in this case the system has switched towards a FC as combustion occurs in a poor oxygen environment and limited temperature increase. As a matter of fact, for this curve, if compared to the T_{in} of the reactor, the temperature increase is small if compared to the combustion mode. From these observations, FC is defined as follows by Cavaliere *"A combustion process is named Mild when the inlet temperature of the reactant mixture is higher than mixture self−ignition temperature whereas the maximum allowable temperature increase with respect to inlet temperature during combustion is lower than mixture self-ignition temperature (in Kelvin)"*. This definition is graphically reported in Fig.2.5(a) and compared to the working fields of high temperature combustion and feedback combustion.

2.3 Flameless combustion in industry

Flameless combustion is a technology which has attracted researchers and industrial companies since its discovery. The possibility of a more rational and cleaner use of fossil fuel is very attractive from a technological point of view. Furthermore, the possibility of obtaining a more diffused temperature field, makes FC very promising for industrial applications in the steel, glass and ceramic industry. This section is divided in two parts. In the first part, all the advantages of this technology will be detailed from different points of view. In the second part, some existing FC implementations already used in industry will be presented.

2.3.1 Advantages of Flameless combustion in industry

The advantages of FC concern improved performances in terms of efficiency, pollutant emissions and economic savings. Also it is suitable for particular industrial applications such as steel, ceramic and glass furnaces. These aspects will be now presented in detail.

Reduction of pollutant emissions

As stated above, such a combustion mode allows the reduction of pollutant emissions and the improving of burner efficiency. In this section we will analyze how the physics of the FC regime can result in these two positive outcomes. As far as the pollutant production is concerned, their formation is favored if burnt gases containing oxygen are exposed to[13]:

- temperatures > $1600K$ and residence times on the order of seconds;
- temperatures > $2000K$ and residence times on the order of milliseconds;

In this sense, the two elements to avoid to reduce NO_x production is to limit hot and oxygen−rich pockets. Both these factors are mitigated at the same time in FC. A clear example of the potential of the technology in this sense, is reported in Malfa et al., Combustion Colloquia 2009 [21]).

In this work, three main technologies for NO_x reduction, namely air staging, internal flue gas recirculation and flameless combustion, are compared to a traditional burner. All the burners considered are burners of large size ($> 1000kW$). The four burners used to collect the data and to carry out the experimental campaign are the following: the traditional burner was a Hennig burner, the air staging one was a Hauck TRIOX, the one operating with flue gases recirculation was a Techint TNS and the one operating in flameless mode was a Techint TSX (further detail about the experimental campaign and all the four burners used can be found in the final report of the *Research Programme of the Research Fund for Coal and Steel 2003 - 2007* [21]) In this work, flameless combustion appears as the best technology available as far as NO_x reduction is concerned. As a matter of fact, if compared to air staging and internal flue gas recirculation technologies, the lowest quantity of NO_x is emitted. With respect to a traditional burner, the technology can drop to 80% the NO_x production of a burner.
Another work dealing with NO_x emissions in FC regime is that of Plessing et al. [15]. As seen in Fig.2.4(a) and 2.4(b), in order to obtain a stable form for FC, the furnace has to be heated. In Fig. 4 of [15], this pre-heating process of the furnace is shown. Temperature at the exit of the furnace increases as a function of time. Also NO_x are shown as a function of time. When temperature reaches $800^{\circ}C$, the furnace switches in FC mode, and NO_x drop dramatically from 35 ppm to 10 ppm.

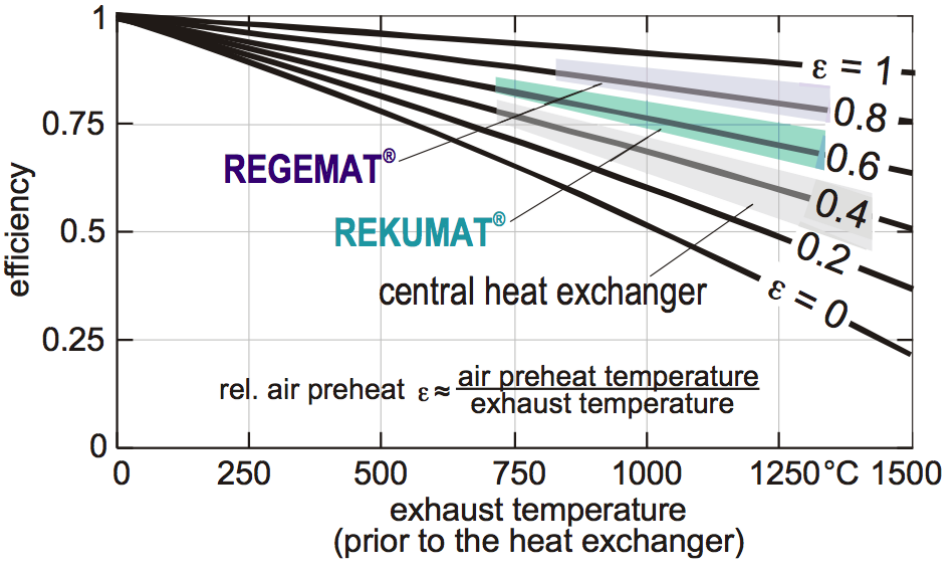

Figure 2.6 – *Effect of air-preheating for 3 different technologies compared to no-air-prehating operating mode ($\epsilon = 0$) in function of exhaust temperature [22]*

Efficiency increase in Flameless Combustion

As far as the efficiency is concerned, the most common method to improve it, consists in pre-heating the air either by using a heat exchanger to recover burnt gases enthalpy. If this method allows obtaining an improvement of the efficiency of the burner, on the other hand, the final temperature of the mixture is increased, resulting in greater emissions of NO_x. In FC, although the fresh gases temperature is increased, the low content of oxygen strongly limits NO_x production. Wunning [22] presents clearly the potential of air-preheating in FC. He shows the results of a comparative study on different burners, combining air-preheating to different technologies such as regenerative burners (explained in detail in section 2.3.2), recuperative burners (burnt gases counter-flow with air in a heat exchanger, in order to recover their enthalpy) and burners with heat exchanger. Figure 2.6 shows the efficiency of several burners as a function of exhaust gases temperature. In particular, the REGEMAT (regenerative burner) which works in FC mode and the REKUMAT (recuperative burner) which works in combustion mode are presented. Each burner works with a different air-preheating rate ϵ, defined as the temperature ratio of pre-heated air and exhaust gases. If air is not pre-heated ($\epsilon = 0$), efficiency drops dramatically as exhaust gas temperature increases. As the air-preheating rate is increased instead, not only the efficiency increases, but it is also less dependent on temperature exhaust gases. Furthermore, the REGEMAT which works in FC, presents the highest efficiency among the other burners.

Flameless combustion in steel industry and other applications

The possible applications of FC in industry are many. Generally speaking, FC finds its best application when a uniform field of temperature is required.For instance, its performances in terms of efficiency can be exploited for gas turbines [23] or coal fueled furnaces [24]. As anticipated in the introductory part of this chapter, FC presents a diffuse field of temperature which is sought for particular industrial applications. For example, in the steel industry it allows the improving surface treatment processes. Let us consider a galvanization line for steel strip production ([25]). In this case, an uniform temperature field is one of the most critical elements. This is because discrepancies in the surface of steel are to be avoided in order to improve the

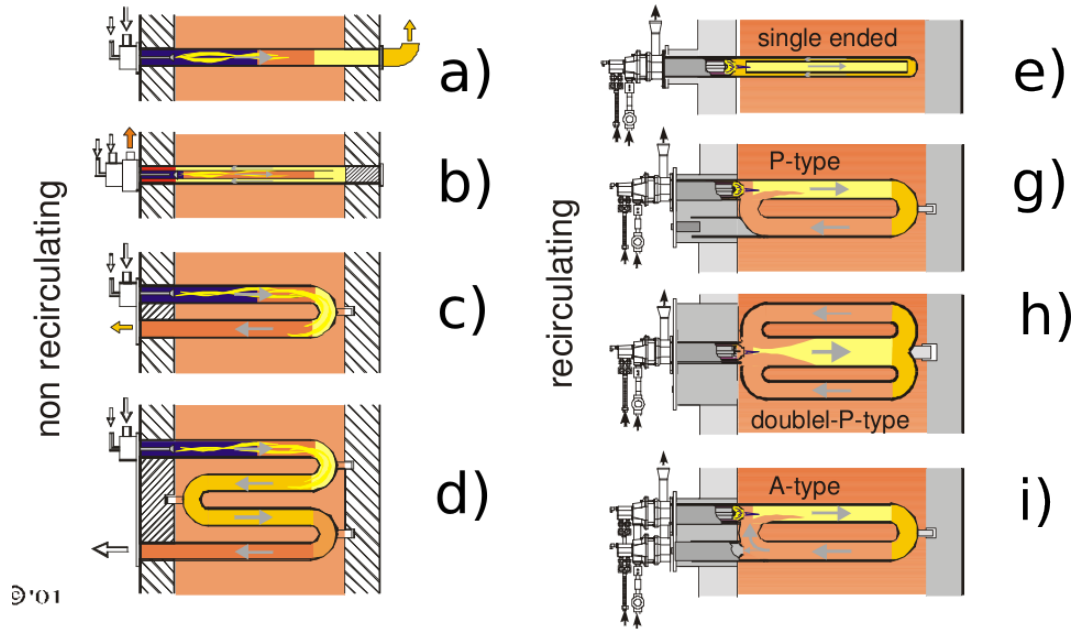

Figure 2.7 – *Solutions of radiative tubes for steel furnaces and gradients of temperature. Figure from [26]*

quality of the final product. Generally, W-shape tubes and the U-shape tubes (*c* and *d* in figure 2.7) are the most common solutions in steel industry for the strip lines producing (A.Milani [26] and Wünning [27]). This kind of furnaces are not *recirculating solutions*. It means that fuel and reactants are injected from one side and extracted at the outlet. In these tubes, near to the injection zones, the flame is still controlled by fluid-dynamics as injection velocity is still high. After this first zone, inside the radiative tube, only exhaust gases are present. Consequently, the radiative tube does not have a uniform temperature. It is clear that the temperature field for these solutions is quite discontinuous. First of all, a higher temperature is present at the injection section. Furthermore, the elbows are zones where burnt gases concentrate and high temperature gases pockets form. In the elbows higher temperature and gradients are also present and these zones favor NO_x. With respect to the W-shape tubes (d), the situation can be slightly improved with the U shaped radiative tubes (c), but strong temperature gradients are still shown. A more uniform temperature is instead obtained with recuperative furnaces (*e*, *g*, *h* and *i* solutions in figure 2.7), with the radiant tubes working in FC mode. In order to attain FC conditions, a counter-current burnt gases flow is generated. The flame entrains the burnt gases and gradients of temperature almost disappear. This results in a more diffuse field of temperature.
Now, this brief description was intended to explore the possibilities of using flameless technology in this field. As already shown above, FC can accomplish the task of producing an uniform temperature field. For this reason it can also be used in the case of ceramic and glass production ([13],[28]).

2.3.2 Industrial applications of flameless combustion today

This section is meant to give some example of FC in the industrial field, by presenting some documented and referred results. All the furnaces presented are actually used in industry nowadays; the data here reported are retrieved on the internet site of the main manufacturers whose research involves FC. For all the furnaces presented, it will be reported:

- the maximum produced power

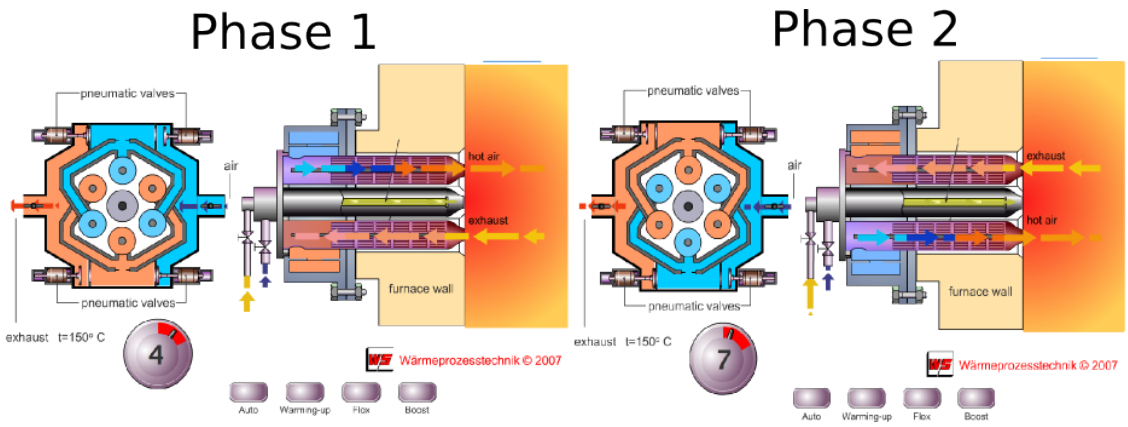

Figure 2.8 – *From an animation on the website [29]. The two alternatives phases of a REGEMAT 250. Please notice that in phase 1, hot air flows in the upper burner from left to right and that in phase the two flows are inverted.*

- the NO_x emissions.

The first burner described is designed and built by the german *FLOX* company (http://www.flox.com). It is the REGEMAT (250 and 350 depending on power). The REGEMAT is represented in Fig.2.8 and is based on a regenerative technique: Fig.2.8 illustrates the axial and longitudinal cut of the combustion chamber during two different operating phases. In the first phase the upper burner is on: its air flows through a heat exchanger previously heated by the exhaust gases of the second burner. In this way the enthalpy of the exhaust gases of the second burner is recovered. The fuel burns in a FC atmosphere. The pneumatic valves allow switching to the second phases, where the second burner is activated and recovers the enthalpy of the exhaust gases of the upper burner. The results of the efficiency for this burner were already anticipated in chapter 2, in Fig.2.6. The REGEMAT can work either in FC or combustion mode; to switch to FC air pre-heating temperature has to be above 850C approximately. NO_x emissions are below $100ppm$.

Another example of furnaces employed in the steel industry are the TENOVA furnaces, TSN and TSX, described in [30]. In this report, it is shown how environmental limitations on NO_x emissions were successfully respected by means of FC technology. The american Rocky Mountain Steel (RMS) for instance, installed 26 TSX burners in the heating zone of steel. The temperatures required for this process range from 1100 to 1300$^{\circ}C$. The limit in the state of Colorado, where the burners were actually installed, was $\simeq 58ppm$. The limitations were respected all along the day, regardless the process temperature.

Another interesting application for flameless combustion is the coupling of FC with oxy-combustion, cited in section.1.1.2, in order to ease carbon capture and storage operations. Examples in this sense are already documented and realized; one example is found in the documents [31] or [32], where the annealing and pickling line of Avesta Works is presented. It is one of the world largest oxy-flameless installation, with a power of $39MW$ and $24m$ of length and $75t/h$ of fuel supply. Another experimental burner was realized in Cottbus. The results on the burner were presented in [33]. The burner used dry-lignite as fuel and presented a thermal power of 0.5 MW. The study focuses on parametrical variations such as combustion time and gas composition.

2.4 Issues in Flameless Combustion furnaces design and interest of CFD

Developing a furnace or a burner needs many tests and it is generally an expensive process. *R&D* operations can become even more expensive when dealing with particular and relative new physical phenomena such as FC. Above, we have seen that the conditions to attain FC depend on many factors such as temperature process, pressure, recirculation ratio etc.. . The optimization of these factors needs many tryings and investigations, with a high cost. Furthermore, in order to retrieve emissions or exhaust burnt gases temperature, experiments have to be carried out with experimental set-ups, which can be relatively costly depending on the size and power of the burner. In addition, retrieving fields of velocity or temperature requires precise techniques and facilities (optical measurements and probes) that can be extremely money consuming. A potential way to reduce this kind of cost is represented by numerical simulations. In numerical simulations mathematical equations issued from a physical model are resolved on computers. Numerical simulations include:

- 1D simulations: in this type of numerical simulations, the geometry of a furnace is reduced to a global 1D system which requires global inputs such as temperature of the reactants, mass fractions etc. . Data such as the final temperature of the process can be obtained. This kind of modelling is inexpensive in terms of CPU time, with running times that can be even lower than the real time process.
- 2D or 3D simulations: in this case, the furnace geometry is simulated. The fluid dynamics equations are resolved in meshes or grids which represent the geometrical domain. This simulations are more reliable in terms of final inputs and allow to retrieve more complete information such as velocity, temperature and species fields. They present higher costs compared to 1D simulations in term of CPU time. Running time can be on the order of 1-7 days.

Now, numerical simulations can represent a significative reduction of *R&D* costs, as they can furnish a complete representation of what occurs inside the furnace. Though, the other side of the coin is that numerical simulations do not offer the same reliability or accuracy of experiments. As a matter of fact, probes or optical techniques measure the physical variables with an accuracy on the order of $1 - 10\%$. CFD can also offer this kind of precision by employing very precise models which have enormous CPU costs and excessive running time (see chapter 3). In this sense, the CFD community has to make strong efforts to reduce computational costs of physical models and to improve their accuracy. In the next chapter, we will expound upon the relationship between CFD and FC, above all to illustrate the recent discoveries of the research community by means of numerical techniques.

3 State of the art in numerical modelling of Flameless Combustion

The aim of this chapter is to outline the state of the art of Flameless Combustion. The chapter is divided in three parts. In the first part, burners relevant to validate FC models are presented. Semi-industrial and laboratory-scale furnaces are distinguished. In the second part, important results obtained in numerical modelling of FC are presented. Finally, the aim of this thesis is be presented.

3.1 Flameless combustion burners for model predictions

In this section, FC burners used to validate numerical set-ups in CFD are presented. These configurations are not used in an industrial context but are rather employed in laboratories. The aim of these furnaces is to retrieve important data such as velocity, temperature and species fields to compare with the numerical simulations. Such data cannot be retrieved from industrial furnaces, which are not designed to insert probes to investigated the field properties. Burners are divided into two categories. Semi-industrial furnaces are not used in industry, but present large powers and large sizes ($< 2m$), comparable to industrial facilities. In the second category the laboratory furnaces are included. These furnaces have small sizes and small powers ($< 1m$,$< 20kW$). Furthermore, their design is simple with cylindrical burners. This is a great advantage when flow and physical properties are to be investigated in detail.

3.1.1 Semi-industrial test-cases

This section discusses the semi-industrial test cases. Among these furnaces, the HEC (High efficiency combustion) configuration of IFRF is investigated by Burggraaf et al.[34] and Battaglia et al.[35]. The power of the furnace is 1MW. The HEC furnace adopts the regenerative technology developed for the REGEMAT series of WS, which was already explained in section 2.3.2. Burggraaf carried out an experimental campaign by fueling this furnace either with natural gas or with a coke oven. The efficiency of the furnace is around 85%. The authors claim that for regular combustion the efficiency would be rather 50%. Numerical investigations for this furnace are reported in [34] and in [35].

Another technology, also belonging to IFRF is HiTAC (High Temperature Air Combustion) ([36], [37] and [38]). In this furnace, air and fuel burn under lean conditions in a pre-combustor. Downstream, the vitiated air from the pre-combustor is injected in the main furnace and mixed with additional fuel. The vitiated air reaches very high temperatures. Under the conditions simulated by Mancini [38], air was pre-heated up to $1300°C$ and natural gas was used to fuel the furnace. The thermal load was $0.58MW$ and NO_x emissions on the order of $120ppm$.

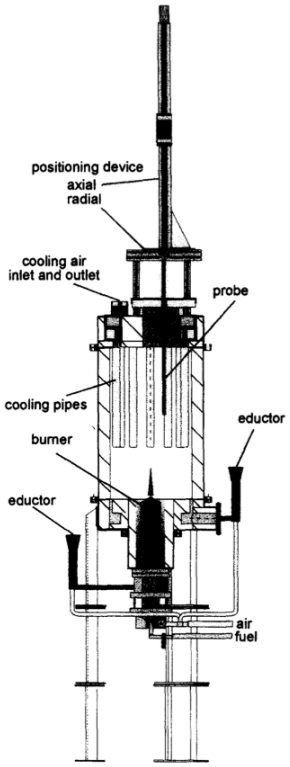

Figure 3.1 – *Experimental setup of the Mild Combustion furnace experimental studies in [13]*

Krishnamurthy et al. [39] investigated the thermo-fluid dynamics of an oxy-flameless burner, in which air was replaced by pure oxygen. The burner was 4.5 m long with a power of $200kW$ and the fuel was propane. The burner is able to work in combustion and flameless mode. In their work, the authors discussed the soot reduction effect of FC.

3.1.2 Laboratory test cases

In this section, several laboratory test cases are presented. As discussed above, these experiments are suitable to perform CFD model validation campaigns are carried out. The burner small size has experimental and numerical advantages. Experimental data can be easily retrieved and the necessary CPU time for numerical simulations is low. The boundary conditions of such burners are well described and the physics of these flames is better understood. Wunning et al. [13] studied a $1m$ long furnace with one central nozzle of gas and 6 nozzles of pre-heated air. The experimental set-up presented in Fig.3.1 was equipped with cooling pipes. The furnace is operated in flameless and combustion mode. Under flameless condition, only 6 ppm of NO_x were emitted (160 ppm in normal combustion regime). The final temperature of the burner was at $1000°C$. One of the main features of FC, i.e. the low noise emission, was also investigated for this burner by measuring temperature fluctuations under flameless conditions (see Fig.2.3).

Plessing et al. [15] conducted an imaging campaign for a flameless burner. The chamber had a length of $485mm$ and can be switched to FC mode, after pre-heating the fresh gases to only $800°C$ (1073 K). The temperature inside the furnace was $1200K$. In the burner a central jet of methane is surrounded by a coflow of pre-heated air. Air is pre-heated by a counter flow of burnt gases. In particular, the conditions necessary to stabilize flameless combustion are inves-

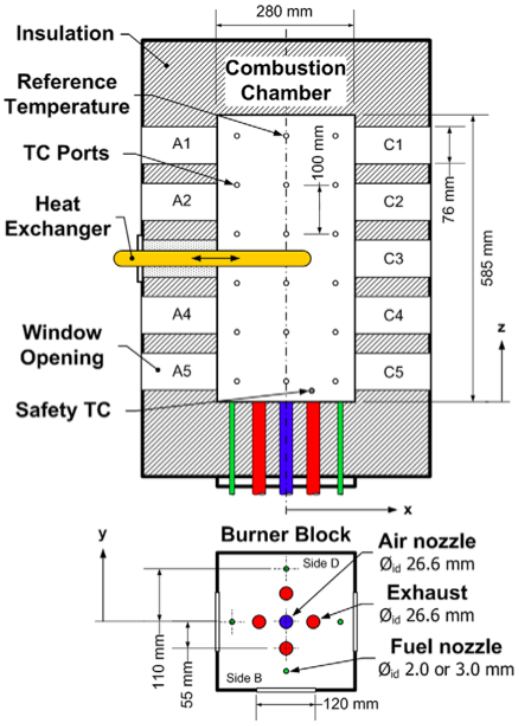

Figure 3.2 – *Scheme and injection detail of the furnace studied in Szego et al. ([41] and [42])*

tigated. In this work the necessity of pre-heating the furnace before stabilizing FC conditions is confirmed. This phenomenon was first observed in [13]. Remarkably, NO_x production drops dramatically from 35 ppm to 10 ppm as the furnace switches to FC regime (these results are already presented in section 2.3.1).

Oždemir et al. [16], investigated the flow field for the same furnace and performed an imaging campaign for OH. They also visualized the vicinity of the burner for both combustion and flameless mode. Velocity fields were also measured in this work. Furthermore, solid particles were dispersed inside the furnace, in order to measure residence times. Dally et al.[40] investigated the effects of diluting fuel with CO_2 and N_2 and its influence on NO_x production and temperature. In their work, they also deepened the understanding about the existence of unstable region B of Fig.2.4(a). They suppose that this region can appear when if in the vicinity of the burner, regions with large residence times and low scalar dissipation rates exist. An intermittent combustion can occur, with local flames propagating continuously downstream, destabilizing the combusion process. Effects of dilution with CO_2 and N_2 were also investigated on NO_x emissions. The experiments were also supported by a numerical investigation.

Szegoe et al. ([41],[42]) investigated a burner with a heat exchanger. The burner, shown in Fig.3.2, has a maximum capacity of 20kW. The burner consists of a central nozzle of air and 4 nozzles of fuel (methane). Exhaust gases exit the burner in the planar section of the injectors. The air is pre-heated to 450°C. In FC mode, the gas temperature in the furnace increases up to 1300°C. In this work, the effects of the heat exchanger interacting with the flame and the effect of recuperating heat from the furnace are investigated experimentally and numerically. Galletti et al. [28], performed a numerical and experimental study of a burner belonging to ENEL (Ente nazionale per l'Energia Elettrica, the Italian electric society). The burner is used in the steel industry (it can be also used for the glass and ceramic industry) and has a nominal power of 13 kW. The burner adopts a recuperative technique, heating the flow by exhaust gases through a radiant tube inside the furnace. The NO_x emissions of the burner are on the order of 30 ppm. Authors argued that the same furnace operating in normal mode would

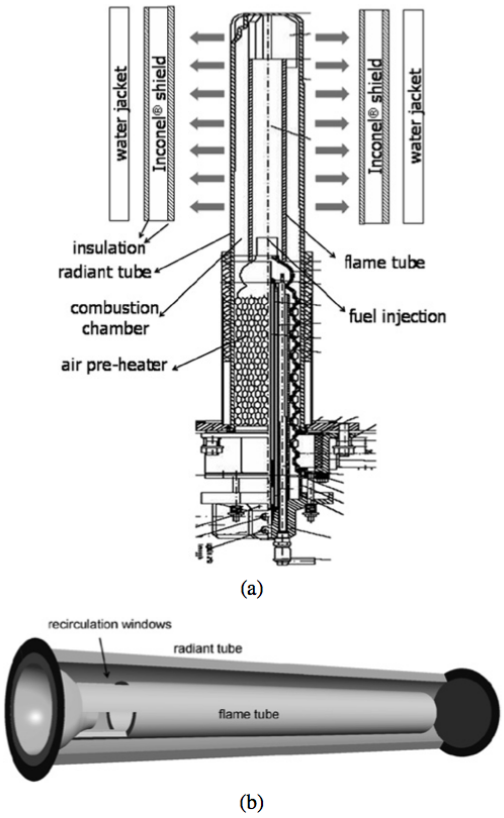

Figure 3.3 – *Scheme of the furnace and representation of the internal furnace of the furnace studied by Galletti et al.[28]*

produce emission up to 1000 ppm.

Jianchun ([44],[45]) examined the same test case as in [42]. For this study, fuel and air were premixed, resulting in a premixed flameless oxidation, which is not the common practice in the field. Ayoub et al. [46] realized FC conditions for a mixture of H_2 and CH_4. Maruta et al. [47] investigated the effects of the scalar dissipation rates on the reaction zone on FC regime. Verissimo et al. [14] studied the operation characteristics of a small-size combustor (10 kW). In the Flameless regime, air was injected at $113 m/s$ and $T = 400°C$ through a central pipe, which was surrounded by 16 small injectors for methane. Dally et al. [43] investigated the jet-hot-coflow burner JHC. This burner consists of a central fuel jet, surrounded by a second burner. This second burner provides a mixture of hot burnt gases, which are then mixed with a mixture of nitrogen and air in order to regulate the oxygen concentration. Several radial measurement are available for the burner which was numerically investigated by Ihme et al. in [48] and [49].

Table 3.2 summarizes all the burners presented in this section.

Burner	Society/ University	Power	Utilisation	Fuel	Temperature process	NO_x emissions	T air pre-heated	Max size	Papers
Industrial burners									
REGEMAT	WS	120 - 400kW	Steel, chemistry	Natural gas and methane	$1050 - 1250C$	100 ppm	–	530 mm	[29]
TSN	TECOVA	1 - 4MW_{th}	Steel	Natural gas	$1150 - 1250 \circ C$	65 ppm	$450 \circ C$	–	[30]
TSX	TECOVA	1 - 4MW_{th}	Steel	Natural gas	$1150 - 1250 \circ C$	40 ppm	$550 \circ C$	–	[30]
Outokumpu	Linde	39 MW	Steel	Oil	–	$65 mg/MJ$	–	24 m	[31], [32]
Semi-Industrial burners									
HEC	IFRF	0.3 - 1MW_{th}	–	Natural gas and coke oven	$750 - 1350 \circ C$	up to 80 ppm	–	–	[35], [34]
HiTAC	IFRF	0.58MW	–	Natural gas		120 ppm	$1300 \circ C$	6.25m	[36], [37], [38]
OxyFlam	Sweden	0.2MW	–	Propane	$1500 \circ C$	0.005 Kg/m^3		7.9m	[39]
Laboratory test cases									
FLOX	RTHW	–	Steel	Natural gas	$1150 - 1250 \circ C$	65 ppm	$450 \circ C$	1 m	[13]
–	ENEL	13kW	Ceramic/ Glass/ Steel	Methane	$--$	30 ppm	$--$	0.58 m	[28]
MCF	Australia	20kW		Natural gas	$\simeq 1250 \circ C$	50 ppm		585 mm	[41] ,[42]
Plessing	RTHW	10kW		Natural gas	$\simeq 1250 \circ C$	50 ppm		585 mm	[15]
JHC	Australia			CH_4/H_2			1300 K		[43]
REKUMAT	WS	–		Methane	-	10 ppm (1000 K)		485 mm	[15], [16]
Verissimo	Lisbon Univ.	10KW		Methane	1350K	20 ppm	673K	500 mm	[14]

Table 3.1 – *A schematic representation of the burners in literature, depending on the categories chosen by the authors*

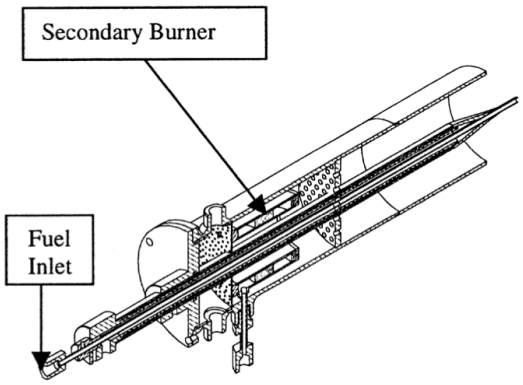

Figure 3.4 – *Scheme of the JHC burner of Dally et al.[43]*

3.2 State of Art in numerical simulation of Flameless Combustion

3.2.1 Main approaches to simulate FC in CFD

As explained above, generally in Flameless Combustion three mixing streams are present. They are the fuel, the oxidizer air and the diluent burnt gases. This mixing usually occurs in a turbulent environment due to the strong velocity injections and recirculation regions inside the furnace. From a numerical point of view, turbulent phenomena (in this case a turbulent ternary mixing) are quite hard to capture and predict, as turbulence is a phenomenon which takes place at different length scales (from macroscopic to microscopic). Fig.3.5 shows the turbulent energy cascade where the turbulent kinetic energy is presented as a function of the wavenumber k, defined as $\frac{2\pi}{\lambda}$, where λ is the wavelength. In this graph, three main zones are represented: a first zone (production zone), with the largest and more energetic eddies; a second zone (inertial range) where the eddies loose their energy and reduce their size); a third zone (dissipation scale) where the eddies have a microscopic size and totally dissipate due to the viscous frictions. In order to simulate this multi-scale phenomenon, three main approaches exist (see Fig.3.5):

- Direct Numerical Simulations (DNS): in DNS, the Navier-Stokes Equations of the flow are directly resolved on a computational grid. The turbulent spectrum is resolved to the smallest dissipative eddies. Consequently, the cell size dimension to resolve the turbulent flow is very small (depending on the Reynolds number of the flow) and computational costs are very high. At present, employing DNS to simulate furnaces (either at the industrial or laboratory scale) is not feasible. Nevertheless, they are used to validate or propose sub-grid scale models or to retrieve information on the microscopic phenomena of turbulence;
- Reynolds Average Navier-Stokes (RANS): in RANS turbulence is not resolved but modelled. The Navier-Stokes equations are averaged on the entire turbulent spectrum and only the average signal of the flow is retained. The advantage of this type of simulation is certainly its contained computational costs. For this reason, since the beginning of CFD, it has been widely used and still is the main approach. However, the predictivity on turbulent flows is only qualitative.
- Large Eddy Simulations (LES): in LES, a filter is applied to Navier-Stokes Equations. In this way, the larger eddies are directly simulated whereas the smaller ones are modelled. In order to model the smallest eddies, it is necessary to employ sub-grid scales models.

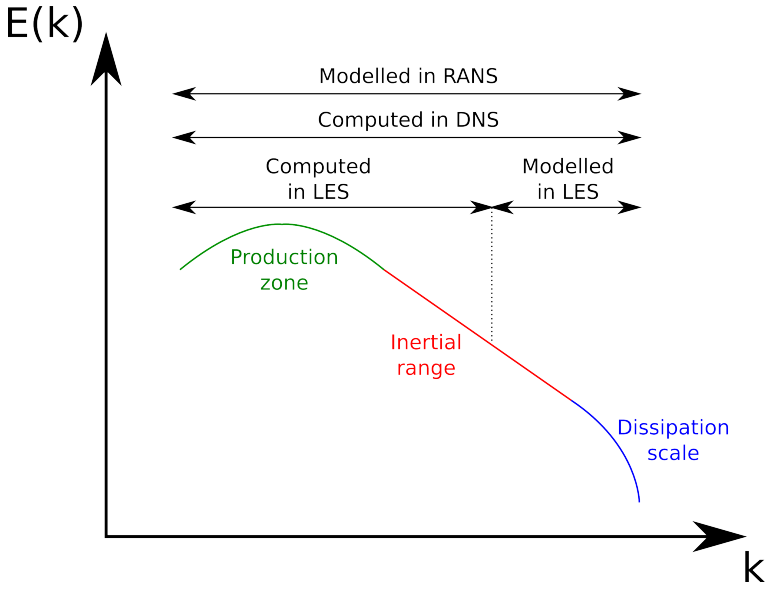

Figure 3.5

At present, their use is widening in CFD computations and it is now possible to employ them for small-size furnaces ($< 1m$).

Now, in order to predict reactive turbulent flows, the turbulence tools need to be coupled with a combustion model. In the case of FC, the main characteristics of combustion, deduced from the previous definitions, are now summarized:

- combustion from $Da < 1$ to $Da > 1$: in flameless combustion furnaces, one can find both regions with slow chemistry ($Da < 1$) and regions with fast chemistry, where reactivity is piloted by the turbulent mixing ($Da > 1$). As both these situations can be found in the same furnace, the model should be able to deal with both of them. More precisely, models based on infinitely fast-chemistry are only suitable for regions where $Da > 1$ but are not accurate for regions where reactivity is piloted by turbulence.
- turbulent combustion: as seen in the previous chapters, FC occurs in a turbulent environment. Combustion models are sometimes retrieved from 1D systems or homogeneous tables which can not describe the influence of turbulence in combustion. Generally, it is necessary to adapt homogeneous combustion models to turbulent combustion models by employing stochastic models, such as probability density functions PDF;
- high velocity jets: in FC furnaces internal recirculation is favored by high-momentum jets. These jets can be characterized by strongly strained flows which locally quench. Consequently FC models should account for the notion of strain in their formulation. Generally, in order to account for strain, the flamelet formulation introduced by Peters [50] is adopted to develop these kinds of models. Generally speaking, a flamelet is a 1D approximation of a counter-flow diffusion flame, which is identified by its strain-rate value.
- ternary mixing: this aspect was also discussed in the previous chapters. Fuel, air and diluent burnt gases, mix together in a turbulent environment. We will see in section 3.2.3, that combustion models which account for only binary systems (only fuel and air), lack accuracy in predicting FC. For this reason, it can be necessary to build models able to consider the diluent burnt gases stream in their formulation;
- auto-ignition: following the definition of Cavaliere et al.[19], the ternary mixing in FC happens at a temperature larger than the temperature of AI of the mixture. Conse-

quently, the model should be able to predict AI correctly. Very simple models sometimes are built on steady systems at equilibrium, which do not consider the unsteady phenomenon of auto-ignition. These models should not be able to describe correctly FC, generally speaking. In order to describe correctly auto-ignition it is necessary to employ complex chemistry mechanism, because auto-ignition is a complex phenomenon where many species (> 30 species) are involved;

- under-adiabatic combustion: FC furnaces in general are designed to exchange large amounts of heat with their surroundings. Consequently the burnt gases of the furnace are strongly under-adiabatic. This under-adiabaticity plays an important role both in the heat exchange and in pollutant emissions. Ideally, a comprehensive model for FC should also account for enthalpy losses.

In this brief presentation it was shown that FC is a multi-scale and multi-physical phenomenon. At present, several combustion models have been already coupled with both RANS and LES. The aim of the next section is to present a state of the art on FC modelling. The state of art is divided in two parts: in the first one, the works carried out in the RANS context are presented. The characteristics of the RANS models and how they perform in FC case will be described. Secondly a state of art in LES will be also presented. This state of art will not be as complete or exhaustive as the one in RANS, as at present few works have been carried out in LES for FC.

3.2.2 State of art in RANS modelling of Flameless Combustion

RANS turbulence modelling is a qualitative modelling of turbulence, where only the average turbulent signal of the flow is obtained. If on the one hand the computational cost of RANS modelling is certainly small compared to LES or DNS, on the other hand in the mixing regions of the flow, imprecisions and lack of accuracy are often shown for this type of simulations. This section will present some of the most common RANS combustion models.

Non-flamelet models

Mixing controlled combustion models These models are based on the hypothesis of infinitely fast chemical reactions and are therefore valid for large Damkhöler numbers. Reaction rates are proportional to the ratio $\frac{\varepsilon}{k}$, where k is the turbulent kinetic energy and ε is the turbulent dissipation. The first model belonging to this category was Spalding's eddy break up model [51]. Magnussen and Hjertager's Eddy dissipation model [52] is based on the EBU model and it differs from the constants used on the two models [53]. The EDM model does not take into account the kinetics of the reactions. Therefore it can be only used with global reaction mechanisms and only the concentration of the final species is computed. In the case of more than two reactions, it is not suitable. EBU and EDM models are very easy to implement and present small computational times. Of course, this kind of model does not account for complex chemistry. Consequently, auto-ignition phenomena can not be taken into account. Furthermore, they are not suitable for $Da < 1$, region to which FC belongs.
Eddy Dissipation model-finite rate (EDM-FR) In EDM-FR, two reaction rates are calculated. The first one is based on the mixing rate while the second is calculated using an Arrhenius' expression. Then the model uses the minimum value of the two. The EDM-FR slightly improves the EDM, as the Da range considered is wider. Though it is advised when reaction rates are limited either by the mixing or by the kinetics whereas it is not when the chemical and turbulent time scales have the same order of magnitude.
Eddy Dissipation Concept (EDC) Magnussens's Eddy Dissipation Concept (EDC) [54], allows the taking into account of more complex kinetics mechanisms. The model assumes that chemical reactions occur in the fine turbulent scales. Fine-scales reactions are modeled through the solution of a PSR reactor, for which the starting conditions are represented by the composition

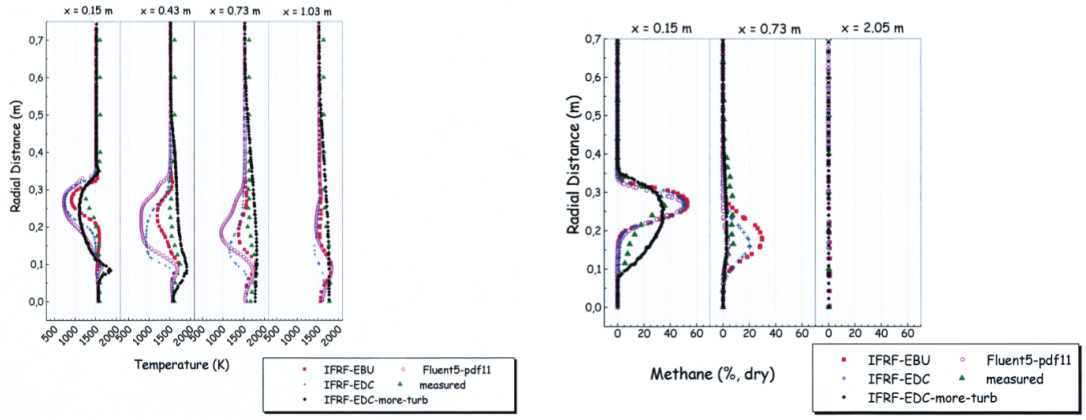

(a) (b)

Figure 3.6 – *Results from Mancini et al. [38]. Radial profiles of Methane and Temperature for several axial positions of the HiTAC configuration*

and temperature within the computing cell. Of course the EDC model is more time consuming if compared to the models seen above, as it requires the solution of the transport equations of each chemical species of the kinetic mechanism. Auto-ignition is taken into account in this model but it is not accurately predicted. However, the EDC certainly represents an evolution in predicting AI, with respect to the EBU or EDM models.

Results obtained with no-flamelet models in RANS Mancini et al. [38] simulated the HiTAC furnace belonging to the semi-industrial furnaces and described in section 3.1.1. Simulations were carried out by means of the EBU and EDC. In the configuration simulated, a central jet of vitiated air was injected at $85 m/s$. Fuel (methane) was injected by means of two nozzles at $100 m/s$. They carried out their simulations with the EBU, the EDC model, the Fluent-PDF model based on mixture fraction and an EDC-model modified, in order to account for dissipative effects of methane. The $k-\epsilon$ model was used to model turbulence. In figure 3.6, the results obtained in their simulations are shown. In particular radial profiles of methane and temperature for several axial positions in the burner are shown. As we can see, the methane rate of consumption is underestimated by all the models. Among the EBU, EDC and PDF model, no strong differences are observed. Temperature was underestimated due to the underestimation of methane consumption. The main reason of this failure in predicting the fuel-jet near zone, is due to the strong interactions between the jets of air and methane, which are not taken into account correctly by the model of turbulence used.

Krishnamurthy et al. [39] investigated numerically an oxy-flameless burner (described in section 3.1.1). Simulations were carried out with the EDC model for combustion and $k-\epsilon$ for turbulence modeling. Results are shown in figure 3.7, where temperature axial profiles of the combustion and flameless combustion states are compared against experimental data. In both cases, near the injection zone, where fresh gases are still mixing, temperature is not correctly predicted. This is a common failure in combustion prediction in RANS, where mixing zones are not correctly predicted and gradients of temperature are generally overestimated.

Flamelet based models

These models are all based on the resolution of Peter's flamelet equation [50]. A flamelet is a 1D approximation of a counter-flow diffusion flame, identified by its strain rate. Strain rate becomes of particular importance when dealing with highly-strained jets, as combustion can be affected by it.

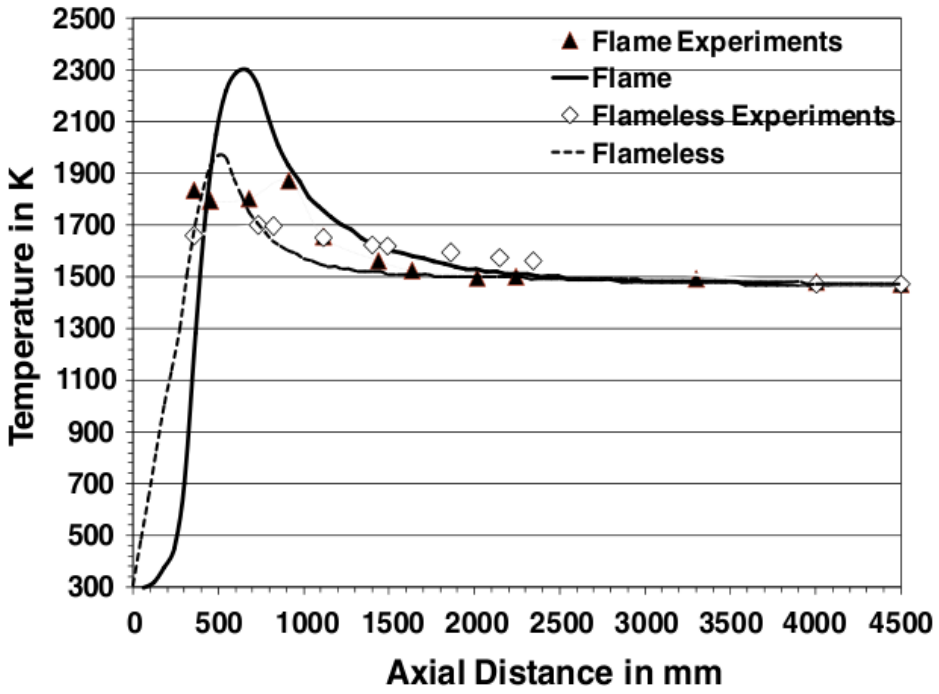

Figure 3.7 – *Axial profiles of temperature of the furnace investigated by Krishnamurthy et al. [39]. Numerical profiles are compared against experimental ones for the flame and flameless state*

Representative interactive flamelets (RIF) models The basic concept of the RIF approach is to couple the CFD code with a 1D flamelet solver. Physical quantities such as mixture fraction and pressure are sent to the 1D solver which calculates species and temperature values as a function of time and position. Such an approach was used by Coelho and Peters [55] in predicting the furnace investigated in [15] and [16] and presented in section 3.1.2. In this study, the RIF code calculated the flamelet at equilibrium so that auto-igniton was not taken into account. Coelho et al. focused their predictions on the fluid dynamics field of the flame. More specifically, the predictions of velocity and residence time (measured in[16]) are presented. In the work of Coehlo et al., axial velocity profiles are predicted qualitatively but lack in precision. In particular, the $k-\epsilon$ is not capable of correctly predicting the mixing between the fuel and air jets, thus overestimating the velocity at the first axial positions. More downstream, predictions are in fair agreement instead. The same lack of precision is also shown for the residence time in the vicinity of the burner, as it is underestimated.

Eulerian Particle Flamelet Model EPFM Pitsch et al. [56] showed that transient effects do not have an important effect on the prediction of species concentrations. Though this is not true for pollutant species such as NO. Indeed, the prediction for this kind of species relies also on the prediction of the residence times. In order to compute residence times, transient effects are taken into account. The Eulerian Particle Flamelet Model EPFM is the model used in order to accomplish this task. This model tracks the spatial and temporal evolution of the path of flamelets (within a combustion chamber for instance) and calculates the scalar dissipation as a function of time. In other words, the model is able to track the evolution of the transported flamelets in the flame. In their work, Dally et al. [40] used the EPFM model for combustion, coupled with $k-\epsilon$ to model turbulence. In this work, a flamelet code resolves the unsteady flamelet equations and it is coupled with the CFD code. Consequently, auto-ignition was taken into account. The FLUENT commercial CFD code was used to solve the mixture fraction and velocity field whereas EPFM was used to predict species and NO_x concentrations. In this work, it is shown that the EPFM model is a comprehensive model, able to account for several aspects

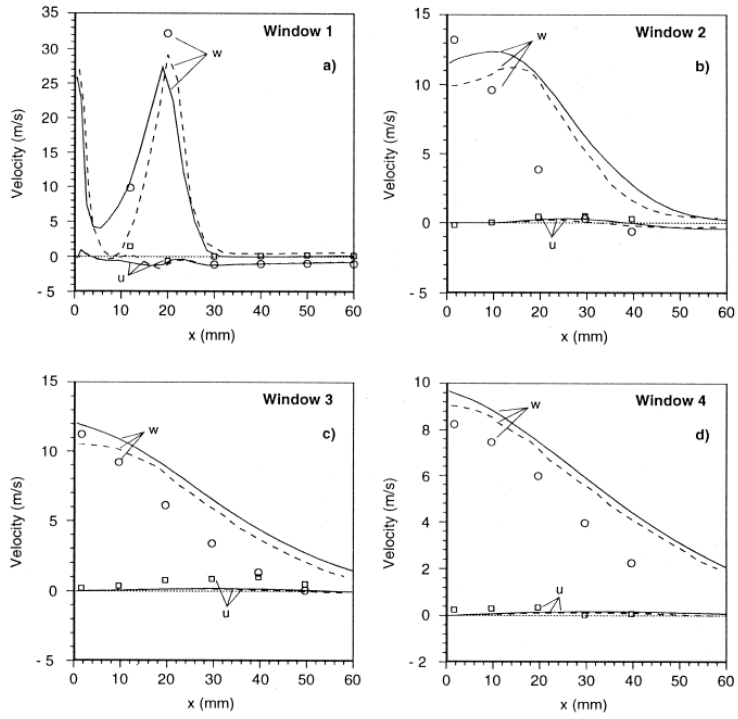

Figure 3.8 – *Axial velocity and radial velocity results from the simulations of Coehlo et al. [55] for several axial positions.*

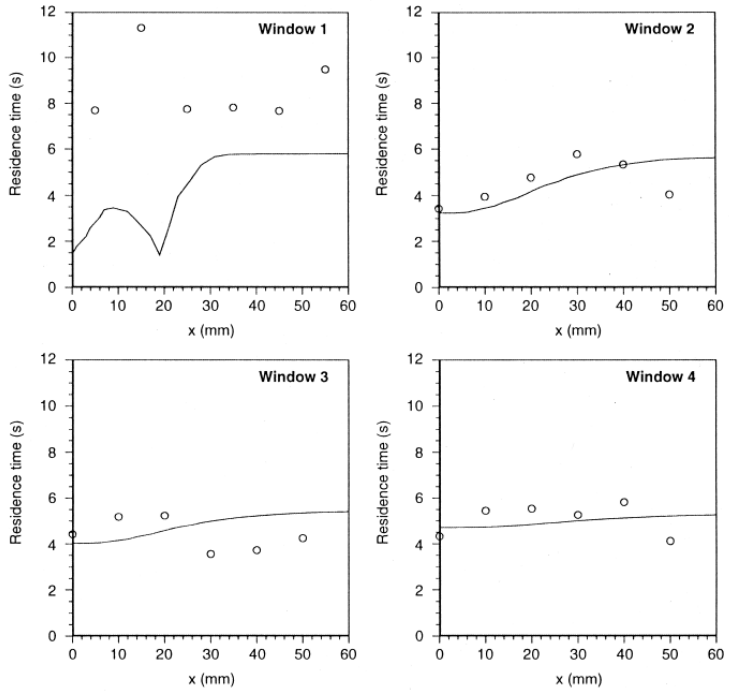

Figure 3.9 – *Residence time results from the simulations of Coehlo et al. [55] for several axial positions.*

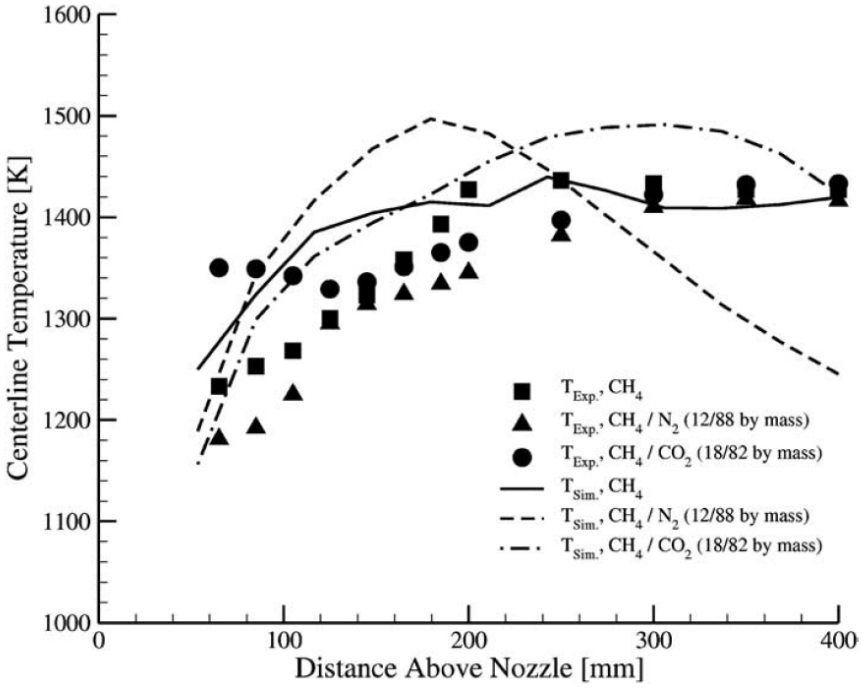

Figure 3.10 – *Temperature centerline predictions and experimental data for the case simulated by Dally et al. [40]. The effect of dilution with inert gases (CO_2 and N_2) is also investigated.*

of FC and to predict it correctly. The prediction of mean centerline temperature is shown in figure3.10 for the cases with pure methane and methane diluted with CO_2 and N_2. Correct results were obtained for the case with pure methane, above for the axial positions after 200 mm from the nozzle. For the case with CO_2 dilution the agreement was less satisfactory. Finally the largest gap was found for the case with N_2 dilution, but it was attributed to measurement uncertainty. But overall, satisfactory results were obtained.

3.2.3 State of the art in LES modelling of Flameless Combustion

At the beginning of this chapter, we gave an overview on the different turbulence description approaches. LES seems to be very promising as it offers a more precise description of the turbulent mixing, which is a critical factor in predicting FC. However, LES is certainly more costly than RANS. For this reason, the complexity and the accuracy of the combustion model should not considerably increase computational costs. It is also recalled that very few studies of LES in FC have been carried out. In this section some of the main models for LES will be presented, by putting emphasis on which aspects they account for and they do not in simulating FC.

Conditional Momentum Closure - CMC

The conditional moment closure model (Klimenko [57] and Bilger [58]) is a model which solves a transport equation for each conditional moment $(\overline{\rho Y_k|Z^*})$, where Y_k is the value of each species mass fraction and Z^* is the conditioned mixture fraction. Mean species mass fractions are retrieved by the following equations:

$$\bar{\rho}\tilde{Y}_k = \int_0^1 (\overline{\rho Y_k|Z^*}) p(Z^*) dZ^* \tag{3.1}$$

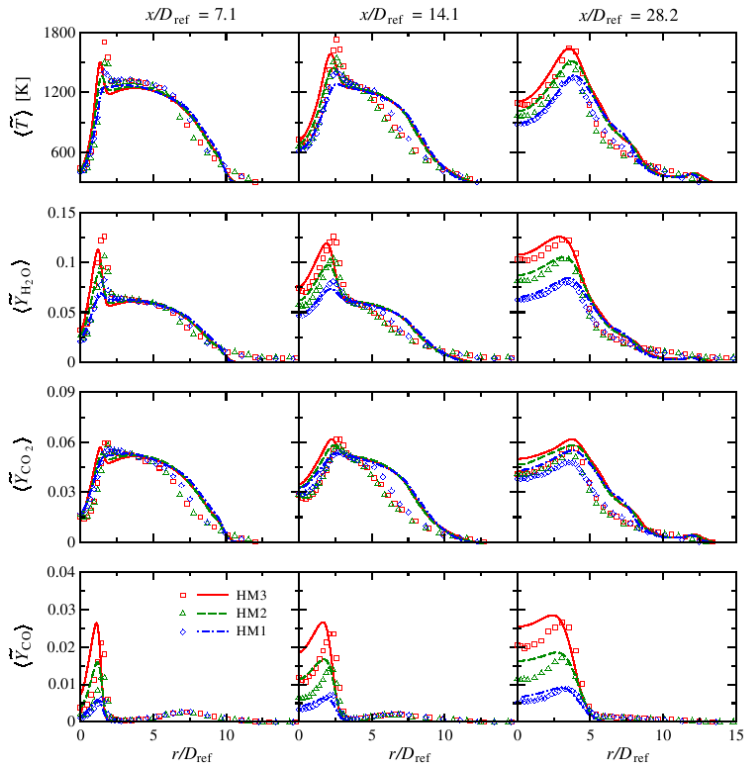

Figure 3.11 – *Numerical results of the radial profiles of T, CO, CO_2 and H_2O for three axial locations of the JHC burner. D_{ref} is the central jet diameter and is equal to* 4.25*mm. HM 1, 2 and 3 denote a different proportion of the O_2 and N_2 quantities.*

Computational costs are very high, as n_{z^*} X n_{Y_k} equations (where n_{Z^*} is the number of Z^* iso-surface and n_{Y_k} is the number of species) are solved. The model accounts for complex chemistry, diffusion flames combustion and auto-ignition. Despite a high computational cost, the model is certainly one of the most complete models for FC modeling. Examples of CMC used in LES can be found in Kronenburg et al. ([59], [60]). With respect to FC, an application of CMC in simulating the flameless JHC burner can be found in [61]. Results were overall quite satisfactory, so that CMC is considered a comprehensive model to simulate FC (although expensive).

Flamelet progress variable - FPV In this model, a database of steady flamelets at equilibrium is used. They were firstly presented by Pierce et Moin [62]. Flamelets at equilibrium are tabulated depending on mixture fraction Z and a progress variable. As flamelets are considered at equilibrium, auto-ignition is not taken into account. An example of FPV model used for FC was presented in Ihme et al.([63] and [48]). The JHC burner of Dally et al.[43] already described in 3.1.2 was simulated. To simulate the burner, an FPV model adapted to the ternary mixing is proposed; more precisely the flamelet database was a function of mixture fraction, strain and a variable which represents the mixing of the oxidizer with the burnt gases. The simulations were carried out for three different O_2 and N_2 proportion in the diluting mixture. Part of the results are shown in Fig.3.11, where the numerical results for the radial profiles of T, CO, CO_2 and H_2O for three axial locations are shown. Results are in very good agreement with the experimental results. No over-estimation of temperature in the reactive zone, typical of RANS simulation, is found.

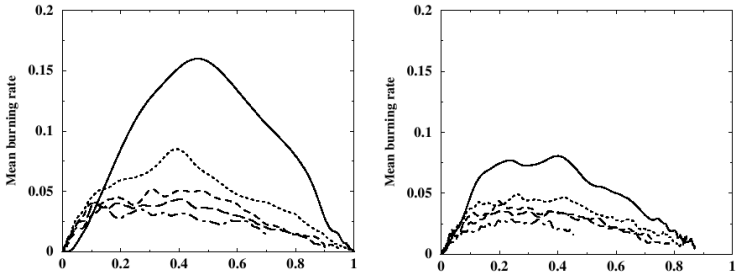

Figure 3.12 – *Mean burning rate versus mean progress variable of the DNS of the V-shape flame of Vervisch et al.[71] for several axial positions*

Flamelet Prolongation ILDM FPI/Flamelet generated manifold FGM

In FPI [64], the parameters of laminar premixed flames are tabulated depending on mixture fraction Z and the initial temperature T_u. Combustion progress is taken into account by a progress variable defined as:

$$c = \frac{Y_c}{Y^{eq}{}_c(Z)} \tag{3.2}$$

where $Y^{eq}{}_c(Z)$ is the equilibrium value of Y_c at Z. As far as Y_c is concerned, there is no unique definition and several forms were proposed. For instance, in Fiorina et al. [65] $Y_c = Y_{CO} + Y_{CO_2}$ whereas Galpin et al. [66] defined it as $Y_c = Y_{H_2O} - Y_H$. FGM models [67] use the same approach of FPI, by tabulating mono-dimensional laminar flamelets, either premixed or non-premixed ones. FGM were used in premixed [68], partially premixed [69] and non-premixed [70] flames.

Presumed conditional moments - FP-ILDM PCM-FPI

The PCM-FPI model is the combination between the FPI tabulation model aforementioned and the PCM model for turbulent combustion of Vervisch et al. [71]. The PCM model of Vervisch [71] accounts for turbulent fluctuations in LES. In PCM, conditional moments are not transported in the code but presumed. To represent turbulent fluctuations, a $\beta - PDF$ is used to account for the SGS fluctuations of c and Z. In order to see if this approach is valid, Vervisch et al. [71] and Bray [72] gave evidence that $\beta - PDF$ is a good approximation for c and Z fluctuations. In particular Vervisch realized a DNS of a V-shape flame. In figure 3.12 a part of the results obtained is shown. The mean burning rate is plotted against the mean progress variable. Several plots are realized for 5 axial positions. It is evident that the mean burning rate has an almost parabolic shape, and so the hypothesis of approximating the fluctuations with a gaussian shape PDF can be considered valid. The other feature of the $\beta - PDF$ (either of Z and c) is that it depends on two parameters, namely the mean value of the variable and its segregation factor. The segregation factor measures the level of fluctuations. The segregation of Z is written as:

$$S_z = \frac{\tilde{Z}_v}{\tilde{Z}(1-\tilde{z})} \tag{3.3}$$

where $\tilde{Z}_v$ is the variance of $\tilde{Z}$ and it is defined as:

$$\tilde{Z}_v = \tilde{ZZ} - \tilde{Z}\tilde{Z} \tag{3.4}$$

where $\tilde{f}$ denotes the favre−mass weighted− filter for the variable f. Segregation for c follows the same form.
However, if on the one hand conditional moments of $P(Z)$ can be easily calculated, on the other hand fluctuations of c also depend on the fluctuation of Z, i.e. $P(c^*) = P(c|Z)$. In a possible

simplification of the model, one can consider that $P(c|Z) \simeq P(c)$, i.e. that the fluctuations of c are independent from the ones of Z. This hypothesis can be disputed as it is not always valid, specifically during the AI in non-premixed flames, where $P(c|Z) \neq P(c^*)$, as shown by Michel et al. in ADF-PCM [73].
Let us now see how the two models are coupled together. From the FPI table, the value of $Y_c^{eq}(Z)$, the reaction rate $\dot{\omega}_{Y_c}(Z,c)$ and species $Y_i(Z,c)$ are retrieved by means of the mean values of $\tilde{Z}$ and $\tilde{c}$. The mean value of the equilibrium value of Y_c is calculated as follows:

$$\tilde{Y}_c^{eq}(\tilde{Z}, S_z) = \int Y_c^{eq}(Z) P(Z, \tilde{Z}, S_z) dZ \tag{3.5}$$

From now on, we will simplify the writing of the equations and for $P(Z, \tilde{Z}, S_z)$ we will simply write $P(Z)$. On the other hand $\widetilde{\omega}_{Y_c}$ is calculated as follows

$$\widetilde{\omega}_{Y_c}(\tilde{Z}, S_z, \tilde{c}, S_c) = \int_0^1 \int_0^1 \omega_{Y_c}^{FPI}(Z,c) P(c|Z) P(Z) dc dZ \tag{3.6}$$

Species are calculated in the same way:

$$\tilde{Y}_i(\tilde{Z}, S_z, \tilde{c}, S_c) = \int_0^1 \int_0^1 Y_i^{FPI}(Z,c) P(c|Z) P(Z) dc dZ \tag{3.7}$$

As said previously, this formulation is further simplified considering that $P(c|Z) \simeq P(c)$. In this case, equations 3.6 and 3.7 may be re-written as follows:

$$\widetilde{\omega}_{Y_c}(\tilde{Z}, S_z, \tilde{c}, S_c) = \int_0^1 \int_0^1 \omega_{Y_c}^{FPI}(Z,c) P(c) P(Z) dc dZ \tag{3.8}$$

$$\tilde{Y}_i(\tilde{Z}, S_z, \tilde{c}, S_c) = \int_0^1 \int_0^1 Y_i^{FPI}(Z,c) P(c) P(Z) dc dZ \tag{3.9}$$

In the 2nd order PCM, $P(c)$ is given by a $\beta-$PDF defined by the equations of Y_c and its variance v_{Y_c}. Conversely, for PCM at 1st order, $P(c)$ is approximated as $P(c) \sim \delta(c - \hat{c})$.

2nd order PCM was applied with success to turbulent premixed flames in [66]. Enthalpy variation is not taken into account in the original version of the model, but was added by Fiorina in [74]. PCM was adapted for auto ignition by Domingo et al. [75] considering both homogeneous auto-igniting reactors and premixed flames. No study on FC using these approaches has been published at present to our knowledge.

Approximated Diffusion Flame Presumed Conditional Moments - ADF-PCM

In order to reduce the computational time required to build auto-igniting flamelet databases, the ADF-PCM model was introduced [76]. In a first step, the reaction rate of auto-igniting homogeneous reactors is tabulated as a function of mixture fraction and progress variable Y_c. This reaction rates ω_{Y_c} so calculated is used in Peter's flamelet equation [50], for Y_c:

$$\frac{\partial Y_c}{\partial t} = \omega_{Y_c} + \chi \frac{\partial^2 Y_c}{\partial Z^2} \tag{3.10}$$

It is underlined that only the flamelet equation for the progress variable is used. Compared to PCM-FPI, using flamelets equations allows to introduce the strain rate a as input parameter of the table. ADF$-$PCM uses the PCM approach to account for fluctuations of Z. In its first version, the strain rate was uniform in the cell. The fluctuations of a were added in [73], by using a presumed PDF of a. ADF-PCM takes into account auto-ignition and is suitable for diffusion flames. A significant limit in the usage of ADF-PCM in FC is that flamelet auto-ignition occurs only if flamelet boundary conditions favor AI. As a matter of fact, boundary conditions for the ADF flamelet database are retrieved from the boundary conditions of the

3D test case to simulate. If the temperature of both air and fuel streams are not high enough to provoke auto-ignition spontaneously, ADF-PCM can not be used. This point will further be discussed in section 3.3.2. Concerning enthalpy losses, they are not accounted for in ADF-PCM, but they could be. Development in this sense will be carried out retaining the developments achieved in this thesis. This model was used in RANS ([76],[73]) and first applications in LES were proposed by Tillou in his PhD thesis [77] and in [78].

Thickened flame - Large eddy simulation - TFLES

TFLES [79] has been developed in order to overcome the problem of capturing the flame front thickness in premixed flames, which would require cells smaller than the flame front, i.e. $0.1 - 0.01mm$ [18]. It has been developed for premixed combustion. In this model, the flame is artificially thickened by a factor F. Some critical aspects of the model arise for large values of F in diffusion flames and auto-ignition conditions. Besides, as the reaction rate is multiplied by a factor F, the ignition delay and the reaction rate are tied to this factor. Indeed, a large value of F can result in a strong modification of the flame itself. Furthermore, a transport equation for each of the species must be solved in the CFD code. In fact TFLES is limited by the number of species, so that using complex chemistry to account for AI becomes CPU demanding. Subgrid fluctuations are not taken into account as the homogeneity hypothesis in the cell is used. The main advantage of the model is certainly its simplicity if compared to more complex models such as CMC, and its ability to qualitatively reproduce any type of combustion regime. However, accurately predicting AI and diffusion flames still remains a challenge for the model.

Diluted-homogeneous-reactors - DHR

In its first version DHR (in homogeneous combustion) was developed to model gas-turbine combustion and it was developed by Michel and Colin in the frame of the KIAI project. In this first version, the model was coupled with the premixed flame tabulated model ECFM-LES model [80]. In this PhD thesis, the model was used without ECFM-LES and adapted to turbulent combustion by accounting for mixture fraction fluctuations. The model is very close to the PCM-FPI model as it uses a tabulation built on homogeneous reactors. However, the innovative feature of this model is that the initial composition in the homogeneous reactor is diluted with burnt gases and the variables involved in combustion are tabulated depending on the level of the dilution α. It also allows to take into account enthalpy losses and auto-ignition.

3.3 Retained approach and aim of the thesis

3.3.1 Aim of the thesis

This chapter started with a brief presentation of all the turbulence tools available. It was reported that, since the spreading of numerical techniques in research, RANS is largely used due to its qualitative results and its limited computing time. It was argued though that in flameless combustion, the ternary mixing of burnt gases, fuel and air was piloted by turbulence. This point represents a critical factor in correctly predicting FC, as a high quality prediction of turbulence is needed. Of course, it does not mean that with RANS, correct results can not be obtained (results in agreement with experimental data were obtained in [40] for the furnace presented in [15], see Fig.3.10). However, it is largely accepted that LES represents a more reliable tool to predict mixing [48]. The present thesis was carried out based on these observations. Being both LES and FC quite recent, to date, very few works have been carried out in predicting FC in the LES context. Apart from those of Ihme et al.([48] and [49]), we can

also mention the works of Vicquelin et al.[81], where a flameless furnace was simulated by means of tabulated chemistry. For this reason, in this thesis, we simulated FC by using LES for turbulence description. The efforts of this thesis were addressed both towards the combustion model and the pollutant modeling. The FC furnace simulated in this thesis was the one presented by Verissimo et al.[14]. It is a 10kW small furnace which operates with internal recirculation of burnt gases. Results concerning combustion are presented in chapter 3 while the ones concerning NO prediction are presented in chapter 4. In the next section, the models chosen to simulate FC in this thesis are presented.

3.3.2 Retained approach for this thesis

The following requirements should be taken into account for a combustion model for flameless combustion:

- time consumption: LES is certainly more expensive than RANS, so that only small size furnaces ($< 1m$) can be simulated within reasonable CPU times at present. In order to reduce the CPU time, the combustion model should present a compromise between accuracy and simplicity of the algorithm, with a low number of species and variables transported. For this reason the CMC model, although accurate and reliable, was excluded for the simulations in this work. From this point of view, all the models based on tabulated chemistry such as FPI-PCM and DHR are less time consuming.
- diffusion flame structure and strain effects: in order to favor internal recirculation of gases, high momentums jets are usually used in FC. For this reason, high velocity jets and highly strained jets are present in FC furnaces. Furthermore, the characteristics of FC are closer to the ones of non-premixed flames rather than premixed flames, as often fuel and air are usually not premixed before combustion. Consequently, a comprehensive model for FC should account for the strain notion. With regard to the TFLES model, the effect of the thickening on a diffusion flame is not clearly understood. During this thesis some tests were carried out to assess the effect of thickening the flame front in partially premixed diffusion flames. The conclusions of that first study were that thickening the flame can have a large impact on the flame structure, when using a standard mesh resolution. For this reason, the model was discarded. In this work, the DHR approach was retained for its simplicity. Due to this simplicity, it does not account for strain. As will be shown in the next section, acceptable results were still obtained, but the absence of the effect of strain was identified as a limitation of the model.
- auto-ignition: in order to predict auto-ignition, complex chemistry should be taken into account in the model. Nowadays, tabulated chemistry represents a good compromise between a correct description of AI and contained CPU times. In models such as FPI-PCM or DHR, the number of transported species is limited to a few species (on the order of ten species), although the AI is correctly described in the complex chemistry tabulation. On the other hand, models such as TFLES, would allow describing AI accurately only by transporting all the species of the entire kinetics mechanism (53 species for the GRI 3.0 mechanisms for instance [82]), which is not feasible in terms of CPU time requirements. With regard to flamelet-based models such as ADF-PCM or FPV, where flamelets consider a binary fuel-air system, auto-ignition is provoked by the high temperature and high pressure conditions of fuel and air streams. These favorable conditions are not found in most FC furnaces. For instance, in the case of Verissimo et al.[14] a central jet of air at $673K$ and methane at ambient temperature are injected in atmospheric pressure. These conditions do not favor spontaneously AI (AI only occurs because of diluent gases) and binary fuel-air flamelets would not auto-ignite. As a consequence, it is necessary to account for diluent burnt gases in the flamelet structure. This point will be further treated in the next point.
- ternary mixing: ternary mixing is typical in FC as three streams, namely fuel, air and burnt gases, take part in the combustion process. In particular, it is necessary to account

for the diluent burnt gases in the diffusion flame structure: this point was clearly demonstrated in the works of Ihme et al.([48] and [49]) where an FPV model was modified to account for the mixing of diluent burnt gases. In the previous point we explained that this becomes necessary as diluent gases are responsible for the AI of the fresh gases. For this reason, ADF-PCM does not seem to be suitable for FC, unless it is modified with a methodology like the one proposed by Ihme. On the other hand, the DHR proposed in this thesis, has been developed exactly in this sense, were fresh gases are diluted with hot burnt gases at equilibrium. This point is further explained in chapter 3.

- enthalpy losses: FC furnaces are built to exchange a large amount of heat with the surrounding environment. Consequently, the burnt gases are strongly under-adiabatic and enthalpy losses need to be taken into account in combustion models. In chapter [3] it will be shown that for the case of Verissimo et al.[14], the burnt gases are 750K below their adiabatic temperature. Including enthalpy losses in flamelets models was already proposed in Netzell et al.[83] or Ihme et al.[48], but only for steady state to our knowledge. To conclude, including enthalpy losses in auto-igniting flamelets might be possible but it is difficult.

In table 3.3, all the features of the models available, are summarized. To conclude this part, the model used in this thesis was the DHR. It has four advantages:

- it is suitable for LES
- it represents AI accurately at a low CPU time
- it represents the ternary mixing
- it accounts for large enthalpy losses

Though, as it is based on homogeneous reactors, it does not account for strain effects. In chapter 3 this lack in the description of combustion will be also investigated.

Burner	Experimental work	RANS	LES
HEC	Battaglia [35]	Battaglia [35] EDC	
HiTAC	Awosope [36]	Mancini [38] EBU,EDC	
OxyFlam	Krishnamurthy [39]	Krishnamurthy [39] EDC	
FLOX	Wunning [13]	Wunning [13] 1step Arrhenius approach	
ENEL	Galletti [28]	Galletti [28] EDC	
Plessing	Plessing [15]	Coehlo [55], RIF, Plessing [40]EPFM	
JHC	Dally [43]		FPV modified[48],[49]
Verissimo	[14]	Verissimo [84] EDC	DHR

Table 3.2 – *A schematic representation of the burners in literature, depending on the categories chosen by the authors*

Model	Tabulation database	Auto-ignition (yes/no)	Enthalpy losses (yes/no)	Ternary mixing	Suitable for	Computing time
CMC	-	Yes	Yes	No	DF	Very very high
RIF	-	Yes	Yes	No	DF	High
TFLES	-	No	Yes	No	PF	Low
PCM-FPI	PF and HR	Yes	Yes	No	PF	Low
DHR	Diluted homogeneous reactors	Yes	Yes	Yes	DF	Low
ADF-PCM	Flamelets from homogeneous reactors	Yes (at hight T)	No	No	DF	Low
FPV from [48]	Flamelets	Yes	No for unsteady	Yes	DF	Low

Table 3.3 – *Comparison among the models considered to model FC (DF = diffusion flames; PF = premixed flames)*

Large Eddy Simulations of flameless combustor

4

In this chapter, the article Large Eddy Simulations of a small-scale flameless combustor by means of diluted homogeneous reactors *accepted for publication in the journal* Flow Turbulence and Combustion *is reported. In the article, the diluted homogeneous reactors DHR model is presented: it was developed in order to account for the ternary mixing and the enthalpy losses. The article is divided into three parts. In the first part, the model is presented; in the second part the model is coupled with ADF-PCM in order to validate the auto-ignition in a 1D flamelet structure. Finally in the third part, the model performances are analyzed in two 3D configurations, Flame D of Sandia and the FC combustor from the works of Verissimo et al.*

4.1 Abstract

A new model for Flameless Combustion (FC) based on the tabulation of diluted homogeneous reactors (DHR) is presented. This model is developed within the Large Eddy Simulations (LES) approach because LES has a good potential for correctly predicting the ternary mixing of FC. In DHR, a ternary mixture of fuel, air and burnt gases at equilibrium is considered as an initial condition for the reactor calculations. The auto-ignition of this mixture is then tabulated as a function of the input parameters which are mixture fraction, fresh gases temperature, dilution fraction, progress variable and enthalpy loss. The enthalpy loss is introduced by decreasing the temperature of the diluting burnt gases. The DHR model is first evaluated over the partially premixed Sandia Flame D. Correct results are obtained for this flame, although CO is overestimated by the model. This discrepancy is attributed to the usage of homogeneous reactors which impedes to account for the influence of scalar dissipation. Secondly, the flameless configuration of Verissimo et al., characterized by a strong enthalpy loss due to wall heat losses, is used to assess the performance of the model. Combustion results are found in correct agreement for temperature and major species. The largest discrepancies are found for CO again, although the axial shape for this species is correctly predicted.

4.2 Introduction

Reducing pollutant emissions and improving burners efficiency has brought to the development of new combustion technologies. Among these new technologies, flameless combustion (FC) takes place as one of the most promising [13, 19]. In flameless combustion, the air and fuel jets are strongly diluted by means of external or recirculated burnt gases. A first consequence is that combustion occurs in a lean oxygen environment, therefore limiting the temperature peak and reducing nitrogen oxides (NO_x) and soot emissions. A second consequence is that the reactive zone is shifted towards low scalar dissipation rate values [48] leading to more diffused reactions and smoother temperature gradients. Decreasing temperature gradients is in

fact sought for in many industrial applications such as steel or glass [13]. FC was investigated both experimentally and numerically. Coelho and Peters [55] used an Eulerian Particle Flamelet model to investigate numerically a furnace experimentally characterized by Plessing et al.[15]. Root mean square (RMS) and mean velocity fields were found in good agreement with experiments, whereas some discrepancies were found for the residence time prediction in the vicinity of the burner. Dally et al.[43] investigated a jet in hot coflow (JHC) burner. For this burner, Kim et al.[61] used a conditional moment closure (CMC) formulation to predict temperature, main species and NO mass fraction. Results were in good agreement with the experimental results. The same burner was investigated numerically by Christo et al.[85] using the eddy dissipation concept (EDC) model coupled with complex chemistry and a mixture fraction/PDF model formulation. The mixture fraction/PDF model performed poorly in predicting the JHC main species. Conversely, the EDC model was able to provide improved results. The authors explained that the poor performance of the mixture fraction/PDF model could be attributed to the single-mixture fraction formulation, which is not suitable for three streams configurations. Verissimo et al. experimentally investigated a small-size FC burner [14]. It was simulated by the same authors in [86] employing the EDC model and a joint composition pdf transport model [87]. Results were in fair agreement with experimental data, although some discrepancies were found on temperature for both models. Globally, the joint pdf model performed better than the EDC in predicting CO. The burner was also investigated by Cuoci et al.[88] employing a kinetic post-processing KPP method. The agreement with the experiment was correct for major species, less so for temperature and CO. The above flameless studies have been performed using the Reynolds Averaged Navier-Stokes (RANS) approach which remains today the standard approach in the industry of furnaces because of its affordable CPU-times. At the same time, as demonstrated for instance in [55], RANS has a limited ability to correctly predict the mixing of fuel, air and burnt gases because the turbulence models employed, often based on a k-ϵ description, fail to describe the features of complex turbulent flows. Like for turbulence, the complete flame structure needs to be modeled in RANS. In the case of furnaces, predicting the combustion mode is difficult because of the aforementioned ternary mixture and because only mean and variances of passive scalars are available. For these reasons and as illustrated in the previous examples, RANS predictivity on furnace applications remains limited.

Alternatively, LES could be a promising tool for furnace applications because it has a better ability to predict complex turbulent flows, even using rather simple turbulence models like the Smagorinsky model [89]. The reason for that is that in LES, large flow structures are directly resolved on the LES mesh, while modeling is only required at the SGS level. Therefore, the modeling assumptions made on the complete flow in RANS are limited to the SGS level in LES. This ability has been largely demonstrated in gas turbine applications, like in Eyssartier et al.[90] and Hermeth et al.[91]. As gas turbines dimensions are fairly small, such LES are today becoming accessible to engine manufacturers thanks to the constant decrease of super-computing costs. On the contrary, LES calculations of flameless furnaces are still computationally expensive, due to the very large dimensions of the test cases involved. As done today in RANS, LES of a single burner will consequently be the first target application for burner designers in the near future. Such calculations are aimed at understanding and improving the burners design, particularly in the case of flameless combustion where an accurate control of the ternary mixing is required. Only a few flameless configurations have been studied in LES. In the work of Duwig et al. [92], a flameless gas turbine experimentally investigated by the same authors was simulated in LES. In this experiment, a mixture of propane and preheated air is injected in a cylindrical combustion chamber through a premixing pipe. Like in most such devices, although the injected air is preheated, the temperature of the fuel/air mixture that is formed is too low to promote auto-ignition. Therefore, using standard homogeneous reactor (HR) calculations like in the ADF-PCM model for instance ([76],[73]), does not allow to ignite the mixture and sustain combustion. This is why a tabulated combustion model based on the calculation of homogeneous reactors diluted with adiabatic burnt gases at equilibrium was proposed in [92]. The LES matched correctly the experimental velocity field in cold operation and succeeded in reproducing the flameless combustion mode, but no quantitative profiles were provided for species or temperature. In the works of Ihme et al.[48, 49], the JHC burner

[43] is simulated using an extended FPV model where an additional conserved scalar W is introduced. This scalar allows to define the proportions of air and burnt gases in the oxidizer stream. A flamelet library is built using the standard mixture fraction, scalar dissipation rate and progress of reaction plus variable W. The authors showed that a single mixture fraction model is not able to reproduce correctly the main species profiles and that it is necessary to use the extended three streams flamelet model. Hence, from this work, there is some evidence that in order to correctly predict flameless combustion, it is necessary to account for the ternary mixing between fuel, air and diluent gases in the combustion model.
In the present paper, an alternative combustion model for LES of flameless combustion is proposed. The model was developed based on three major requirements of flameless combustion. First, as observed in [48, 92, 49], flameless combustion can only be attained if fuel and/or air are strongly diluted with burnt gases prior to combustion. Therefore, the model should account for the ternary mixture of fuel, air and diluent burnt gases. Secondly, as outlined in many flameless studies, this ternary mixture is introduced at temperatures that are larger than the auto-ignition temperature. This means that the model should correctly reproduce the auto-ignition delay and heat release of such mixtures. Finally, unlike in the JHC burner, flameless burners are designed to exchange a large amount of heat for industrial purposes (glass or steel for instance). As a consequence, the air and fuel streams are diluted with highly under-adiabatic burnt gases, which has a major impact on the reactivity of the mixture. This under-adiabaticity also needs to be accounted for in the model. The diluted homogeneous reactor (DHR) model proposed in this paper satisfies these requirements. To account for the ternary mixture, it relies on the calculation of homogeneous reactors initially composed of fuel, air and hot burnt gases at equilibrium like in the model proposed by Duwig et al.[92]. These reactor calculations are performed a priori and tabulated like in the ADF-PCM model ([76, 73]) or Flamelet Progress Variable (FPV) ([48],[62]) approaches. This choice allows to retain the ability of complex fuel/air mechanisms to accurately predict the auto-ignition delay and heat release while maintaining a low CPU cost. Unlike in the model of Duwig, the enthalpy loss of the mixture is accounted for by considering various levels of enthalpy for the diluting burnt gases, as already proposed by Wang et al. [93] for premixed flames.
The paper is organized as follows. Section 4.3 presents the DHR mathematical formulation. The LES transport equations are first presented, followed by the definition of the DHR initial conditions. The tabulation methodology of the auto-ignition trajectories is then explained. The homogeneous DHR table is finally filtered to get the mean species reaction rate, and the calculation of its input parameters from the transported LES scalars is explained. The DHR reaction rate expression is first evaluated in Section 4.4 on unsteady laminar counter-flow diffusions flames to evaluate its ability to reproduce the auto-ignition of a non premixed mixture. A first evaluation of the DHR model is performed on Sandia flame D in Section 4.5. Although the characteristics of this flame do not meet all the flameless criteria, it shares with flameless combustion an important characteristic: the turbulent mixing of fuel, air and burnt gases. Besides, this flame is very well documented, which allows an accurate comparison between LES and experiment. The model is finally applied to the flameless burner of Verissimo in Section 4.6. This configuration was chosen because it is one of the rare flameless burners which presents, unlike the JHC burner for instance, a high enthalpy loss of the recirculated burnt gases like in a real furnace. Finally Section 4.7 draws the main conclusions.

4.3 The DHR combustion model

4.3.1 The filtered LES equations

The reactive Navier-Stokes equations considered are those of species mass fractions, momentum, energy and mixture fraction. In LES, these equations are filtered using a spatial filter $\bar{\cdot}$, so that $f = \bar{f} + f'$. For convenience, a Favre filter defined by $\tilde{f} = \frac{\overline{\rho f}}{\bar{\rho}}$ is also introduced.

Applying this filtering, the LES equations for a species mass fraction $\tilde{Y}_k$, mean mixture

fraction $\tilde{Z}$ and its variance v_Z, velocity $\tilde{u}$, and total energy $\tilde{E}$, read:

$$\frac{\partial \bar{\rho}\tilde{u}}{\partial t} + \nabla \cdot (\bar{\rho}\tilde{u}\tilde{u}) = \nabla \bar{P} + \nabla \cdot \left(\bar{\tau} + \bar{\tau}^t\right) \tag{4.1}$$

$$\frac{\partial \bar{\rho}\tilde{E}}{\partial t} + \nabla \cdot \left((\bar{\rho}\tilde{E} + \bar{P})\tilde{u}\right) = -\nabla \cdot \left[-\overline{u\tau} + \bar{q} + \bar{q}^t\right] + \bar{\rho}\widetilde{\dot{\omega}}_T + \bar{Q}_w \tag{4.2}$$

$$\frac{\partial \bar{\rho}\tilde{Y}_k}{\partial t} + \nabla \cdot \left(\bar{\rho}\tilde{u}\tilde{Y}_k\right) = -\nabla \cdot \left[\bar{J}_k + \bar{J}_k^t\right] + \bar{\rho}\widetilde{\dot{\omega}}_k \tag{4.3}$$

$$\frac{\partial \bar{\rho}\tilde{Z}}{\partial t} + \nabla \cdot \left(\bar{\rho}\tilde{u}\tilde{Z}\right) = \nabla \cdot \left[\bar{\rho}\left(D + D_t\right)\nabla \tilde{Z}\right] \tag{4.4}$$

$$\frac{\partial \bar{\rho} v_Z}{\partial t} + \nabla \cdot (\bar{\rho} v_Z \tilde{u}) = \nabla \cdot \left(\bar{\rho}\left(D + D_t\right)\nabla v_Z\right) + 2\bar{\rho}\left(D + D_t\right)(\nabla \tilde{Z})^2 - 2\bar{\rho}\tilde{\chi}_Z \tag{4.5}$$

In these equations $\bar{\rho}$ is the filtered density, defined as the sum of the transported species partial densities. In the momentum and energy equations, (4.1) and (4.2), $\bar{\tau}$ represents the filtered stress tensor for a Newtonian fluid. It is modeled as:

$$\bar{\tau}_{ij} = 2\mu\left(\tilde{S}_{ij} - \frac{1}{3}\delta_{ij}\tilde{S}_{nn}\right) \tag{4.6}$$

where μ is the molecular viscosity given as a function of the filtered temperature using Sutherland's law. δ_{ij} is the Kronecker's index while the rate of strain $\tilde{S}_{ij}$ is defined as $\frac{1}{2}\left(\frac{\partial \tilde{u}_j}{\partial x_i} + \frac{\partial \tilde{u}_i}{\partial x_j}\right)$. The term $\bar{\tau}^t = \bar{\rho}\widetilde{u}\widetilde{u} - \bar{\rho}\tilde{u}\tilde{u}$ is the non-resolved turbulent flux for the momentum equation. Its expression is modeled using Boussinesq's approximation:

$$\bar{\tau}_{ij}^t = 2\bar{\rho}\nu^t\left(\tilde{S}_{ij} - \frac{1}{3}\delta_{ij}\tilde{S}_{nn}\right) \tag{4.7}$$

For all the calculations presented in this work, ν_t is modeled using Smagorinsky's model [89].

$\tilde{E}$ represents the sum of the sensible energy $\tilde{e}_s$ and resolved kinetic energy. $\tilde{e}_s$ can be deduced as:

$$\tilde{e}_s = \tilde{E} - \frac{1}{2}\tilde{u}^2 - \frac{\bar{P}}{\bar{\rho}} \tag{4.8}$$

Knowing the filtered species mass fractions $\tilde{Y}_k$ and sensible energy, the filtered temperature $\tilde{T}$ can be deduced. In the energy Eq. (4.2), $\bar{q}$ and $\bar{q}^t$ represent the filtered molecular and turbulent heat fluxes. They are both modeled using Fourier's expression, leading to a total flux:

$$\bar{q} + \bar{q}^t = -(\bar{\lambda} + \lambda^t)\nabla \tilde{T} + \sum_{k=1}^{N}(\bar{J}_k + \bar{J}_k^t)\tilde{h}_{s,k} \tag{4.9}$$

where $\bar{\lambda} = \frac{\mu \bar{C}_p}{Pr}$ is the thermal molecular conductivity and $\lambda^t = \bar{\rho}\frac{\nu_t \bar{C}_p}{Pr^t}$ the turbulent thermal conductivity. $\tilde{h}_{s,k}$ is species k sensible enthalpy while $\bar{J}_k$ and $\bar{J}_k^t$ are the filtered species molecular and turbulent fluxes respectively. These latter terms are modeled using a Fickian law:

$$\bar{J}_k + \bar{J}_k^t = -\bar{\rho}(D_k + D_k^t)\nabla \tilde{Y}_k \tag{4.10}$$

where $D_k = \frac{\mu}{\bar{\rho} Sc_k}$ is species k molecular diffusivity and $D_k^t = \frac{\nu^t}{Sc_k^t}$ its turbulent diffusivity. In the present calculations, we use $Sc_k = Pr = 1$ and $Sc_k^t = Pr^t = 0.6$. The term $-\overline{u\tau}$ in Eq. (4.2) represents the viscous dissipation term, modeled as $-\tilde{u}(\bar{\tau} + \bar{\tau}^t)$. The last term $\bar{Q}_w$ represents

the heat flux at walls. It is modeled using a thermal wall-law along with the dynamic wall-law used in the momentum equations. Its equation reads:

$$\bar{Q}_w = \frac{\rho_w C_{p,w} u_\tau (T_w - \tilde{T})}{T^+} \tag{4.11}$$

where u_τ, ρ_w and $C_{p,w}$ are the friction velocity, density and constant pressure specific heat at the wall respectively. T^+ is calculated as follows:

$$y^+ \leq 11.445 : \qquad T^+ = Pr\, y^+ \tag{4.12}$$

$$y^+ > 11.445 : \qquad T^+ = k_w^{-1} Pr^t \ln(F_w y^+) \tag{4.13}$$

where $k_w = 0.41$ and $F_w = 2.96$. y^+ is the non-dimensional wall distance calculated as:

$$y^+ = \frac{y_w u_\tau}{\nu_w} \tag{4.14}$$

where y_w is the node distance from the wall and ν_w is the molecular viscosity at T_w. This approach, although not as accurate as a direct resolution of LES equations at walls, is much cheaper in terms of CPU cost as it avoids to use an extremely fine mesh refinement at walls. Results presented in Section 4.6, also suggest that this approach is sufficient for the configuration considered here.

In species equations, $\widetilde{\omega}_k$ represents the species chemical reaction rate, closed with the DHR combustion model as presented in Section 4.3.7. The heat release rate $\widetilde{\omega}_T$ in the energy equation is directly deduced form $\widetilde{\omega}_k$:

$$\widetilde{\omega}_T = \sum_{k=1}^{N} \widetilde{\omega}_k h_k^0 \tag{4.15}$$

where h_k^0 is the enthalpy of formation of species k. Eq. (4.4) for the mean mixture fraction $\tilde{Z}$ is similar to that of species equations, apart that it contains no source term, Z being a passive scalar. Equation (4.5) for its variance v_Z is modeled as in [77]. The second term on the right-hand side of Eq. (4.4) represents the source of variance by the mean gradients, while the last term is the scalar dissipation $\tilde{\chi}_Z$ modeled using the relaxation expression $\tilde{\chi}_Z = C_0 \frac{\nu_t}{\Delta x^2} v_Z$, where Δx is the local cell size and C_0 is a modeling constant set equal to 1.

4.3.2 The DHR initial composition

In the DHR model auto-ignition trajectories of homogeneous reactors are tabulated. At elevated pressure and temperature, a mixture of fuel and air will usually auto-ignite, a property already exploited in tabulated models like TKI [94] for piston engine applications and ADF-PCM [73] for high temperature non premixed flames. For furnace or aeronautic conditions, the fresh gases temperature is usually too low to allow auto-ignition, which is also a desired property for safety. At these conditions, flame reactions are triggered by the dilution of the incoming fresh mixture with recirculated (or external) burnt gases. The idea of DHR is to follow auto-ignition trajectories triggered by the dilution of the fresh mixture with burnt gases. Although dilution of premixed flames [93] could be considered for this purpose, we choose here homogeneous reactors for three main reasons: first, it allows to describe the auto-ignition process which can be important in some burner technologies like in flameless; second, homogeneous reactors are the easiest and fastest model reactors to use; third, homogeneous calculations allow to use detailed chemistry mechanisms containing hundreds of species and thousands of reactions, which makes it attractive when studying the impact of fuel formulation on the heat release and pollutants. The fresh gases are composed of fuel and air. For these two components, their respective total enthalpies $H_F(Y_i{}^F, T_F)$ and $H_A(Y_i{}^A, T_A)$ are introduced, where T_F and T_A are fuel and air temperatures respectively while $Y_i{}^F$ and $Y_i{}^A$ are species mass fractions in the fuel and air streams respectively. The index i represents any species employed

in the chemical mechanism used to perform the DHR calculations. After the mixing of fuel and air, the fresh gases mixture is at a mixture fraction Z_0. Mixture fraction is considered as a fuel tracer and is here defined as the sum of the C and H atoms mass fractions in the mixture. If we call Z_F the mixture fraction in the fuel stream (equal to unity when the fuel stream contains only C and H atoms like in the calculations presented in Section 4.6), the fresh gases total enthalpy can be deduced from those of fuel and air according to their respective proportions:

$$H^u(Z_0) = (1 - Z_0^+)H_A({Y_i}^A, T_A) + Z_0^+ H_F({Y_i}^F, T_F) \tag{4.16}$$

where Z_0^+ is the normalized mixture fraction defined by:

$$Z_0^+ = \frac{Z_0}{Z_F} \tag{4.17}$$

The fresh gases species composition is defined by:

$${Y_i}^u(Z_0) = (1 - Z_0^+){Y_i}^A + Z_0^+ {Y_i}^F \tag{4.18}$$

The fresh gases total enthalpy $H^u(Z_0)$ and the fresh gases species composition ${Y_i}^u(Z_0)$ allow to deduce the fresh gases temperature $T_0(Z_0)$ which is only a function of Z_0.

With regard to diluent recirculated burnt gases in industrial furnaces, they usually correspond to well mixed fuel and air. Their mixture fraction Z_d (where the subscript d stays for *diluent*) can be consequently approximated by the mean mixture fraction of the furnace, which is defined as:

$$Z_d = \frac{\dot{m}_F}{\dot{m}_F + \dot{m}_A} \tag{4.19}$$

where $\dot{m}_F$ and $\dot{m}_A$ are the fuel and air mass flow rates respectively. As industrial furnaces are designed to exchange a large amount of heat and consequently are strongly under-adiabatic, the diluent total enthalpy is usually much smaller than that of the corresponding fresh mixture $H^u(Z_d)$ at mixture fraction Z_d. For this reason, an enthalpy loss ΔH_d is added to the initial mixture enthalpy $H^u(Z_d)$, yielding:

$$H_d(Z_d, \Delta H_d) = H^u(Z_d) + \Delta H_d \tag{4.20}$$

For $\Delta H_d = 0$, i.e. when diluent gases are adiabatic, $H_d(Z_d, \Delta H_d)$ is equal to the fresh gases enthalpy $H^u(Z_d)$. The enthalpy $H_d(Z_d, \Delta H_d)$ along with the unburnt composition ${Y_i}^u(Z_d)$, allow to calculate the equilibrium state, defined by the equilibrium temperature $T_d = T^{eq}(Z_d, H_d)$ and composition ${Y_i}^{eq}(Z_d, H_d)$. For convenience, the burnt gases under-adiabaticity will also be presented as a function of $\Delta T_d = T^{eq}(Z_d, H_d) - T^{eq}(Z_d, H_u(Z_d))$ which represents the burnt gases temperature decrease compared to the adiabatic burnt gases temperature. Once the two mixtures are defined, they are mixed together. For this purpose a dilution factor α is introduced which quantifies the mass fraction of burnt gases in the final mixture. It first allows to define the mixture fraction Z of the mixed state as:

$$Z = (1 - \alpha)Z_0 + \alpha Z_d \tag{4.21}$$

It should be noticed that as the diluent is made of burnt gases it is not an inert diluent but contributes to the equilibrium state. This is seen in the above equation through the diluent contribution αZ_d to mixture fraction.

The total enthalpy of the mixed state follows the same linear relation and reads:

$$\begin{aligned} H(Z_0, \alpha, \Delta H_d) &= (1 - \alpha)H^u(Z_0) + \alpha H_d(Z_d, \Delta H_d) && (4.22)\\ &= (1 - \alpha)H^u(Z_0) + \alpha(H_u(Z_d) + \Delta H_d) && (4.23) \end{aligned}$$

In the above equation $(1 - \alpha)H^u(Z_0) + \alpha H_u(Z_d)$ is equal to the adiabatic enthalpy of the mixture $H^u(Z)$, which allows to rearrange Eq. (4.23) as:

$$H(Z_0, \alpha, \Delta H_d) = H^u(Z) + \alpha \Delta H_d \tag{4.24}$$

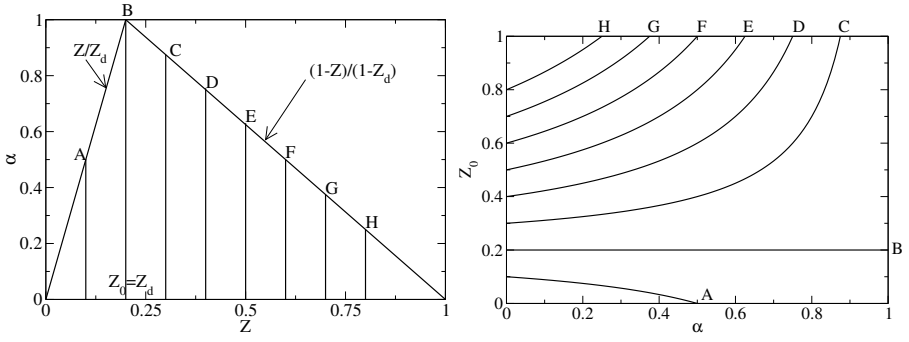

Figure 4.1 – *Values of α_{max} (capital letters from A to F) in the $[\alpha, Z]$ plane (left) and in the $[Z_0, \alpha]$ plane (right) for eight values of $Z \in [0.1 : 0.8]$ with $Z_d = 0.2$.*

This equation shows that the enthalpy loss of the mixed state $\Delta H = H - H^u(Z)$ is equal to $\alpha \Delta H_d$ and that it is proportional to the amount of diluent introduced and to the enthalpy loss of the diluent itself. Considering a thermodynamical state defined by Z and H, it is important to note that any α, Z_0 and ΔH_d satisfying Eq. (4.21) and Eq. (4.24) will lead to the same equilibrium state. This shows that the formulation is thermodynamically consistent.

Right after mixing, before auto-ignition starts, at $t = 0$, the mixture composition is defined as a function of α:

$$Y_i(t = 0) = (1 - \alpha) Y_i{}^u(Z_0) + \alpha Y_i{}^{eq}(Z_d, H_d) \tag{4.25}$$

It is interesting to note that if α is set to zero, the initial condition is exactly the one used in HR calculations used in the ADF-PCM model for instance [76]. This means that the DHR table contains the HR table.

The mixed state being described, it is interesting to note that Eq. (4.21) establishes a relation between Z, Z_0, and α for a fixed value of Z_d. As both Z_0 and Z range between 0 and 1, the possible values of α are restricted as follows:

$$\alpha_{max} = \frac{Z}{Z_d} \quad \text{for } Z \leq Z_d \tag{4.26}$$

$$\alpha_{max} = \frac{1 - Z}{1 - Z_d} \quad \text{for } Z > Z_d \tag{4.27}$$

These restrictions are shown graphically in the planes $[\alpha, Z]$ (Fig. 4.1(a)) and $[Z_0, \alpha]$ (Fig. 4.1(b)). In the first plane Eq. (4.21) is shown for eight values of Z ranging from 0.1 to 0.8 with a step of 0.1, and therefore corresponds to vertical lines. These vertical lines are limited on the upper side by the lines defined by Eq. (4.26) and (4.27), which represent the maximal value of α. The point of maximal dilution is denoted by a letter from A to H for the eight mixture fractions. The same iso-Z curves are traced in the $[Z_0, \alpha]$ plane (Fig. 4.1(b)). These curves start at $\alpha = 0$ and end at the maximum dilution corresponding to points A to H. It is here clear that the condition $Z_0 \in [0, 1]$ limits the maximum value of α as the curves stop at points where $Z_0 = 0$ or $Z_0 = 1$.

4.3.3 Tabulation of DHR trajectories

The DHR reactor calculations are performed considering a homogeneous adiabatic mixture which follows Eq. (4.2) and (4.3) without the convective and diffusive terms. Like in the FPI-PCM [64] model, the evolution of the mixture composition in the reactor is monitored by a progress variable Y_c which is defined as a linear combination of species mass fractions. As in [65], we choose the sum of the CO and CO_2 mass fractions: $Y_c = Y_{CO} + Y_{CO_2}$. This choice allows

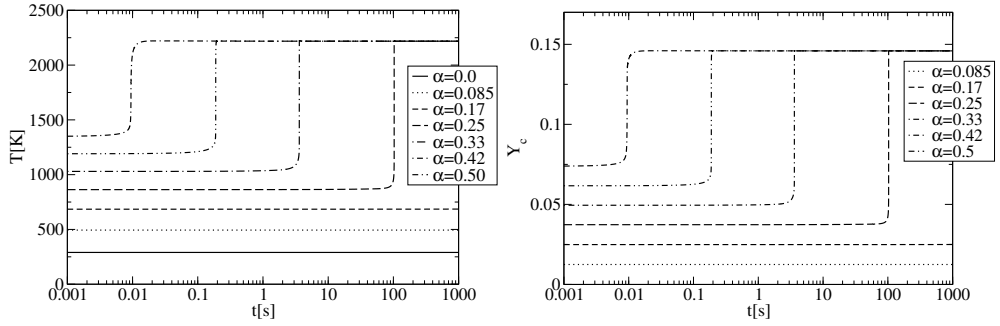

(a) (b)

Figure 4.2 – *Temporal evolution of T (left) and Y_c (right) for six values of the dilution factor α. Conditions: $T_0 = 290$ K, $Z = 0.055$ and $p = 1$ bar.*

a monotonic increase of Y_c from its initial value up to the equilibrium value $Y_c^{eq}(Z, H)$, which only depends on the considered mixture fraction Z and total enthalpy H. Such a monotonicity is illustrated in Fig. 4.2(b). As Y_c increases monotonically, it allows a bijective representation of the reactor characteristics (temperature, species etc...) against Y_c. This is illustrated in Figures 4.4 to 4.5 which show that a given value of Y_c on the X-axis corresponds to a unique value on the Y-axis. In order to build the DHR table, a normalized progress variable is introduced:

$$c = \frac{Y_c}{Y_c^{eq}(Z, H)} \tag{4.28}$$

It goes from zero in the fresh gases mixture, up to unity in the fully burnt gases at equilibrium. Noting that the diluent already contains CO and CO_2, the initial normalized progress variable $c(t = 0)$ will be larger than zero when $\alpha > 0$.

Fig. 4.2(a) and 4.2(b) present typical evolutions of temperature T and Y_c versus time for different initial dilutions in the case of an adiabatic diluent ($\Delta H_d = 0$). The fuel stream corresponds to methane at $T_F = 290$ K while the oxidizer stream is composed of air at $T_A = 290$ K. The reactor calculations are performed with the GRI−MECH 3.0 mechanism [82]. It can be first noticed that the initial temperature and Y_c increase with dilution. This can be explained looking at Eq. (4.25). As the fuel/air fresh mixture contains neither CO nor CO_2, Y_c is proportional to dilution α:

$$Y_c(t = 0) = \alpha Y_c^{eq}(Z_d, H_d) \tag{4.29}$$

As dilution increases, the mass fraction of burnt gases increases, which also leads to an increase of the initial temperature. Two types of trajectories can be observed in Fig. 4.2. For a dilution smaller than 0.25, the initial temperature is too low to promote auto-ignition; temperature and mass fractions therefore keep their initial values. For $\alpha \geq 0.25$, auto-ignition occurs after an ignition delay which decreases with increasing dilution, that is, with increasing initial temperature. This induction period is followed by a rapid increase of temperature and Y_c towards their equilibrium values.

This allows to define a critical dilution $\alpha_{reac}(Z, H)$ as the lowest dilution fraction leading to auto-ignition for a given mixture fraction Z and enthalpy H. It is worth noting that the reactive trajectories of Fig. 4.2(a) and 4.2(b) present the same $T^{eq}(Z, H)$ and final composition $Y_i^{eq}(Z, H)$, as they share the same enthalpy and mixture fraction. Besides, like for $\alpha_{reac}(Z, H)$, a critical progress variable ${Y_c}^{reac}$ can be defined as:

$${Y_c}^{reac}(Z, H) = \alpha_{reac}(Z, H) Y_c^{eq}(Z_d, H_d) \tag{4.30}$$

where the enthalpy H_d is deduced from Eq. (4.24) in order to preserve the total enthalpy H considered:

$$H_d = H^u(Z_d) + \frac{H - H^u(Z)}{\alpha} \tag{4.31}$$

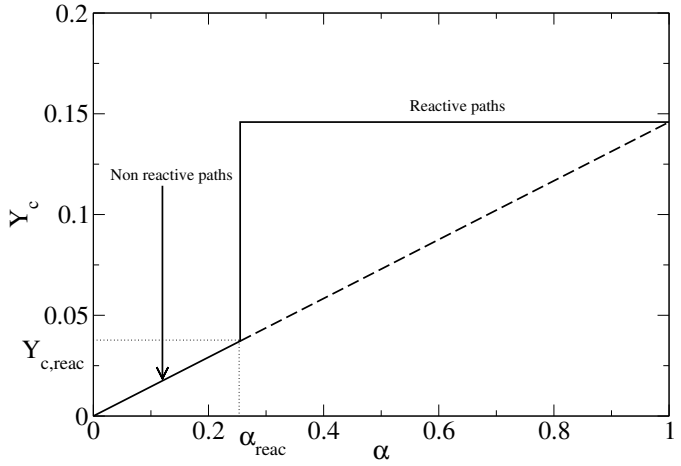

Figure 4.3 – *Schematic evolution of Y_c in DHR reactor calculations from its value at $t = 0$ to Y_c^{eq} as a function of the dilution factor α. Conditions: $T_0 = 290$ K, $Z = 0.055$ and $p = 1$ bar.*

With these definitions, Fig. 4.3 shows schematically the values Y_c can assume as a function of α, still considering an adiabatic diluent. For $\alpha < \alpha_{reac}$, Y_c assumes a unique value given by Eq. (4.29), as trajectories are not reactive. For $\alpha \geq \alpha_{reac}$, Y_c follows a vertical trajectory between its initial value and its equilibrium value $Y_c^{eq}(Z, H)$. In the general non adiabatic case, if we consider a given enthalpy $H(Z) < H^u(Z)$, the sketch remains identical excepted that the diluent enthalpy H_d evolves with α according to Eq. (4.31). As a consequence, $Y_c^{eq}(Z_d, H_d)$ also depends on α and the initial value of Y_c defined by Eq. (4.29) is no more a straight line.

Fig. 4.4 presents the bijective evolution of temperature, CO and CO_2 mass fractions versus Y_c for three different dilutions. For $Y_c < 0.136$ approximately (corresponding to $c \sim 0.93$ for the equilibrium value $Y_c^{eq} = 0.1459$), the dependence of temperature with dilution is weak, while that of CO and CO_2 is more pronounced. For $Y_c > 0.136$, that is close to the equilibrium state, all trajectories tend to collapse towards a unique trajectory. This type of observation was already made for premixed laminar flames by Gicquel et al. [64]: the species manifold becomes mono-dimensional only close to the equilibrium state, while it remains multi-dimensional at lower temperatures. For each reactive trajectory, the reaction rate of the progress variable can be defined as:

$$\dot{\omega}_{Y_c}(Z_0, \alpha, \Delta H, t) = \frac{\partial Y_c}{\partial t}(Z_0, \alpha, \Delta H_d, t) \tag{4.32}$$

$\dot{\omega}_{Y_c}$ is presented in Fig. 4.6 as a function of Y_c for the same cases. It can be observed that, as the level of dilution increases, the peak of reactivity shifts towards larger values of Y_c. On the contrary, the level of dilution does not affect the order of magnitude of the maximal reaction rate as well as the shape of the $\dot{\omega}_{Y_c}$ curve. This observation is due to the fact that as the total enthalpy H is kept constant, the mixture temperature is weakly sensitive to the dilution ratio α.

The situation is different if we now consider a variation $\alpha\Delta H_d$ of the total enthalpy H. For this purpose, α is kept constant at 0.33 while three values of ΔH_d are chosen: $\Delta H_d = 0$, $\Delta H_d = -167$ kJ/kg (dashed line) and $\Delta H_d = -315$ kJ/kg (dashed-dot). The first one corresponds to adiabatic burnt gases at $T^{eq} = 2220$ K, while the others correspond to diluent temperature variation $\Delta T_d = -350$ K and -650 K respectively. Fig. 4.5 presents $\dot{\omega}_{Y_c}$, temperature, CO and CO_2 for these conditions. It can be observed that the maximum reaction rate drops dramatically as ΔH_d decreases. The temperature trajectories of the non adiabatic cases look similar to the adiabatic one, excepted that they are shifted by a nearly constant shift corresponding to $\Delta H = \alpha\Delta H_d$ (see Eq. (4.24)). Species CO and CO_2 are also affected by the non-adiabaticity for $Y_c < 0.125$. Above this value, trajectories become similar with contained variations of Y_c^{eq} depending

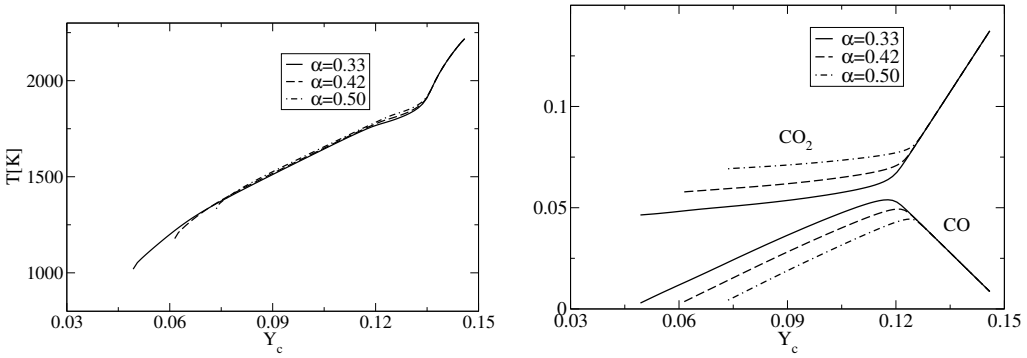

Figure 4.4 – *Evolution of T (left), CO and CO_2 (right) versus Y_c for three values of dilution α. Conditions: $T_0 = 290$ K, $Z = 0.055$ and $p = 1$ bar.*

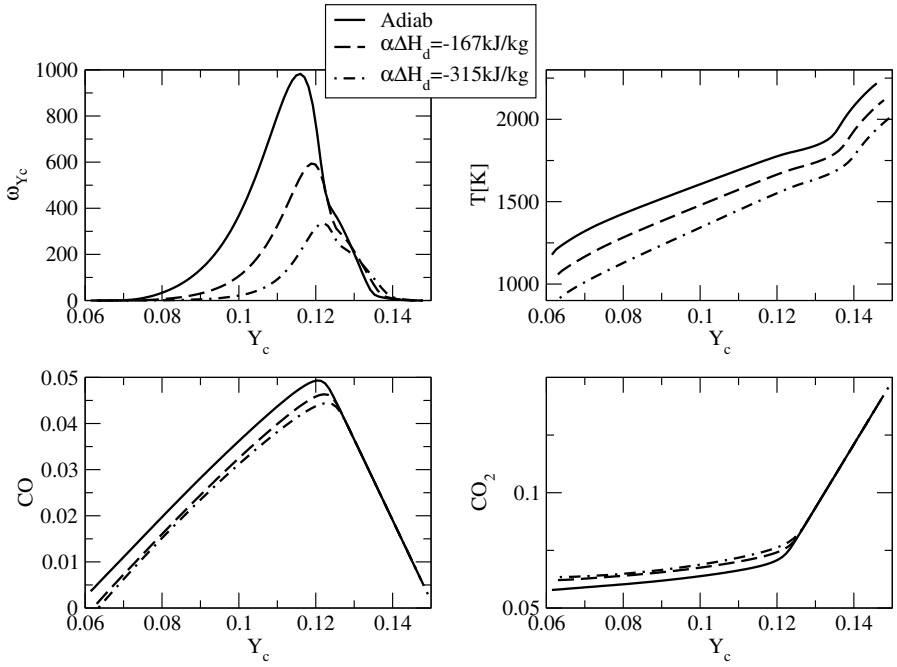

Figure 4.5 – *Clockwise: Progress variable reaction rate $\dot{\omega}_{Y_c}$, temperature T, CO_2 and CO versus Y_c for three values of the enthalpy gap $\alpha\Delta H_d$. Conditions: $T_0 = 290$ K, $Z = 0.055$ and $p = 1$ bar.*

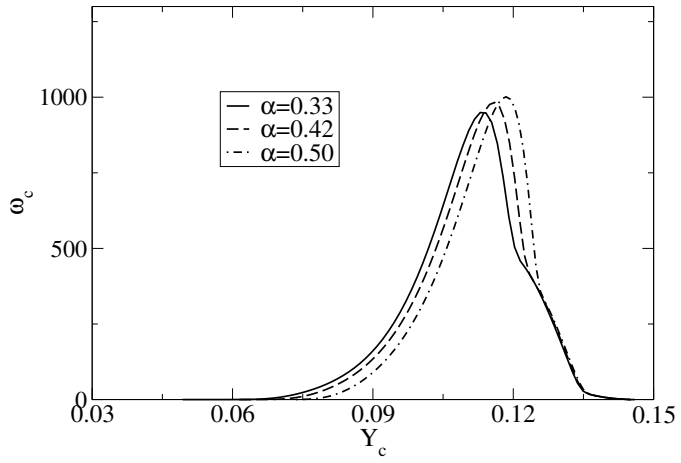

Figure 4.6 – *Progress variable reaction rate $\dot{\omega}_{Y_c}$ versus Y_c. Conditions: $T_0 = 290$ K, $Z = 0.055$ and $p = 1$ bar.*

on ΔT_d. Based on the previous description of DHR calculations, the homogeneous DHR table is built as a function of six input parameters:

$$\Phi^{DHR} = \Phi^{DHR}(Z_0, \alpha, T_0, p, \Delta H, Y_c = cY_c{}^{eq}) \tag{4.33}$$

where $\Delta H = \alpha \Delta H_d$ represents the enthalpy loss of the mixed state. The outputs Φ^{DHR} of the table that will be used in the final model are:

- the reaction rate $\dot{\omega}_{Y_c}^{DHR}$;
- Five tabulated species Y_k^{DHR}: CH_4, CO_2, H_2O, H and CO.

In the calculations presented in this article, pressure is nearly constant and T_0 can be deduced from fuel and air inlet conditions (see Eq. (4.16) and (4.18)). To simplify notations, the parameter p in Eq (4.33) will be omitted in the following Sections.

4.3.4 Filtering of the DHR table

In the previous Section, a homogeneous DHR table was obtained. In order to apply DHR to LES, a filtering of this homogeneous table is required. For this purpose, presumed PDF of the input parameters are used following the procedure proposed in the PCM model [71]. Any filtered output of the DHR table can be written in the most general form:

$$\widetilde{\Phi}^{DHR} = \int_0^1 \int_0^1 \Phi^{DHR}(Z_0, \alpha, T_0, \Delta H, Y_c = cY_c{}^{eq}) P((Z_0, \alpha, \Delta H, c)|Z) P(Z)\, dZ_0 d\alpha d\Delta H dc dZ \tag{4.34}$$

where $P(Z)$ is the PDF of mixture fraction and $P((Z_0, \alpha, \Delta H, c)|Z)$ is the PDF of all other parameters conditioned on Z. As this conditional PDF is unknown, modeling assumptions are necessary. We first assume that dilution of the fresh mixture with burnt gases takes place at a large time and length scale in the combustion chamber. This hypothesis allows to consider that for a given mixture fraction Z, the SGS fluctuations of Z_0 and α can be neglected. This is also equivalent to say that the fresh mixture is perfectly mixed with the diluent gases at the SGS level. A second assumption is to consider that the diluent gases enthalpy is locally uniform at the SGS level. This assumption is justified like the previous one by the fact that enthalpy variations in the combustion chamber take place at large time and length scales.

Combining both hypothesis allows to consider that for a given Z, the fluctuations of enthalpy can also be neglected. This allows to define a unique value ΔH for a given Z as presented in Section 4.3.5. The first hypothesis allows to define a unique couple (Z_0, α) as a function of the three remaining parameters Z, H and Y_c as presented in Section 4.3.6. With these assumptions, Eq. (4.34) can be simplified as:

$$\widetilde{\Phi}^{DHR} = \int_0^1 \int_0^1 \Phi^{DHR}(Z_0, \alpha, T_0, \Delta H, Y_c = cY_c{}^{eq}) P(c|Z) P(Z) dc dZ \tag{4.35}$$

In order to model the conditional PDF $P(c|Z)$ first (PCM1) and second order (PCM2) formulations were proposed in [71]. In both formulations, it is first assumed that fluctuations of c are weakly dependent on mixture fraction, which allows to further simplify Eq. (4.35) writing $P(c|Z) \simeq P(c)$. For PCM1, $P(c)$ is assumed to be a Dirac delta function at $c = \tilde{c}$, while for PCM2, $P(c)$ is modeled as a β function completely characterized by the values of $\tilde{c}$ and the progress variable variance v_c for which a transport equation is added. Very recently, Chevillard et al.[95] conducted DNS of auto-igniting two-feed mixing layers comparable to those observed in Diesel engines. The PCM1, PCM2 and ADF-PCM approximations of $P(c, Z)$ were evaluated *a priori* against the DNS reference solution. It was shown that assuming a β-PDF for c (PCM2) can be sometimes worse than assuming a Dirac function (PCM1). The best solution was obtained using the PDF deduced from an auto-ignition laminar diffusion flame like done in the ADF-PCM combustion model. This result shows that in the present case of a three-feed mixing, the best modeling might be given by a two-dimensional flamelet equation like proposed by Doran et al.[96]. Although interesting, this choice would lead to a high complexification of the present model, which is not desired. Alternatively, as evidenced in the two-feed case, choosing a Dirac function is probably not worse than using a β-pdf in the three-feed case. For this reason, the PCM1 formulation is finally retained, leading to the following expression of the filtered variable:

$$\widetilde{\Phi}^{DHR} = \int_0^1 \Phi^{DHR}(Z_0, \alpha, T_0, \Delta H, Y_c = \tilde{c} Y_c^{eq}(Z, H(Z))) P(Z) dZ \tag{4.36}$$

Eq. (4.36) allows to calculate the mean progress variable reaction rate $\widetilde{\dot{\omega}}_{Y_c}^{DHR}$ and the mean tabulated species mass fractions $\tilde{Y}_k^{DHR}$. As presented in Section 4.3.7 these quantities will finally allow to define the species and energy source terms.

In order to compute the integral in Eq. (4.36), $P(Z)$ is approximated using a $\beta - PDF$ function:

$$P(Z) = P_\beta(Z, \tilde{Z}, S_z) \tag{4.37}$$

where S_z is the normalized variance of Z, called the segregation factor, and is defined as:

$$S_z = \frac{v_Z}{\tilde{Z}(1 - \tilde{Z})} \tag{4.38}$$

The four input parameters of the DHR table appearing in the integral of Eq. (4.36) can not be obtained directly from the transported quantities presented in Section 4.3.1. In fact, once $H(Z)$ is known, ΔH can be directly deduced from Eq. (4.24): $\Delta H(Z) = H(Z) - H_u(Z)$, where the enthalpy $H_u(Z)$ is given by fuel and air inlet conditions. Section 4.3.5 presents the determination of $H(Z)$ and $\tilde{c}$, while Section 4.3.6 presents the determination of Z_0 and α.

4.3.5 Determination of the local enthalpy loss ΔH and mean progress variable

In Eq. (4.36), the enthalpy $H(Z)$ at mixture fraction Z needs to be specified, both to determine the input parameter ΔH and to calculate the equilibrium progress variable $Y_c{}^{eq}(Z, H(Z))$. In the LES calculation, only the mean total enthalpy is available:

$$\tilde{H} = \tilde{h}_s + \sum_k \tilde{Y}_k h_k^0 \tag{4.39}$$

where $\tilde{h}_s$ is deduced from the transported energy $\tilde{E}$. Consequently, modeling assumptions need to be introduced to calculate ΔH. Eq. (4.24) shows that the total enthalpy $H(Z_0, \alpha, \Delta H_d)$ can be varied through the term $\alpha\Delta H_d$. The maximal value of H corresponds to the adiabatic case ($\Delta H_d = 0$) while the minimal value is attained for the largest enthalpy loss in the diluent gases ($\Delta H_d = {\Delta H_d}^{min}$) and for the maximal value of dilution α_{max} defined by Eq. (4.26) and (4.27):

$$H_{max}(Z) = H^u(Z) \tag{4.40}$$

$$H_{min}(Z) = H^u(Z) + \alpha_{max}{\Delta H_d}^{min} \tag{4.41}$$

These minimal and maximal values need to be chosen in adequation with the configuration simulated. This means that ${\Delta H_d}^{min}$ needs to be sufficiently low to guarantee that any enthalpy level found in the LES is be included in the DHR table. In order to evaluate H under non-adiabatic conditions, the approach proposed in [97] for the FPI-PCM model is used here. It expresses the local enthalpy H as:

$$H(Z) = H_{min}(Z) + c_H(H_{max}(Z) - H_{min}(Z)) \tag{4.42}$$

where c_H represents a normalized measure of the non-adiabaticity: $c_H = 1$ for an adiabatic mixture while $c_H = 0$ for the minimal enthalpy value. In order to determine c_H, we further assume that it does not depend on Z: $c_H(Z) = \tilde{c}_H$. This allows to write:

$$H(Z) = H_{min}(Z) + \tilde{c}_H(H_{max}(Z) - H_{min}(Z)) \tag{4.43}$$

$\tilde{c}_H$ is then obtained by filtering Eq. (4.43) over mixture fraction:

$$\tilde{c}_H = \frac{\tilde{H} - \tilde{H}_{min}(\tilde{Z}, S_z)}{\tilde{H}_{max}(\tilde{Z}, S_z) - \tilde{H}_{min}(\tilde{Z}, S_z)} \tag{4.44}$$

where $\tilde{H}_{max}$ and $\tilde{H}_{min}$ correspond to the filtering of Eq. (4.40) and (4.41):

$$\tilde{H}_{max}(\tilde{Z}, S_z) = \int_0^1 H_{max}(Z)P(Z)dZ \tag{4.45}$$

$$\tilde{H}_{min}(\tilde{Z}, S_z) = \int_0^1 H_{min}(Z)P(Z)dZ \tag{4.46}$$

Knowing $H(Z)$, it is possible to evaluate the mean equilibrium progress variable:

$$\tilde{Y}_c^{eq}(\tilde{Z}, S_z, \tilde{c}_H) = \int_0^1 Y_c^{eq}(Z, H(Z))P(Z)dZ \tag{4.47}$$

which finally allows to define the mean progress variable $\tilde{c}$ as:

$$\tilde{c} = \frac{\tilde{Y}_c}{\tilde{Y}_c^{eq}} \tag{4.48}$$

where $\tilde{Y}_c(x,t)$ is retrieved from the sum of the transported values of $\tilde{Y}_{CO}$ and $\tilde{Y}_{CO_2}$.

4.3.6 Determination of the dilution factor α

Like for ΔH, α and Z_0 in Eq. (4.36) can not be directly retrieved from filtered quantities. In fact, as shown in Section 4.3.3, a given value of Z can correspond to an infinity of Z_0 and α couples, linked by Eq. (4.21).

In order to define α, we use the observation that auto-ignition only occurs if $\alpha \geq \alpha_{reac}$, which can also be formulated in terms of progress variable as $Y_c \geq {Y_c}^{reac}$. In Eq. (4.36), Y_c is known from the relation $Y_c = \tilde{c}Y_c^{eq}(Z, H(Z))$ and is here used as an input parameter to individuate a unequivocal value of α, depending on the reactivity of the mixture:

1. If $Y_c < {Y_c}^{reac}$, the trajectory can not be reactive (see Fig. 4.3). In this situation, α is directly deduced form Y_c using Eq. (4.29). The progress variable reaction rate is zero and the mass fractions correspond to the mixing between fresh and burnt gases as described in Section 4.3.2;
2. If $Y_c \geq Y_c^{reac}$, the trajectory is necessarily reactive. In this case all values of α satisfying $\alpha \geq \alpha_{reac}$ and $\alpha \leq \frac{Y_c}{Y_c^{eq}(Z_d,H_d)}$ (Eq. (4.25)) could be considered as input parameters. Following the analysis of Fig. 4.6, it is assumed as a first modeling that reactive trajectories are weakly dependent on the value of α, as long as the total enthalpy of the mixture $H(Z)$ is kept constant. This allows to choose $\alpha = \alpha_{reac}$. In future work, a more refined modeling could be envisaged by considering for instance a transport equation for the mean dilution fraction.

The above two cases can be summarized in the following mathematical expression of α, valid for all cases:

$$\alpha(Z,H) = \min\left(\alpha_{reac}(Z,H), \frac{Y_c}{Y_c^{eq}(Z_d,H_d)}\right) \tag{4.49}$$

It is important to note that in the above expression, α evolves with Y_c only when the trajectory is not reactive, that is when $Y_c < \alpha_{reac} Y_c^{eq}$. When the trajectory becomes reactive, α does not depend anymore on the progress of reaction Y_c and remains equal to α_{reac}. This means that for fixed mixture fraction and enthalpy conditions, a unique DHR reactive trajectory is followed.

Another important remark concerns the case of non diluted mixtures. If the initial mixture is not diluted by burnt gases, that is $Y_c = 0$ initially, Eq. (4.49) shows that initially a HR (non diluted) trajectory will be used by the DHR model. If the initial temperature is too low, this trajectory will be non reactive and no auto-ignition will take place. On the contrary, if the initial temperature is high enough, like in a Diesel engine, α_{reac} will also be equal to zero. As a consequence, the DHR model will follow the reactive HR trajectory characterized by $\alpha = 0$, exactly like in TKI or ADF-PCM models. This shows that in the absence of dilution, the DHR model reverts to the standard HR tabulated model.

To summarize, the species and progress variable reaction rate are given by the following expressions:

$$\tilde{Y}_k^{DHR}(\tilde{Z}, S_z, \tilde{Y}_c, \tilde{c}_H) = \int_0^1 Y_k^{DHR}(Z_0, \alpha, T_0, \Delta H, \tilde{c} Y_c^{eq}(Z, H(Z)) P(Z) dZ \tag{4.50}$$

$$\tilde{\omega}_{Y_c}^{DHR}(\tilde{Z}, S_z, \tilde{Y}_c, \tilde{c}_H) = \int_0^1 \omega_{Y_c}^{DHR}(Z_0, \alpha, T_0, \Delta H, \tilde{c} Y_c^{eq}(Z, H(Z)) P(Z) dZ \tag{4.51}$$

In the above expressions, $P(Z)$ is a beta-PDF defined by $\tilde{Z}$ and S_z which are given by the transport equations of the mean and variance of mixture fraction Eq. (4.4) and Eq. (4.5). The normalized enthalpy loss $\tilde{c}_H$ is given by Eq. (4.44) which itself depends on the mean total enthalpy $\tilde{H}$ which is deduced from the transport equations of species and energy $\tilde{E}$, Eq. (4.2) and (4.3). Knowing $\tilde{c}_H$, the conditional enthalpy $H(Z)$ can be calculated using Eq. (4.43) and the enthalpy loss ΔH using Eq. (4.24). This allows in turn to deduce the conditional equilibrium progress variable $Y_c^{eq}(Z, H(Z))$ and its filtered value $\tilde{Y}_c^{eq}$, Eq. (4.47). The filtered non-normalized progress variable $\tilde{Y}_c$ is given by the transport equations of CO and CO_2 Eq. (4.3). The filtered normalized progress variable $\tilde{c}$ is deduced from $\tilde{Y}_c^{eq}$ and $\tilde{Y}_c$ using Eq. (4.48). The dilution factor α is finally given by Eq. (4.49), while Z_0 is given by Eq. (4.21).

4.3.7 Species reaction rates calculation

In the present paper, the DHR model is implemented in the compressible LES code AVBP [98]. In this code, filtered species mass fractions are transported (Eq. (4.3)), therefore, their respective chemical source terms $\widetilde{\dot{\omega}_k}$ need to be defined. As shown in Michel et al. [99], when

using species transport equations, it is not possible to directly extract $\widetilde{\omega_k}$ from the filtered table because this leads to trajectory inconsistencies. For this reason, the relaxation approach proposed in this paper is used for determining the species reaction rates:

$$\widetilde{\omega_k}(x,t) = \frac{\tilde{Y}_k^{DHR}(\tilde{Z}, S_z, \tilde{Y}_c^*, \tilde{c}_H) - \tilde{Y}_k(x,t)}{\tau} \tag{4.52}$$

In this expression $\tilde{Y}_k^{DHR}$ is given by Eq. (4.50) and τ is an arbitrary small relaxation parameter which only needs to satisfy $\tau \geq dt$, where dt is the time step of the code. It was shown in [99] that as long as τ remains small compared to the reaction rate time-scale, transported mass fractions remain very close to the table values. As proposed in [99], $\tau = 5dt$ is used in the present calculations to guaranty this property. $\tilde{Y}_c^*$ is the progress variable at time $t + \tau$ defined as:

$$\tilde{Y}_c^* = \tilde{Y}_c + \tau \tilde{\omega}_{Y_c}^{DHR}(\tilde{Z}, S_z, \tilde{Y}_c, \tilde{c}_H) \tag{4.53}$$

where $\tilde{\omega}_{Y_c}^{DHR}$ is given by Eq. (4.51). Nine species are transported in the code. CH_4, CO, CO_2, H_2O and H are directly retrieved from the filtered DHR table using Eq. (4.36). The four remaining species O_2, N_2, CH_2 and H_2 are used to close the atomic balance of O, N, C and H atoms respectively. As reported in Section 4.3.1, the energy source term is finally deduced from the species source terms using Eq. (4.15).

4.4 First evaluation on laminar diffusion flames

As a first evaluation, the DHR model is applied to the simulation of unsteady laminar counterflow diffusion flames. For this purpose, the DHR model is directly used to compute the progress variable reaction rate in the flamelet equation and to estimate the species mass fractions, leading to the computation of approximated diffusion flames (ADF) [76], which are compared to laminar diffusion flames computed with complex chemistry with a dedicated solver (here COSILAB [100]), in terms of ignition and flame structure. The main difference with the work presented in [76] is that we consider here much colder mixtures which are unable to auto-ignite without an energy deposit.

4.4.1 Reference calculations

We consider here kerosene/air unsteady counterflow laminar diffusion flames as reference flames. They are calculated using the COSILAB software [100]. The fuel stream is composed of pure kerosene at $T_0 = 300$ K and the oxidizer stream is composed of pure air at the same temperature. The pressure is constant and set equal to $p = 1$ bar. Two strain rate values have been tested, 1 and 10 s^{-1}. As a mixture of kerosene and air at atmospheric pressure at 300 K is not reactive due to the very low temperature, an energy deposit is necessary to let the air-fuel mixture auto-ignite. For the calculations of this section, three different initial temperature profiles are tested to allow ignition. These profiles present the same maximum of 1500K which is favorable to a fast auto-ignition of the mixture. They differ only in the location of the temperature profile: going from A to C, scalar dissipation increases (it is maximum at $Z = 0.5$), which leads to a faster diffusion of this initial profile and consequently to a reduced reactivity as time passes. These profiles are represented as functions of the mixture fraction in Fig. 4.7. These flames are solved in mixture fraction space using one flamelet equation [101] for each chemical species and one for the energy. Chemistry is represented by the mechanism of Luche et al. [102] which includes 91 species and 991 equations. All Lewis numbers are set equal to unity. Finally, these flames are solved with 200 points in mixture fraction space with a time step equal to $dt = 1. \times 10^{-7}$ s.

Approximated diffusion flames using tabulated chemistry

In order to reproduce the reference flames presented in Section 4.4.1 with the DHR model, we use the ADF-PCM flamelet equation presented in [73] and [76]. For this purpose, two flamelet equations have to be solved (instead of one in the original ADF-PCM approach). The first one corresponds to the progress variable mass fraction equation as proposed in ADF-PCM:

$$\frac{\partial Y_c}{\partial t} = \dot{\omega}_{Y_c} + \chi \frac{\partial^2 Y_c}{\partial Z^2} \tag{4.54}$$

in this equation, χ is the scalar dissipation rate, which is computed from the local value of Z and the strain rate a using the classical expression of Peters [101] below:

$$\chi(Z) = aF(Z) \tag{4.55}$$

$$F(Z) = \frac{\exp\left(-2[\mathrm{erf}^{-1}(1-2Z)]^2\right)}{2\pi} \tag{4.56}$$

$\dot{\omega}_{Y_c}$ is the progress variable reaction rate, read from the DHR database:

$$\dot{\omega}_{Y_c}(Z,t) = \dot{\omega}_{Y_c}^{DHR}(Z_0, \alpha, T_0, \Delta H, Y_c) \tag{4.57}$$

In the present flamelet calculations, no sink of enthalpy (radiation etc....) is introduced, consequently the enthalpy gap is $\Delta H = 0$. The diluent mixture fraction Z_d is here chosen equal to the stoichiometric mixture fraction Z_{st}. This choice comes from the fact that in a laminar diffusion flame, most of the burnt gases production (i.e. of the reaction rate) is located close to Z_{st}. The dilution factor α is calculated according to Eq. (4.49). In DHR as well as in ADF-PCM, the fresh gases total enthalpy H^u is deduced linearly from those of fuel and air, see Eq. (4.16). In the present simulations, we impose and initial profile $T_0(Z, t=0)$ corresponding to an enthalpy $H^u(Z, t=0)$ which is not linear with Z. This profile will consequently evolve in time due to diffusion in mixture fraction. The introduction of the fresh gases total enthalpy flamelet equation allows to follow this evolution:

$$\frac{\partial H^u}{\partial t} = \chi \frac{\partial^2 H^u}{\partial Z^2} \tag{4.58}$$

We note that this equation contains no source term because total enthalpy and adiabatic flow conditions are considered. We also observe that as $\Delta H = 0$, $H(Z,t) = H^u(Z,t)$ (see Eq. 4.24). Knowing $H^u(Z,t)$ and the fresh gases composition Eq. (4.18) allows to deduce the instantaneous fresh gases temperature $T_0(Z,t)$ used to define the progress variable reaction rate Eq. (4.57).

Following the ADF-PCM approach, all species mass fractions are then read from the DHR look-up table in the same manner as the progress variable reaction rate:

$$Y_k(Z,t) = Y_k^{DHR}(Z_0, \alpha, T_0, \Delta H, Y_c) \tag{4.59}$$

which allows a very fast computation in comparison with the complex chemistry reference calculation (only a few seconds). Temperature is retrieved from the DHR table in the same way:

$$T(Z,t) = T^{DHR}(Z_0, \alpha, T_0, \Delta H, Y_c) \tag{4.60}$$

In the first place, if we assume $T_0(Z, t=0) = 300$ K we verify that the flame does not ignite. Therefore the initial profiles A,B and C presented in Fig. 4.7 are considered.

In order to perform these calculations, the DHR table is generated using the same chemical mechanism as in the reference flames calculations. As calculations are adiabatic, only the value $\Delta H = 0$ is considered. The resulting look-up table is described in Tab. 4.1. As for the reference flames, these approximated diffusion flames are solved with 200 points in mixture fraction space with a time step equal to $dt = 1. \times 10^{-7}$ s.

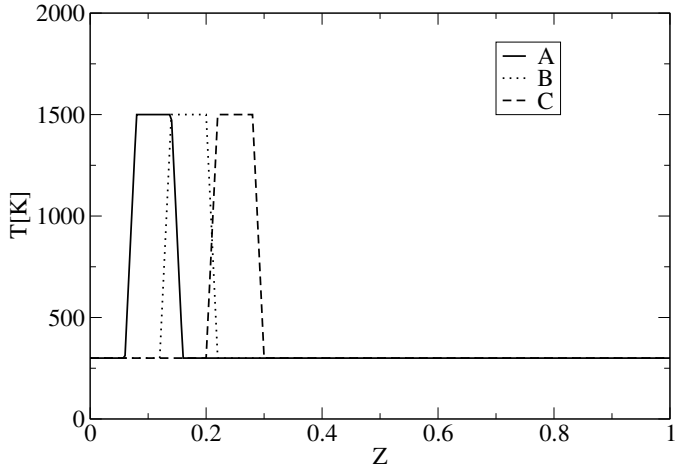

Figure 4.7 – *Initial fresh gases temperature profiles $T_0(Z, t = 0)$ for cases A, B and C versus mixture fraction.*

Unsteady results

As a first example, we consider a diffusion flame with a strain rate value equal to $a = 1\ \mathrm{s}^{-1}$. The initial temperature profile corresponds to case A presented in Fig. 4.7. Fig. 4.8 presents the evolution of temperature T and fresh gases temperature T_0 at six consecutive times: 0, 0.25, 0.5, 1, 6 and 9 ms for the reference and ADF flames.

Table 4.1 – *Description of the DHR look-up table used for the diffusion flame calculations*

Quantity	Number of tabulated values	Minimal value	Maximal value
T_0[K]	11	250	1800
Z_0	100	0	1
α	21	0	1
ΔH_d[J/kg]	1	0	0
Y_c	200	$Y_c(t = 0)$ (Eq. (4.25)	$Y_c{}^{eq}(Z, H(Z))$

At time $t = 0$, all temperature profiles are identical as $H = H^u$ and $Y_k = Y_k^u$. At $t = 0.25$ ms, chemical reactions have started at mixture fractions close to 0.08 and consequently T becomes larger than T_0 in this region. By contrast, T becomes smaller than T_0 in the rich region located at Z close to 0.12 due to the cracking of fuel, which is an endothermic reaction. At this time, the approximate diffusion flame perfectly matches the reference flame. At $t = 0.5$ ms, combustion has started between $Z \approx 0.6$ and $Z \approx 0.12$ for the reference flame and $Z \approx 0.7$ and $Z \approx 0.11$ for the approximate diffusion flame. At this stage, ignition has only occurred in regions where enthalpy (or fresh gases temperature) is sufficiently high to allow ignition of the mixture without dilution. Between 1 and 9 ms, the reactive zone propagates towards lean and rich mixtures for the reference and approximated diffusion flames. The agreement in temperature between the reference and approximate diffusion flame is very good in regions that are already ignited. In the auto-ignition front located on the lean and rich regions (corresponding to $Z \approx 0.05$ and $Z \approx 0.15$ at $t = 6$ ms), temperature is under-predicted by the approximated diffusion flame due to a slightly too slow propagation of auto-ignition. In these auto-igniting regions, the fresh gases temperature is very low (close to 300 K), unlike at earlier times. Consequently, ignition cannot occur without dilution. This is confirmed in Fig. 4.9 which presents the profiles

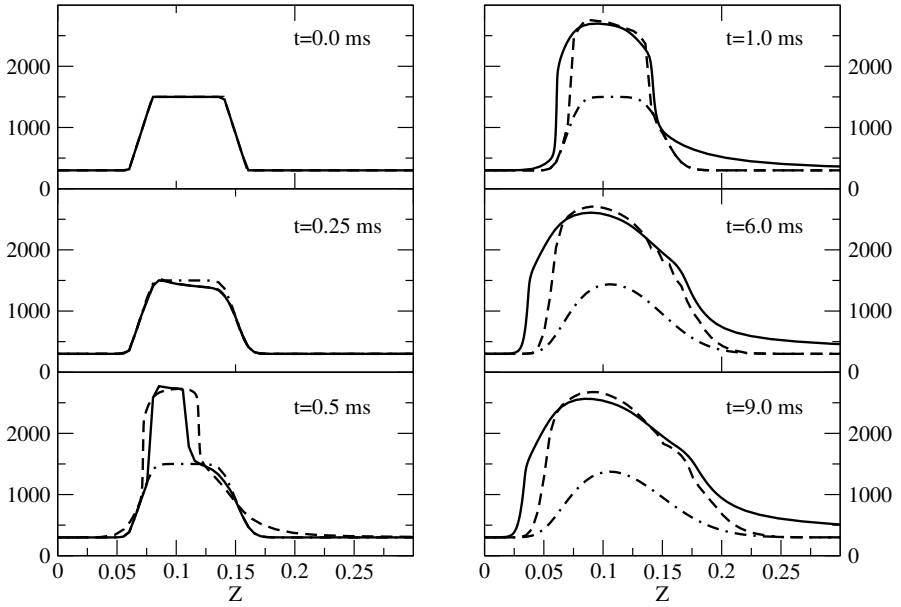

Figure 4.8 – *Evolution of temperature versus Z at six consecutive times (from* 0.0 *to* 9.0 *ms). Solid lines: approximated DHR temperature; Dashed lines: reference flame from COSILAB calculations; Dashed-dot: fresh gases temperature* T_0

of Y_c (for the reference and approximated diffusion flames) and α versus mixture fraction for $1 \leq t \leq 9$ ms. It can be observed that the profiles of Y_c predicted by the approximate diffusion flame completely reflect the agreement obtained for temperature in Fig. 4.8. The dilution factor reaches high values at the border of the reactive zone (at $Z \approx 0.05$ and $Z \approx 0.15$ at $t = 6$ ms). This is explained by the fact that in these regions the enthalpy decreases rapidly, leading to an increase of α_{reac} from zero to values as high as 0.8. Finally, Fig. 4.10 presents the profiles of Y_{CO} and Y_{CO_2} at the same times. As observed for temperature and Y_c, the agreement for both species is good in the ignited region and less satisfactory in the auto-igniting regions because of the too slow auto-ignition propagation speed. Globally, this comparison shows that the DHR model allows to retrieve correctly the main features of an auto-igniting diffusion flame.

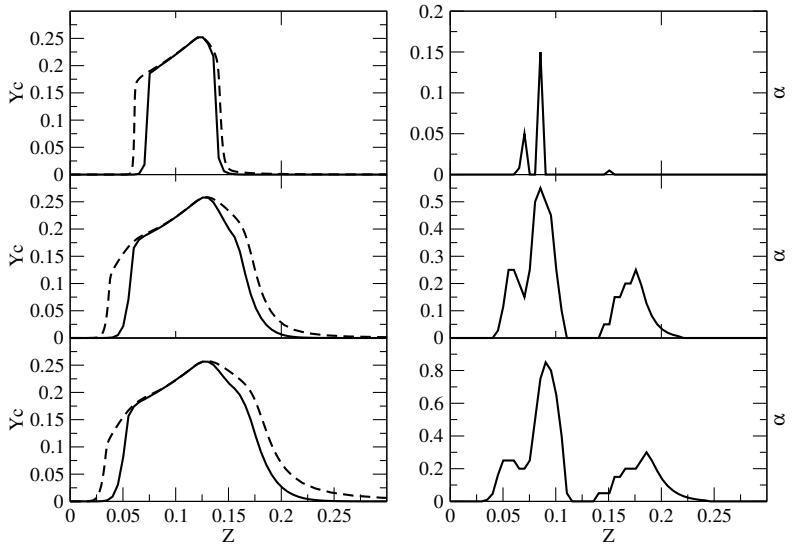

Figure 4.9 – *Profiles of* Y_c *(left) and* α *(right) versus Z at three consecutive times (from top to bottom* 1, 6 *and* 9 *ms). Solid line: approximate diffusion flame. Dashed line: reference flame.*

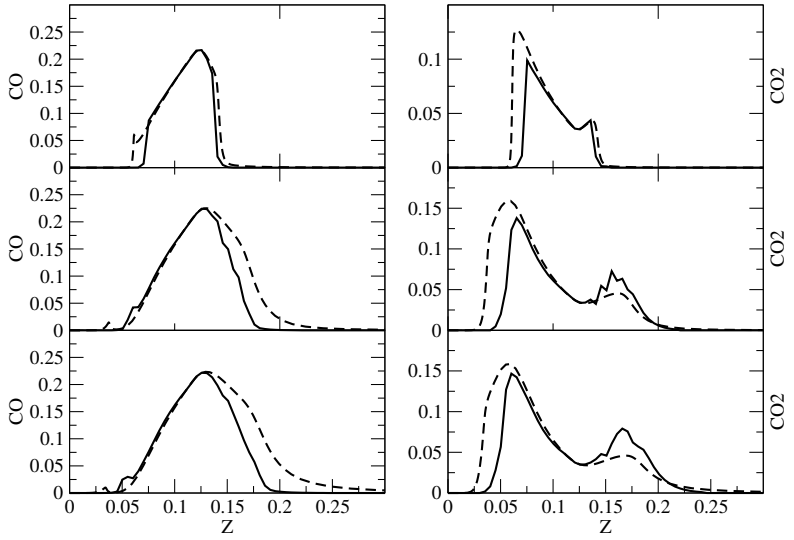

Figure 4.10 – *Profiles of Y_{CO} (left) and Y_{CO_2} (right) versus Z at three consecutive times (from top to bottom* 1, 6 *and* 9 *ms). Solid line: approximate diffusion flame. Dashed line: reference flame.*

Effects of strain rate and initial temperature profile on ignition

In this section, the influence of the strain rate and initial temperature profile on the flame ignition are studied. Table 4.2 summarizes the ignition success or failure obtained for the three temperature profiles A, B and C presented in Fig. 4.7 considering two strain rates: 1 and 10 s^{-1}. For all cases, the approximated diffusion flame calculation recovers the result of the reference diffusion flame. Namely, for $a = 1\ s^{-1}$, profiles A and B allow auto-ignition while C leads to an ignition failure. This behavior is explained by the fact that profiles A to C are centred on increasing mixture fraction values, therefore experiencing a higher scalar dissipation rate (the scalar dissipation rate χ in Eqs. (4.54) and (4.58) being proportional to $\exp(-\text{erf}^{-1}(Z-0.5))$. As scalar dissipation increases, the temperature diffusion time-scale decreases, and the initial temperature profile is diffused more rapidly. For the fastest diffusion case C, the diffusion time-scale becomes smaller than the auto-ignition delay time, therefore preventing auto-ignition.

In the same way, an increase of the strain rate from 1 to 10 s^{-1} leads to a reduction of the diffusion time-scale by a factor of 10. This reduction is strong enough to prevent auto-ignition for the three considered profiles A to C, showing that for the present thermo-chemical conditions, ignition is extremely sensitive to strain rate.

Steady state results

Finally, the steady state of the reference and approximate flames can be compared. For this purpose, reference flames have been computed with COSILAB for the same boundary conditions as previously, but considering the following four strain rate values: 1, 10, 100 and 1000 s^{-1}. The fact that a burning steady state exists for $a > 1\ s^{-1}$ although ignitions in these conditions cannot occur (see table 4.2), is explained by the difference between the ignition limit (i.e. the maximal value of strain rate - or scalar dissipation rate - allowing the ignition of the flamelet) and the quenching value (i.e. the value of strain rate above which the flame quenches) [101, 18]. The quenching limit is normally much larger than the ignition limit (which is here 0 without an energy deposit). In order to reach steady state, approximate steady state flamelet profiles for species and temperature are imposed at time t=0 for the reference flames. The same procedure is used for the approximate diffusion flames imposing the initial profile of Y_c. With such initializations, the flamelets converge rapidly towards their steady state.

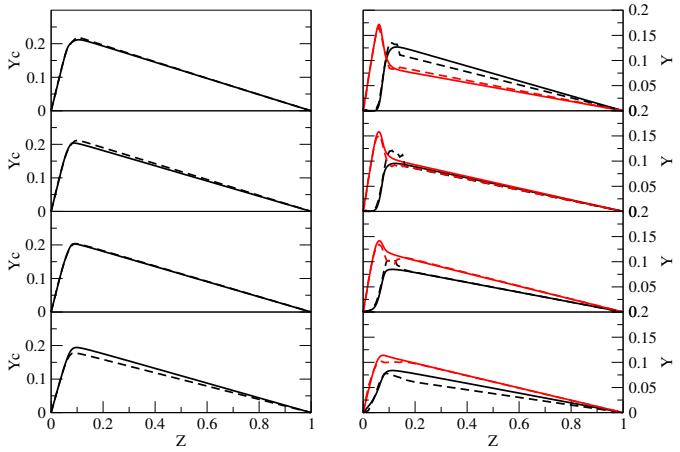

Figure 4.11 – *Evolution with mixture fraction of Y_c (left), Y_{CO} (black) and Y_{CO_2} (red) (right) for the four steady flames computed (from top to bottom* 1, 10, 100 *and* 1000 s^{-1}*). Dashed line: approximate diffusion flame. Solid line: reference flame.*

The results of the steady flames are presented in terms of Y_c, Y_{CO} and Y_{CO_2} in Fig. 4.11. The first observation is that the Y_c profiles are correctly retrieved for the three lowest values of the strain rate. For $a = 1000$ s^{-1} the ADF profile is below that of the reference flame. This can be explained by the fact that this strain rate is close to quenching value: in this situation, the fact that only Y_c diffuses in ADF leads to non negligible errors in the diffusion term evaluation. Y_{CO} and Y_{CO_2} are globally retrieved for all strain rates. In particular, the non zero Y_{CO} values observed in lean mixtures because of the decrease of Y_c with strain rate, is well retrieved by the ADF/DHR calculations (see e.g. for $0 < Z < 0.05$ for the case $a = 1000$ s^{-1}). However, in very rich mixtures (here approximately for $Z > 0.15$), significant discrepancies can be observed. This is explained by the fact that for these mixtures diffusion in mixture fraction space leads to values of Y_c which are larger than the equilibrium value (obtained from a chemical equilibrium calculation). As a consequence, the composition predicted by the table is not correct. It should be noticed that this phenomenon only occurs in rich mixtures for the steady state. Therefore, the composition in the reaction zone (corresponding to the zones where the curvature of $Y_c(Z)$ is not zero) is correctly retrieved, as well as the evolution after ignition (see Fig. 4.10).

Finally, the capacity of the model to retrieve the quenching strain rate has been evaluated. The exact diffusion flame predicts that the quenching strain rate is located between 1000 and 2500 s^{-1}, that is, all tested values with $a \geq 2500$ s^{-1} lead to quenching. The quenching limit found with ADF/DHR is also located between these two values. This shows that the reaction rate provided by the DHR table assumes correct values not only during ignition, but also at high progress variable values found at the extinction limit.

4.5 Evaluation of DHR on Flame D

The DHR model is now evaluated on SANDIA Flame D [103, 104, 105], described in Section 4.5.1 along with the numerical setup used to simulate it. The results obtained are then presented in Section 4.5.2.

4.5.1 Configuration and numerical setup

Flame D is a partially premixed diffusion flame with a Reynolds number of 22400. A fuel/air mixture is injected at 49.6 m/s through an injector of diameter $D = 7.2$ mm. Its fuel/air equivalence ratio Φ is 3.17 and its temperature is 294 K. The flame is piloted by a crown of burnt gases

Table 4.2 – *Conditions of ignition*

Temperature profile (Fig 4.7)	$a[s^{-1}]$	reference flame	Approximate Diffusion Flame
A	1	ignition	ignition
B	1	ignition	ignition
C	1	no ignition	no ignition
A	10	no ignition	no ignition
B	10	no ignition	no ignition
C	10	no ignition	no ignition

at an equivalence ratio of $\Phi = 0.77$, temperature $T = 1880$ K and injection velocity 11.4 m/s. This configuration is surrounded by a coflow of fresh air with a velocity of 0.9 m/s. The LES equations presented in Section 4.3.1 are solved on a cylindrical unstructured tetrahedral mesh with a radius of 20 D and a length of 150 D presented in Fig.4.12. The main and pilot injectors are represented by two coaxial cylinders with a length of 10 mm. Boundary conditions are modeled without using any experimental profiles. This choice is made for two reasons. First, Vreman et al.[70] showed that imposing experimental profiles did not significantly improve the results on this configuration. Secondly, in industrial burners, profiles at the injector exit are never known; therefore in the perspective of applying LES to industrial burners, it is desirable to define a methodology that does not make use of such profiles. As the turbulent flow can not be accurately resolved in the injectors (cells down to 0.01 mm would be required in this case), slip walls are retained as boundary conditions inside the injectors. An analytical turbulent channel flow velocity profile is used for the main jet velocity. Turbulence is injected using the model of Smirnov et al.[106], based on [107]. The RMS velocity was set to 10 m/s for the main jet, in agreement with experimental measurements at $x/D = 1$. For the pilot jet and the air coflow, a simpler flat velocity profile is used, without imposing a turbulent contribution. This choice is made because the momentum of the pilot and air coflows is much smaller than that of the central jet, consequently, only the velocity profiles and turbulence intensity of the central jet have an influence on the jets interactions. For Flame D, the main jet profile is discretized with 15 cells and the pilot with 10 cells. The injection zone is the most refined part of the mesh with a minimum cell size of 0.36mm. The total number of cells is close to 12 millions. On the cylinder sides, a slip wall condition is used while NSCBC non reflective boundary conditions [108] are used at the cylinder outlet. The homogeneous DHR table is presented in table 4.3. Notice that this table is built with only one enthalpy loss point at $\Delta H = 0$, corresponding to adiabatic conditions. This choice is made due to the fact that Flame D shows a low radiative loss of approximately 0.89 kW corresponding to 5% of the total power [109]. Consequently, it can be considered as almost adiabatic. Also, as discussed in the introduction and in Sections 4.3.2 and 4.3.6, the fresh gases temperature of fuel and air in this experiment (300 K) is too low to promote auto-ignition. This means that using a HR type combustion model, i.e. without dilution of the initial fuel/air mixture by burned gases, will lead to no combustion at all. In this situation, only the diluted trajectories of the DHR table ($\alpha > 0$) will allow to initiate reactions.

The table is built with the GRI−MECH 3.0 mechanism [82]. Z_d is set equal to 0.042 which corresponds to the equivalence ratio of the burnt gases coflow. Simulations were run from $t = 0$ ms to $t = 60$ ms to let the flame fully develop in the domain and reach a quasi-steady state. Statistics, which are presented in the following Section, were then acquired considering 160 ms after the initial 60 ms.

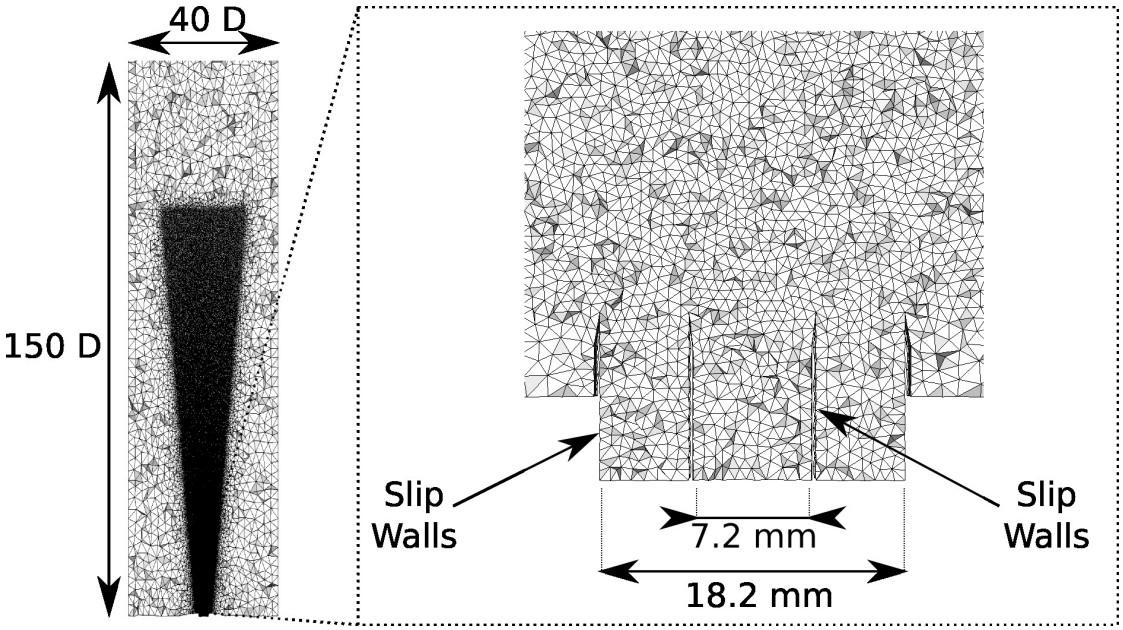

Figure 4.12 – *Flame D computational grid (left) and details of the boundary condition setup for the same grid (right)*

Table 4.3 – *Description of the DHR look-up table used for the Flame D calculations*

Quantity	Number of tabulated values	Minimal value	Maximal value
T_0[K]	1 value 290 K	//	//
Z_0	40	0	1
α	20	0	1
ΔH_d[J/kg]	1 value (adiab)	//	//
Y_c	50	$Y_c(t=0)$ (Eq. (4.25)	$Y_c{}^{eq}(Z, H(Z))$

4.5.2 Results

Figure 4.13 presents the predicted and experimental axial velocity radial profiles at various axial locations from $x/D = 3$ to $x/D = 60$. A fair agreement is found for the mean velocity at all measurement positions, although an overprediction of the order of 20% is found at $x/D = 30$ for the mean axial velocity. The shape of the RMS velocity is correctly predicted by the LES, although an over-prediction is observed at $x/D = 7.5$ for $r/D = 0$. This overprediction might be due to the injection methodology chosen. The same kind of observation was made by Vreman et al. (see Fig. 2.b of [70]) for Flame D, whereas the problem was not observed if the experimental profiles at $x/D = 1$ were used as inlet conditions. Figure 4.14 presents the mean and RMS radial profiles of the normalized mixture fraction at the same measurement positions. Mean mixture fraction predictions are in good agreement with the experiment, although a slight overprediction is shown for $x/D = 30$ and $r/D = 0$. The radial profiles of Z_{RMS} are also correctly predicted, although some deviation from the experimental values can be found at $x/D = 45$. Regarding combustion, the radial profiles of CH_4 are presented in Fig. 4.15, showing a very good agreement with the experiment at every location. Figure 4.16 presents the results obtained for the mean progress of reaction $\tilde{Y}_c$. The agreement between the LES and experiment is globally very satisfactory. It can just be noted that the peak of $\tilde{Y}_c$ is overpredicted between $x/D = 7.5$ and $x/D = 15$. This over-prediction can be attributed to the absence of SGS modeling effect in the DHR model. The radial profiles of the mean H_2O and O_2 (not shown), reflect those of the progress variable. The prediction of the mean CO_2 (not shown), is also quite similar to that of $\tilde{Y}_c$ because CO_2 is the major contributor to $\tilde{Y}_c$. A good agreement is found for the mean temperature presented in Fig. 4.17. Again, as temperature is essentially determined by major product species like CO_2 and H_2O, the agreement in T essentially reflects the one observed for these species.

The prediction of CO, presented in Fig. 4.18, is consistent but less satisfactory than that of previous species. A constant over-prediction of CO is found for the first six measurement positions. In order to explain this observation, the profiles of both CO an CO_2 are presented against the fuel/air equivalence ratio ϕ in Fig. 4.19. Interesting enough, the overestimation of CO and the slight underestimation of CO_2 occur in a very precise range of equivalence ratio, between $0.9 < \phi < 2.2$. This issue is not particular to the DHR model but rather a constant feature of constant mixture fraction tables (either considering premixed flames or homogeneous reactors). For instance, in the study of Fiorina et al. [74], the capability of an FPI database (based on premixed laminar flames) to predict the chemical species of a rich partially premixed flame was investigated. A departure from detailed chemistry was observed in a similar range of ϕ as in Fig. 4.19. This departure was attributed to the absence of diffusion in mixture fraction space when using premixed laminar flames. The same observation can be made in the present study, as diffusion in mixture fraction space is not considered in the DHR table. The same issue was investigated by Vreman et al. [70]. In their work they compared the predictions of a premixed against a non premixed tabulated FGM manifold on Flame D. The CO mass fraction was better predicted with the non-premixed manifold, showing again the importance of diffusion in mixture fraction, while temperature and major species were found quite similar between the two tables. The results obtained with the premixed manifolds in their study are also consistent with those of the DHR model. Nevertheless the global agreement of CO/CO_2 species can be considered as satisfactory for the desired applications targeted here.

4.6 Application to the burner of Verissimo et al.

In this section the burner of Verissimo et al.[14] is chosen to evaluate the DHR model on a configuration which is representative of a furnace working in flameless mode. The burner, presented in Fig. 4.20, is a 10 kW laboratory-scale combustor using methane as a fuel. It is fed with one central injector of pre-heated air (10 mm diameter) and 16 fuel injectors (2 mm diameter) which surround the main central air injector. Air is preheated at 673 K while methane

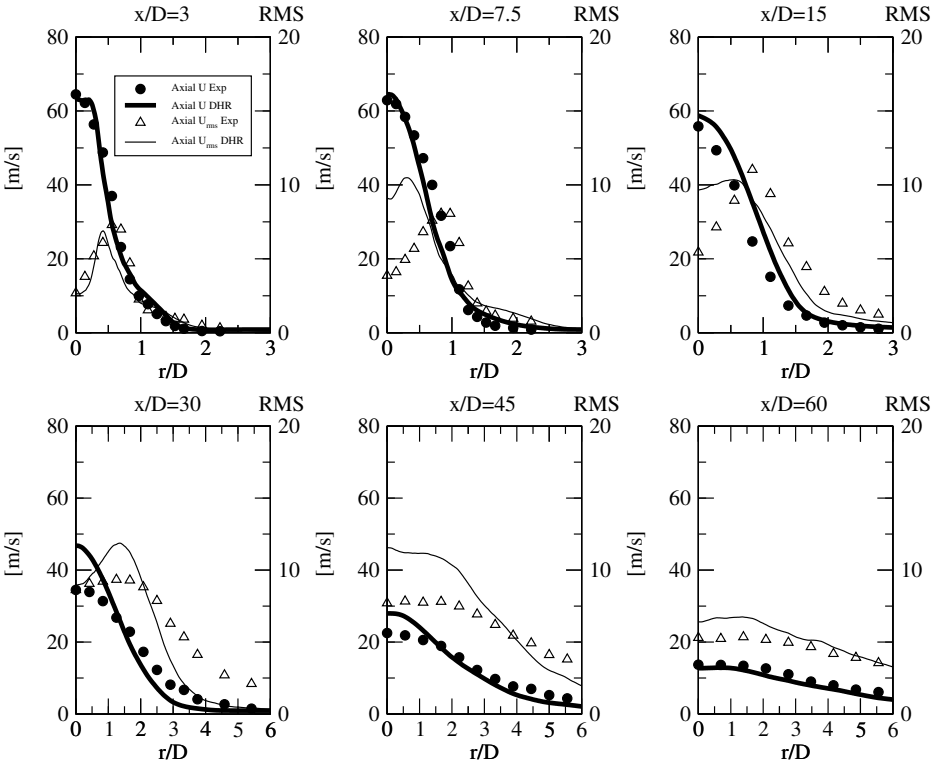

Figure 4.13 – *Mean and RMS axial velocity radial profiles for Flame D.*

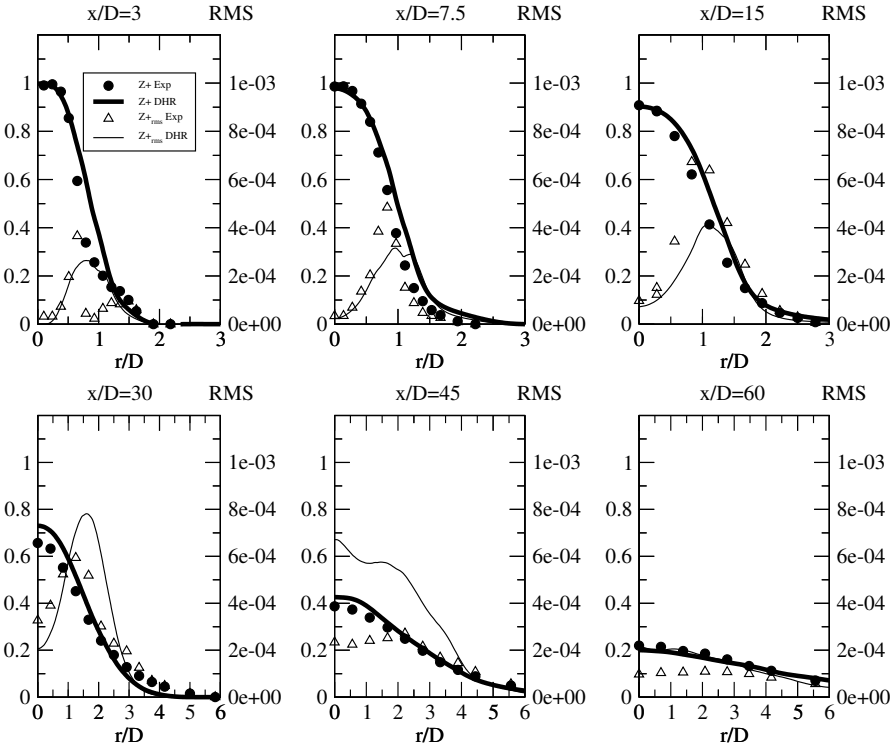

Figure 4.14 – *Mean and RMS normalized mixture fraction radial profiles for Flame D.*

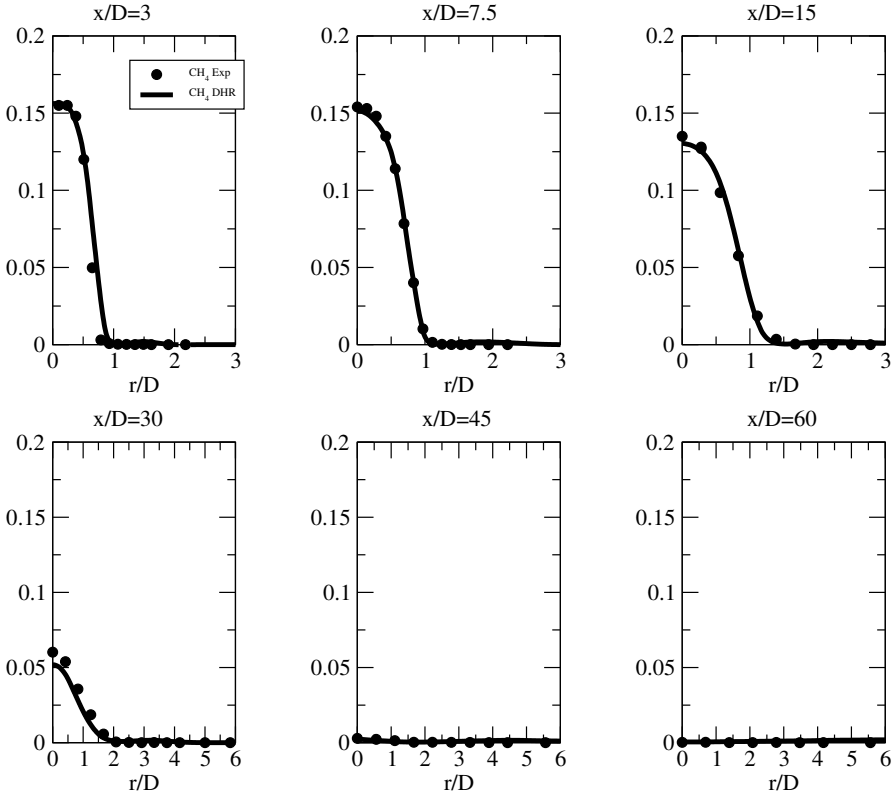

Figure 4.15 – *CH_4 mass fraction radial profiles for Flame D.*

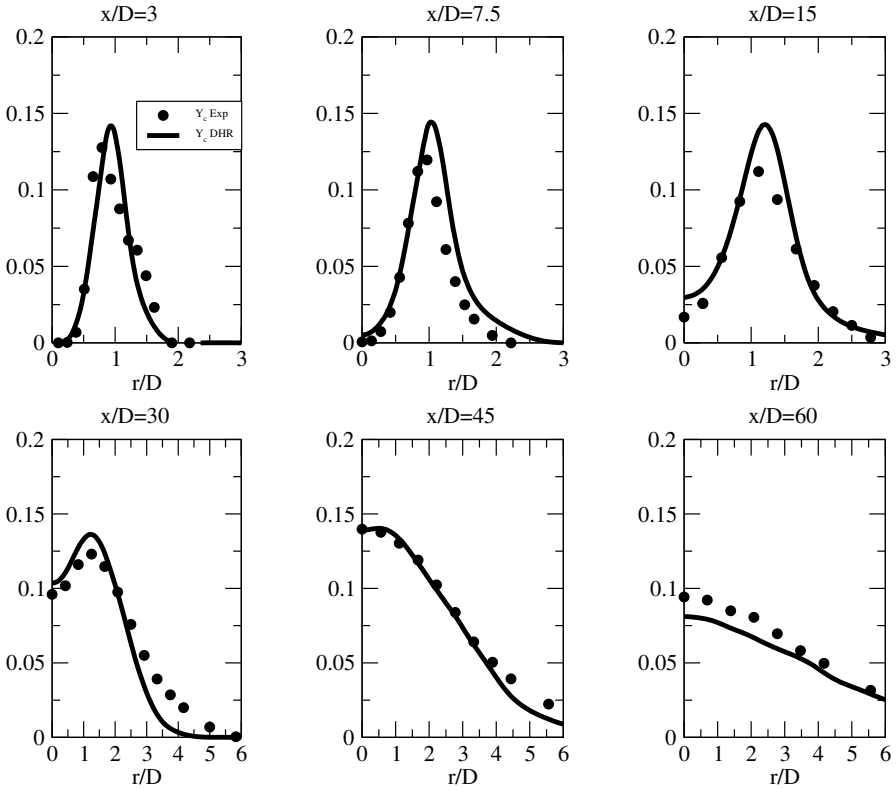

Figure 4.16 – *Radial profiles of the mean progress variable for Flame D.*

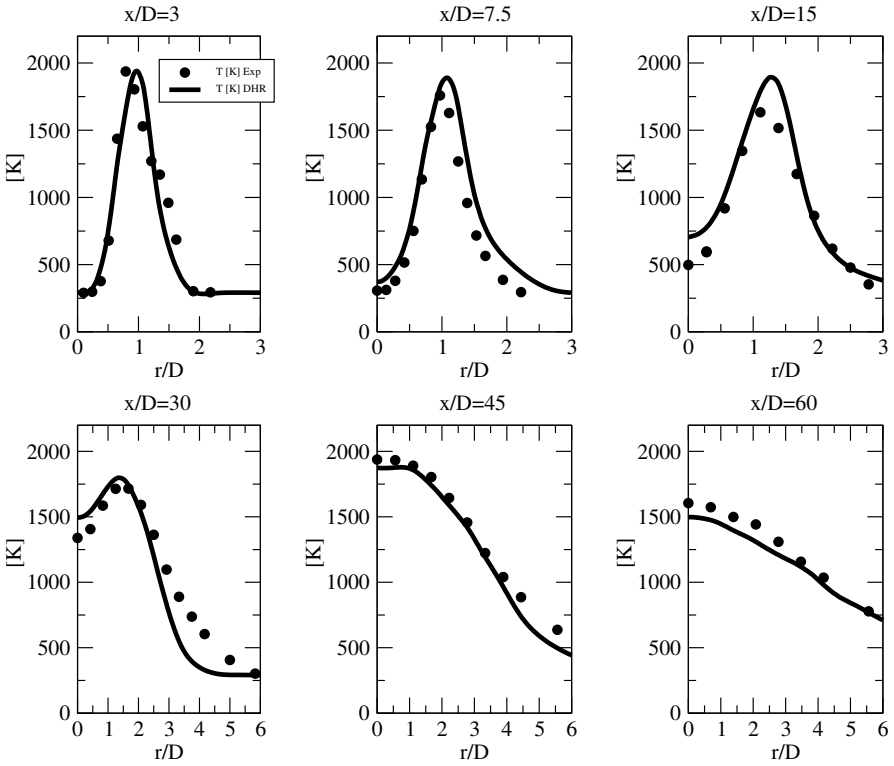

Figure 4.17 – *Temperature radial profiles for Flame D.*

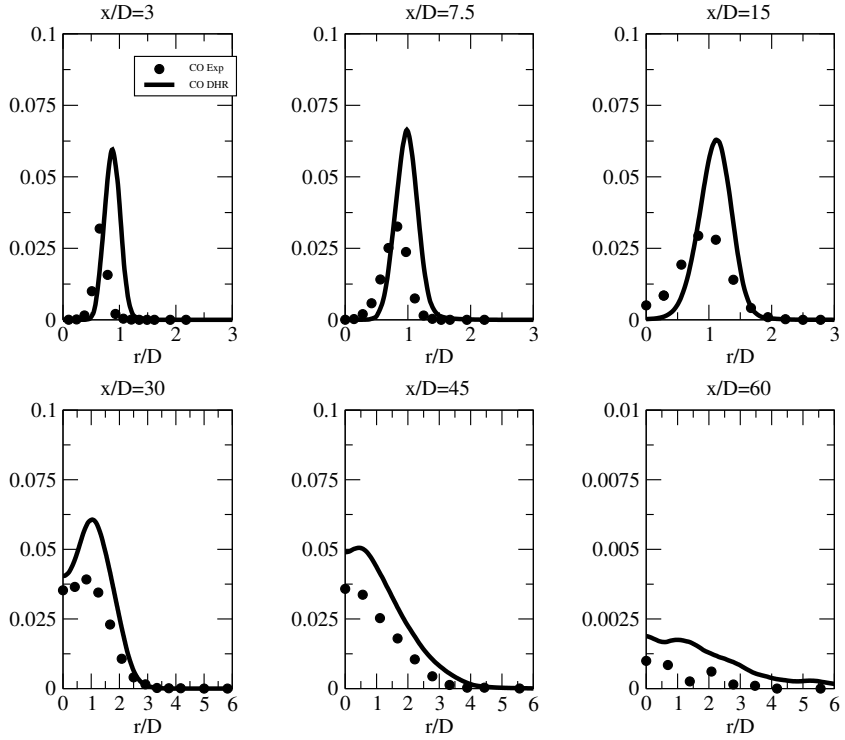

Figure 4.18 – *CO mass fraction radial profiles for Flame D.*

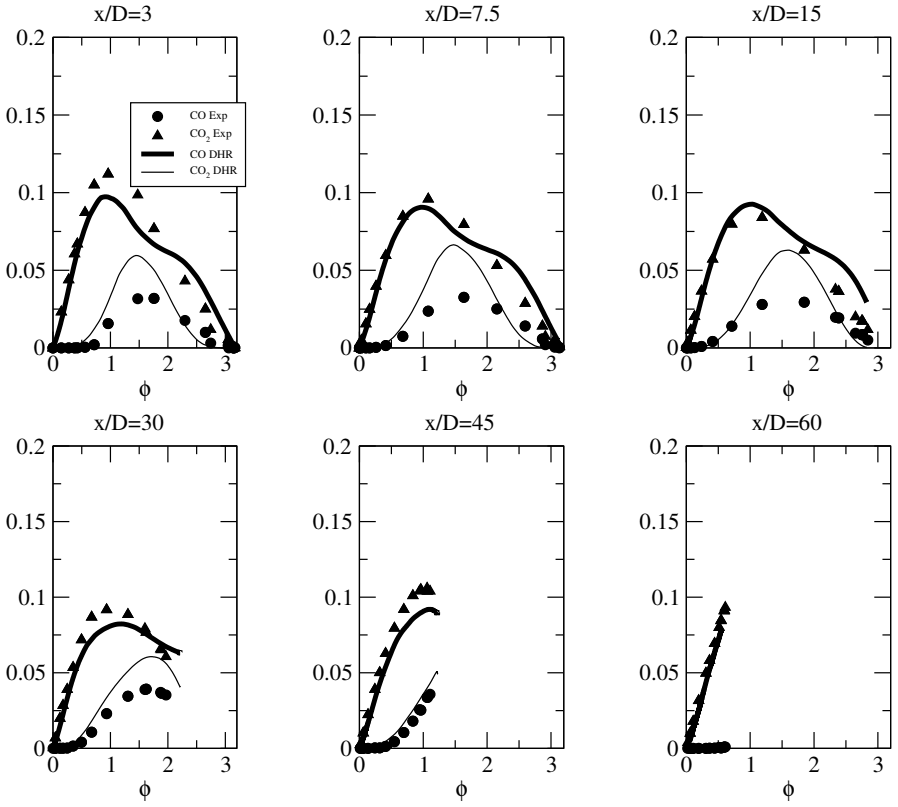

Figure 4.19 – *CO and CO_2 mass fraction profiles versus mean equivalence ratio for Flame D.*

is injected at ambient temperature. The burner is made of a 340 mm long cylindrical part followed by a convergent nozzle of 150 mm length. The burner can work either in flameless or conventional combustion mode by varying the air jet injection velocity. In the present work, the case called RUN2 in [14] is simulated. Its air/fuel equivalence ratio is equal to 1.3. The methane injection velocity is 6.2 m/s and the air velocity is 113.2 m/s. The radial profiles of temperature, CO, CO_2 and O_2 are available at ten axial positions. As velocity was not measured for the reactive configuration RUN2, we first performed an LES of a cold flow case of the same burner carried out by the same team in [86]. The results of this simulation are presented in Section 4.6.1.

The furnace was simulated with a reference mesh containing 20 millions cells. In order to make sure that this reference mesh is sufficient to ensure a correct LES resolution, a refined mesh containing 36 million cells was also considered. This refined mesh corresponds to a decrease of the cell size by approximately 30 % in the jet and heat release regions. A description of the mesh is given in Fig. 4.20, where the computational domain is shown from $x = 0$ to $x = 180$ mm. In order to guarantee a correct prediction of the ternary mixing of fuel, air and burnt gases at the injector exit, the minimum cell size is set to 0.3 mm in the main injector for the reference mesh and 0.2 mm for the refined one (corresponding to $\sim$50 points in the injector diameter). The mesh was also refined at walls where recirculation zones were observed. Boundary conditions use the same approach as for Flame D: a short cylinder of 10 mm length is used for both air and fuel injectors, imposing slip wall boundary conditions. Assuming that the ratio u'^2/U^2 remains close to that of Flame D, the RMS velocity is set to 20 m/s. On the other walls, an iso-thermal wall law is used. For the case simulated, the DHR homogeneous table is presented in table 4.4. For this configuration, $T_0(Z)$ is deduced from the fuel and air inlet conditions as specified in Section 4.3.2. Also, the enthalpy gaps range from $\Delta H_d = 0$ (corresponding to adiabatic burnt gases) to $\Delta H_d = -1395$ kJ/kg (corresponding to $\Delta_{T_d} = -1000$ K from the adiabatic temperature of diluting burnt gases) Z_d was set equal to

Table 4.4 – *Description of the DHR look-up table used for the flameless configuration of Verissimo et al.[14]*

Quantity	Number of tabulated values	Minimal value	Maximal value
T_0[K]	See Section 4.3.2	//	//
Z_0	40	0	1
α	20	0	1
ΔH_d[kJ/kg]	4 values	1395	0 (adiab)
Y_c	50	$Y_c(t=0)$ (Eq. (4.25)	$Y_c{}^{eq}(Z, H(Z))$

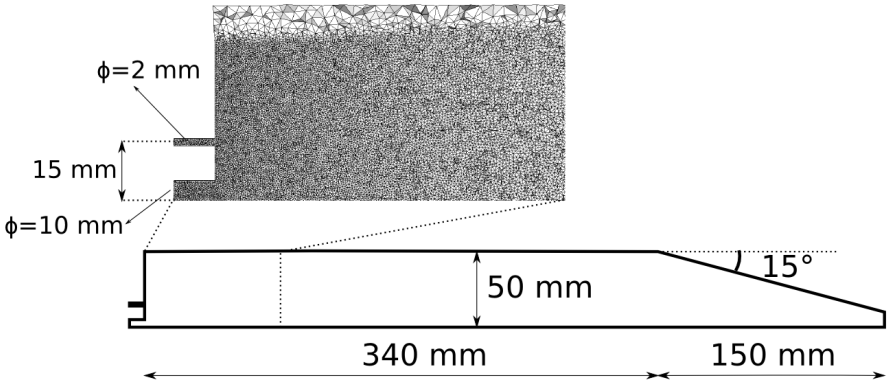

Figure 4.20 – *Schematic representation of the Verissimo burner and detail of the grid used for the DHR simulations presented in Section 4.6*

0.042, corresponding to the air/fuel equivalence ratio $\lambda = 1.3$. Like for Flame D, we observed that non diluted DHR trajectories, i.e. trajectories with $\alpha = 0$, did not lead to auto-ignition. This means that the fuel/air mixture injected in the burner is not able to auto-ignite although air is preheated to 673 K. This illustrates the fact that like in Flame D, a standard HR table, i.e. without dilution, could not be used to perform the simulation, which shows the necessity to use a model like DHR including dilution as a parameter of the model.

4.6.1 Cold flow validation

In order to assess the validity of the injection and turbulence modeling, the cold case called RUN3i in [86] was first simulated. For this case, the air injection diameter is 6 mm instead of 10 mm and the velocity 133.7 m/s. The axial velocity profiles were kindly furnished by the same authors for all axial positions.

Experimental and LES profiles of mean and RMS axial velocity are presented in Fig. 4.21. A dashed horizontal line is placed at $U = 0$ m/s in order to identify the recirculation zone. Radial profiles are very well predicted at all axial positions. The recirculation zone extends from $x = 45$ mm to $x = 250$ mm, that is, on a large part of the burner. The mean value of the velocity in this zone is very low compared to the bulk velocity, with a maximum of -7.2 m/s at $x = 181$ mm. In the reactive cases, this large recirculation zone allows to mix the burnt gases formed close to the burner axis with the fresh gases exiting from the fuel and air injectors. Apart from an overestimation at the first two axial positions, the RMS are also quite

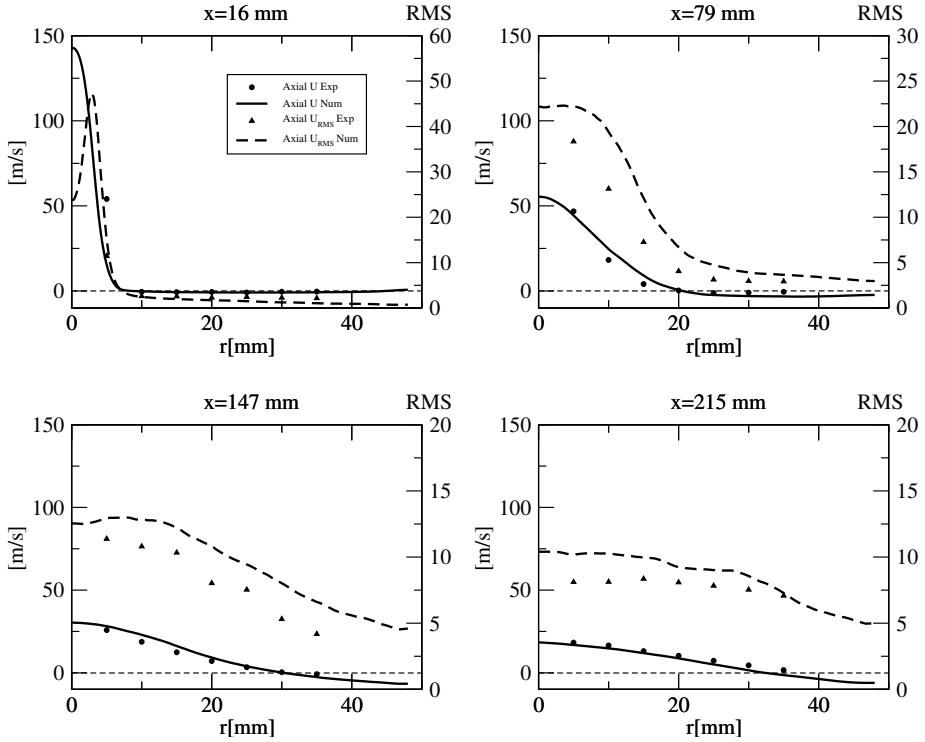

Figure 4.21 – *Mean and RMS axial velocity profiles for the cold flow case of Verissimo.*

well predicted. These results show the ability of the LES solver and set-up to reproduce a cold flow in this configuration, which is a prerequisite before assessing the DHR combustion model on the reactive cases.

4.6.2 DHR results on the flameless case

In the experiment [14], the major source of enthalpy loss comes from the heat losses at walls and corresponds approximately to half of the burner power (private communication from the authors). As wall temperature was not measured, the wall temperature is fitted in the LES to recover approximately the experimental temperature level at the last measurement position at $x = 310$ mm. Following this procedure, $T_w = 700$ K was retained.

The axial profiles of temperature, O_2, CO_2 and CO are presented in Fig. 4.22 for the two mesh resolutions. It is first observed that the transition from the fresh gases state to the burnt gases state takes place essentially between $x = 45$ mm and $x = 113$ mm and is well reproduced by the DHR model for both meshes, although temperature prediction is more accurate with the refined mesh. The temperature increase is accompanied by a simultaneous decrease of O_2 and increase of CO_2. On the other side, CO behaves more like an intermediate species which marks the reaction zone. The experimental axial profile of CO is qualitatively well captured by the LES. The location of its peak value is well captured by the reference mesh while it is located too upstream for the refined mesh. On the contrary, the CO decrease for x>147 m is slightly too slow with the reference mesh, while it is better predicted by the refined mesh. This shows that the reaction zone is moved slightly upstream with the refined mesh compared to the reference mesh.

2D instantaneous snapshots of temperature, under-adiabaticity factor $\tilde{c}_H$, axial velocity and progress variable reaction rate $\tilde{\omega}_{Y_c}$ are presented in Fig. 4.23. These images confirm that

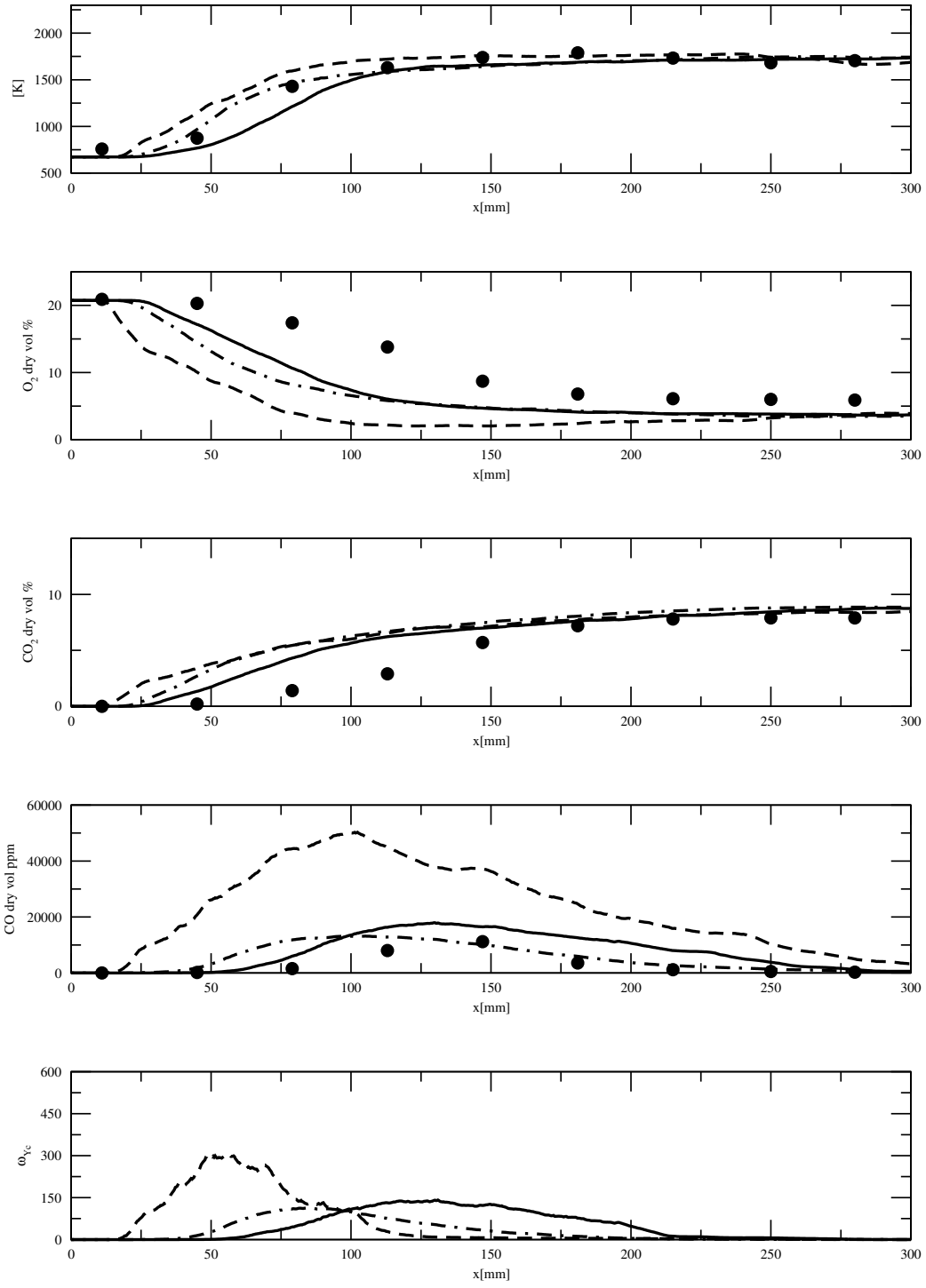

Figure 4.22 – *Axial profiles of the mean temperature, O_2, CO_2, CO mass fractions and progress variable reaction rate for the flameless case. Symbols: experiments; Solid line: DHR model with the reference mesh; Dash-dot: DHR with the refined mesh; Dashed lines: adiabatic DHR ($\tilde{c}_H = 1$).*

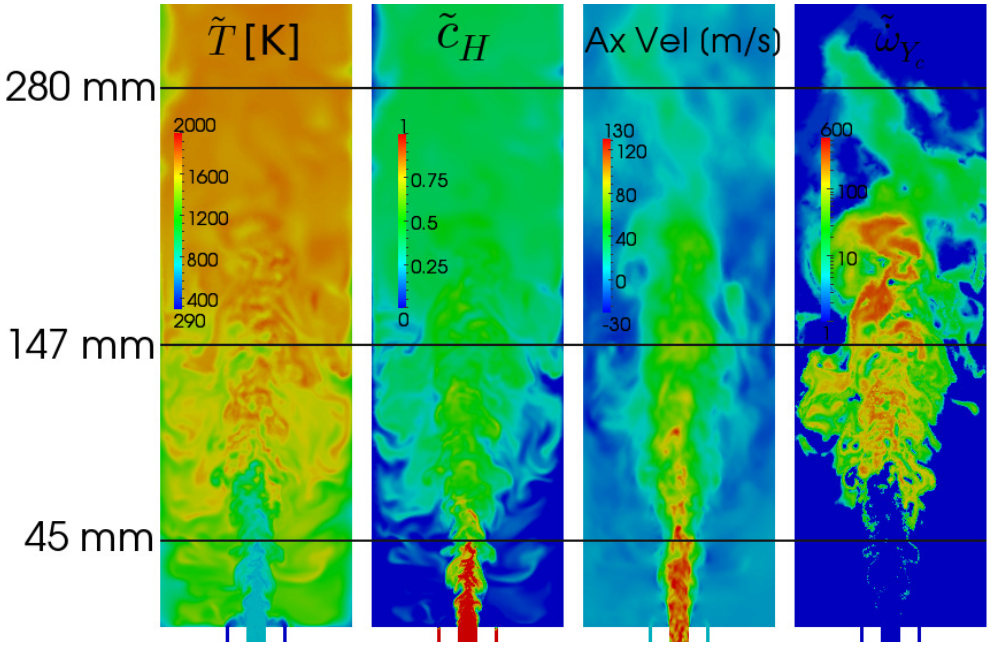

Figure 4.23 – *Instantaneous fields of temperature, under-adiabaticity factor $\tilde{c}_H$, axial velocity and progress variable reaction rate $\tilde{\dot{\omega}}_{Y_c}$ for the flameless case of Verissimo et al.[14].*

the temperature increase is very progressive without any visible peak, in coherence with the reaction rate. $\tilde{c}_H$ assumes values of the order of 0.5 approximately corresponding to $\Delta T_d \sim$ 491 K in the major part of the reactive region, while it falls to values close to zero in the region located close to the upstream corner of the combustor.

This variation of $\tilde{c}_H$ is explained by the decrease of the diluent gases enthalpy when following the recirculation flux from the downstream to the upstream part of the burner. The reaction rate field confirms that the reaction zone is detached from the injector leaps and that it extends over a very large volume fraction of the combustor.
Figures 4.24, 4.25 and 4.26 present radial profiles of the same quantities at various axial locations between $x = 11$ mm and $x = 310$ mm for the two grids. At $x = 11$ mm one can notice a strong under prediction of temperature close to the jet axis: in the LES the temperature remains close to the air injection temperature of 673 K while in the experiment it is close to 1250 K. In order to understand this discrepancy, we consider points A and B located at $z = 11$ mm and $r = 0$ (A) and 5 mm (B) respectively. These points are represented in Fig. 4.27 in terms of temperature, mixture fraction, CO, CO_2 and O_2 concentrations. In this figure, the equilibrium compositions at various mixture fractions are also presented, for adiabatic (circles) and non adiabatic conditions (triangles) corresponding to $\Delta T_d = 500$ K. From this figure it can be observed that point A corresponds quite accurately to the inlet air state, apart for the 1 ppm CO concentration, which can be attributed to the measurement uncertainty. On the contrary, point B corresponds to a very low $Z_l \simeq 0.015$ or rich $Z_r \simeq 0.155$ mixture fraction, as it can be seen on the Z-T plane of Fig. 4.27a. If one looks at the CO_2-T and O_2-T plots, it can be seen that the experimental temperature is above the adiabatic equilibrium state. Therefore, to make the comparison, we now only consider the adiabatic conditions marked with circles. From the CO_2-T plot, point B is seen to be close to the richer condition Z_r. On the O_2-T plane, point B corresponds on the contrary to a lean mixture and is very far from the rich condition which presents an O_2 mass fraction close to zero. Finally on the CO-T plane, point B does not match neither the rich nor the lean composition. These plots first show that point B does not correspond to a standard equilibrium state and could therefore not be retrieved by the DHR calculation, at least without taking radiations into account. Assuming all measurements are reliable, the only possibility to approximately match the experiment with an equilibrium state

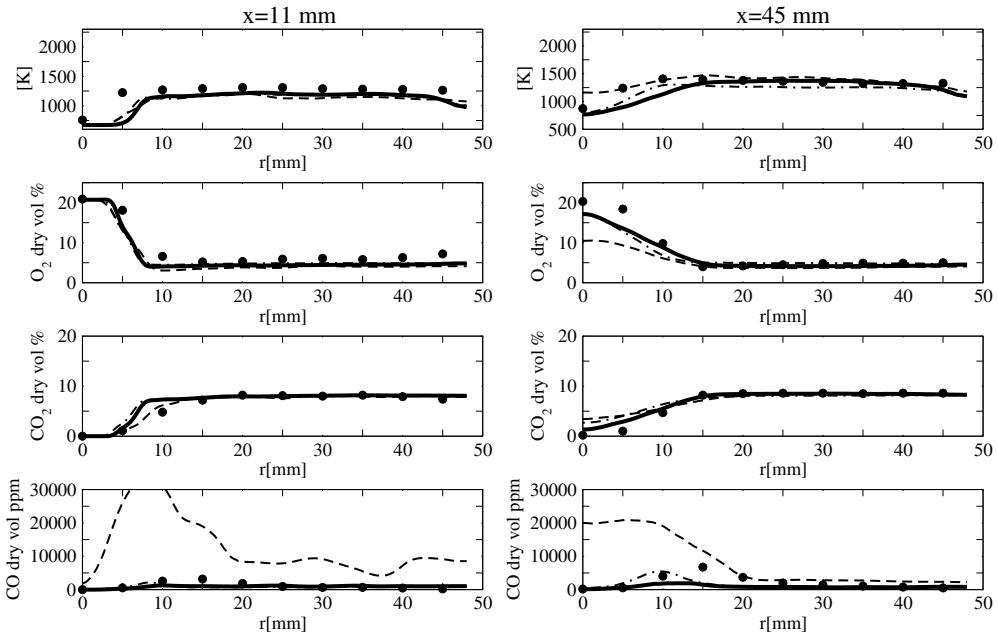

Figure 4.24 – *Radial profiles of mean temperature T, O_2, CO_2 and CO at $x = 11$ mm and $x = 45$ mm. Symbols: experiments. Solid line: DHR with the reference mesh; Dash-dot: DHR with the refined mesh; Dashed lines: adiabatic DHR ($\tilde{c}_H = 1$).*

is to consider that point B corresponds to a lean mixture at Z_l with a temperature increase of more than 150 K, which is the explanation proposed by the authors (private communication). As air enters at a high velocity of 113 m/s in the domain, its residence time at point B is approximately 1μs. This time seems extremely short for getting such a temperature increase. As no radiation model was used in this LES, it is difficult to further justify this view. Alternatively, one can suspect a problem in the measurement of temperature or species concentrations at this location, as already suggested by Cuoci et al.[88]. At this point, it is difficult to conclude on this issue, complementary measurements and simulations being necessary.

Fig. 4.28 presents instantaneous fields of the turbulent diffusivity divided by the molecular diffusivity for the two meshes employed. It can be seen that μ_t/μ remains always smaller than 10 for both the grids. As suggested in [110], values smaller than 10 for the μ_t/μ ratio, confirm that the mesh resolution is very good in both cases.

Further downstream, the mixing between air, fuel and burnt gases proceeds up to $x = 147$ mm and $r < 15$ mm approximately. In this region temperature is correctly predicted while O_2 is underpredicted and CO_2 is overpredicted, with no significative differences between the two grids. The CO profile is strongly under-predicted up to $x = 45$ mm which could denote a lack of reactivity in this region, in coherence with the under-prediction of temperature. Further downstream it assumes both a correct shape and order of magnitude.

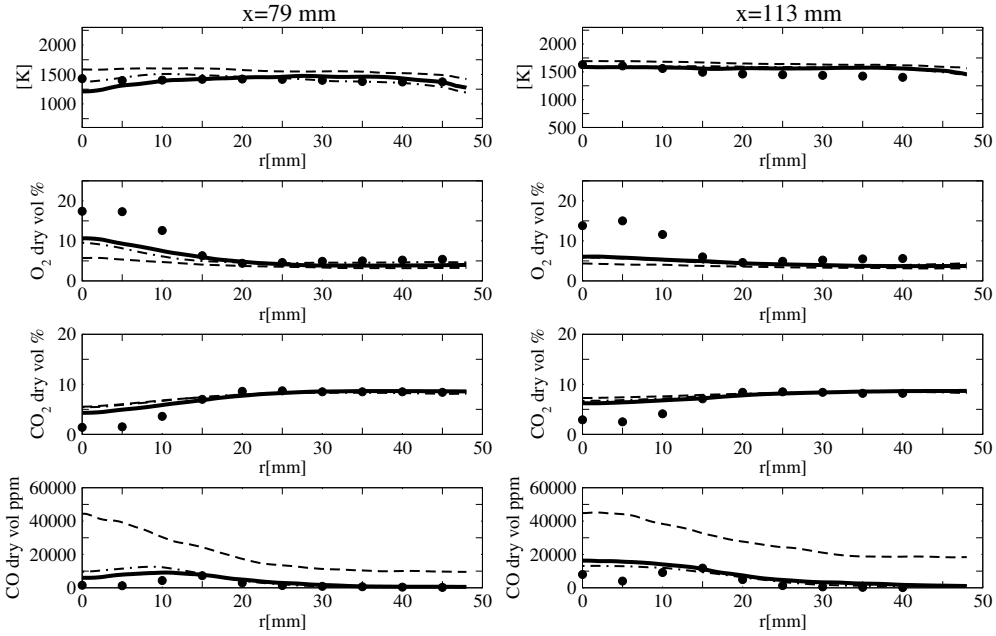

Figure 4.25 – *Radial profiles of mean temperature T, O_2, CO_2 and CO at $x = 79$ mm and $x = 113$ mm. Symbols: experiments. Solid line: DHR with the reference mesh; Dash-dot: DHR with the refined mesh; Dashed lines: adiabatic DHR ($\tilde{c}_H = 1$).*

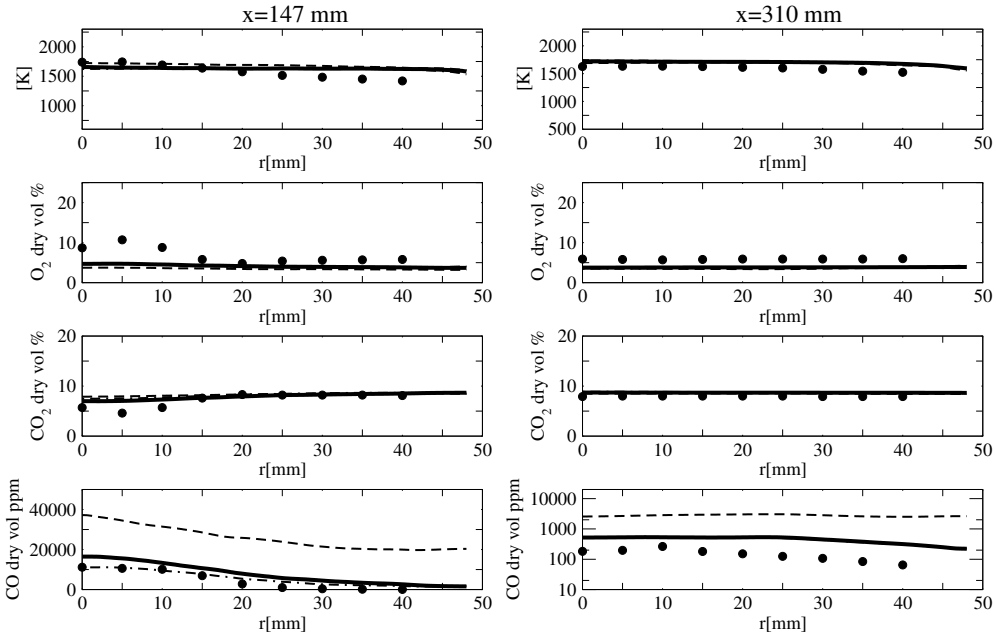

Figure 4.26 – *Radial profiles of mean temperature T, O_2, CO_2 and CO at $x = 147$ mm and $x = 310$ mm. Symbols: experiments. Solid line: DHR with the reference mesh; Dash-dot: DHR with the refined mesh; Dashed lines: adiabatic DHR ($\tilde{c}_H = 1$).*

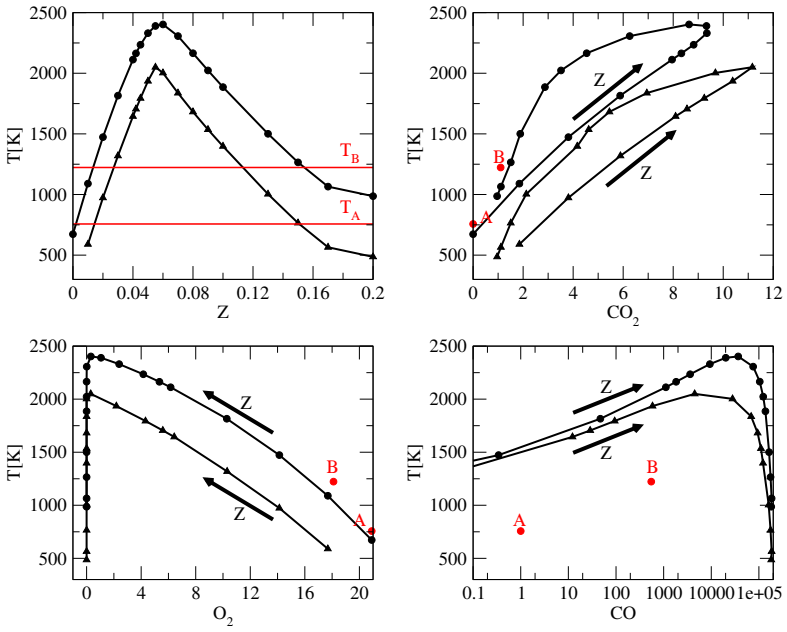

Figure 4.27 – *Temperature equilibrium state for a diluted reactor using Verissimo boundary conditions for T_F, T_A and Z_d. Calculations performed with adiabatic (black circles) and non-adiabatic temperature gap (black triangles, $\Delta T_d = -500K$). Experimental results corresponding to points $[x = 11\text{mm}, r = 0\text{mm}]$ (red circle A) and $[x = 11\text{mm}, r = 5\text{mm}]$ (red circle B). Clockwise: Temperature versus mixture fraction, CO_2, O_2 and CO.*

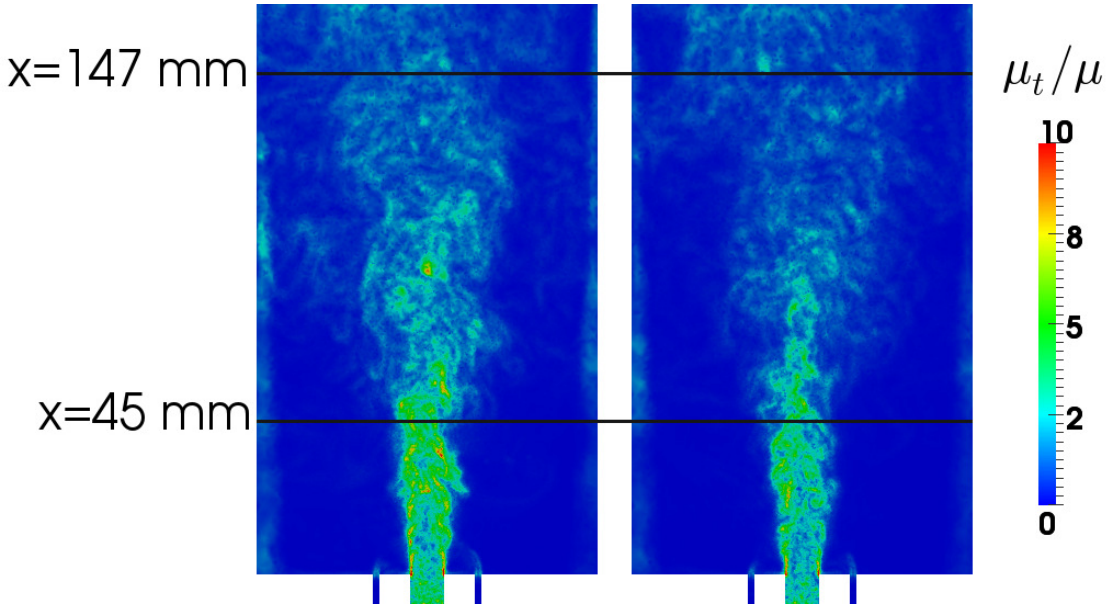

Figure 4.28 – *Instantaneous fields of turbulent/laminar viscosities for the flameless case of Verissimo et al.[14]. Left: Reference mesh; Right: Refined mesh.*

Between $x = 147$ mm and the last measurement location at $x = 310$ mm, temperature, O_2 and CO_2 profiles tend to flatten, indicating the end the heat release region. In this region, the agreement with the experiment is good, showing that the global reaction rates of O_2 and CO_2 are correct and that the enthalpy loss through the walls is well adjusted. The profile of CO assumes a correct shape but it is overpredicted with a maximum value of 500 ppm against 200 ppm in the experiment. This overprediction is attributed as said before to a slightly too slow reactivity in the downstream part of the combustor. These results shows that the DHR model globally succeeds in reproducing this flameless configuration, with better results than those of RANS presented in [84] and [88]. At the same time, improvements to the model might be necessary to model the near injection region and the CO profiles.
In order to assess the importance of the heat losses in the present flameless configuration, and more generally in furnaces, Fig. 4.22, 4.24, 4.25 and 4.26 also present the results obtained with DHR imposing $\tilde{c}_H = 1$, that is, considering only the adiabatic DHR table. As shown in Fig. 4.22, the mean progress variable reaction rate is two times larger in the adiabatic simulation compared to the reference non-adiabatic simulation. This reactivity variation was already observed in Fig. 4.5 and is entirely due to the impact of the diluent enthalpy loss on the initial temperature of the mixture. As a consequence of this larger reactivity, the flame reaction zone is moved upstream compared to the reference DHR solution. This in turn leads a less diluted combustion (as dilution of the fresh mixture by burned gases increases continuously along the jet), leading itself to a much higher peak temperature. As a consequence, temperature is largely over-predicted for the adiabatic simulation in the flame region, O_2 is under-predicted and CO_2 is over-predicted. On the contrary, further downstream, temperature, O_2 and CO_2 profiles for the adiabatic and non-adiabatic simulations are very similar. This is explained by the fact that in the present LES solver, an equation for energy is transported. Therefore, even if an adiabatic table is used, the enthalpy losses at walls are also accounted for in the adiabatic simulation, leading to a correct estimation of the total enthalpy in the domain. Besides, the differences on O_2 and CO_2 mass fractions close to equilibrium are sufficiently low between the adiabatic table and the non adiabatic table to allow a correct reproduction of these major species. As a consequence, temperature, which is deduced from enthalpy and species mass fractions, is also correctly recovered in the adiabatic case. On the contrary CO presents a strong sensitivity to the enthalpy value: while the order of magnitude is correctly predicted for the reference

DHR calculation, it is correctly predicted in the reference DHR simulation, it reaches almost 5000 ppm in the adiabatic simulation.

4.6.3 Structure of the Verissimo flameless burner

In order to better understand how combustion takes place in this flameless case, Fig. 4.29 presents a scatter plot of total enthalpy $\tilde{H}$ versus $\tilde{Z}$ at different axial positions. The scatter plot at each position includes all mesh points located at $+$ or $-$ 5 mm from the considered position. As total enthalpy and mixture fraction are passive scalars, they allow to figure out the evolution of mixing in the chamber. In this figure, the air inlet condition is labelled "A" and corresponds to point $Z = 0$ and $H = 390$ kJ/kg while the fuel inlet condition is labelled "F" and corresponds to point $Z = 1$ and $H = -4640$ kJ/kg. The point labelled D^{ad} corresponds to the diluent mixture fraction $Z_d = 0.042$ at the adiabatic condition, that is, on the mixing line A-F defined by inlet states A and F. point D in this figure represents the diluent mixture fraction at the minimum enthalpy observed in the calculations corresponding to $\Delta H_d = -1395$ kJ/kg approximately, or $\Delta T_d = -800$ K. It can be first observed that nearly no computing point falls on the mixing line A-F. This means that direct mixing of fuel with air, which could lead to a standard combustion mode like in a counter-flow laminar diffusion flame, is not taking place. This observation can be explained by the strong mixing of the fuel and air jets with diluent which impedes a direct mixing of fuel with air. This is evidenced for $x \leq 11$ mm by the numerous points lying on the mixing line D-F showing that the fuel jet essentially mixes with diluent gases at a state close to state D, that is, burnt gases at Z_d with the lowest enthalpy. These burnt gases are at the lowest enthalpy because as the fuel/diluent mixing essentially takes place close to the fuel injectors, these burnt come from the long lateral recirculation zone, therefore experiencing the maximum wall heat loss. Concerning the air jet, it can be observed that it preferentially mixes on a line defined by points A and DF. Point DF is located on line D-F, with a mixture fraction $Z \sim 0.35$, which tends to decrease as x increases. The mixing line defined by points A and DF indicates that air mixes preferentially with an already highly diluted fuel stream. Further downstream, for $11 \leq x \leq 33$ mm, a second mixing line defined by points A and D becomes important. It corresponds to the direct mixing of the remaining air flow with the diluent gases of the recirculation zone. The scatter plot shows that the points which do not lie on these three mixing lines are essentially located inside the triangle defined by these three lines. These points therefore correspond to intermediate mixing trajectories. As no point lies below line D-F, it also shows that the minimum value of $\Delta H_d = -1395$ kJ/kg used in the DHR table is sufficient to describe all the enthalpy states observed in the calculation. Between $x = 11$ mm and $x = 33$ mm, the maximum mixture fraction decreases from 0.75 to 0.10, indicating that the fuel stream is getting rapidly mixed with diluent gases and air. At $x = 250$ mm, mixture fraction is nearly constant and equal to Z_d. On the contrary, a non negligible enthalpy variation can be observed, the highest enthalpy corresponding to the gases located close to the chamber axis, the lowest enthalpy corresponding to the gases located close to the walls.

4.7 Conclusions

A LES combustion model devoted to non-premixed combustion under furnace conditions was proposed in this paper. This model was designed to maintain a reduced CPU cost thanks to tabulation, while allowing to represent three major features of non-premixed furnace combustion, and in particular flameless combustion: combustion of a three-feed mixture, auto-ignition of the mixture, and high under-adiabaticity of the diluent gases. Two major assumptions were made. The first one is that the burnt gases are at the mean furnace mixture fraction Z_d, while their enthalpy is considered as an additional parameter of the model. The second one is that the micro-mixing description, that is the scalar dissipation rate, can be neglected at first or-

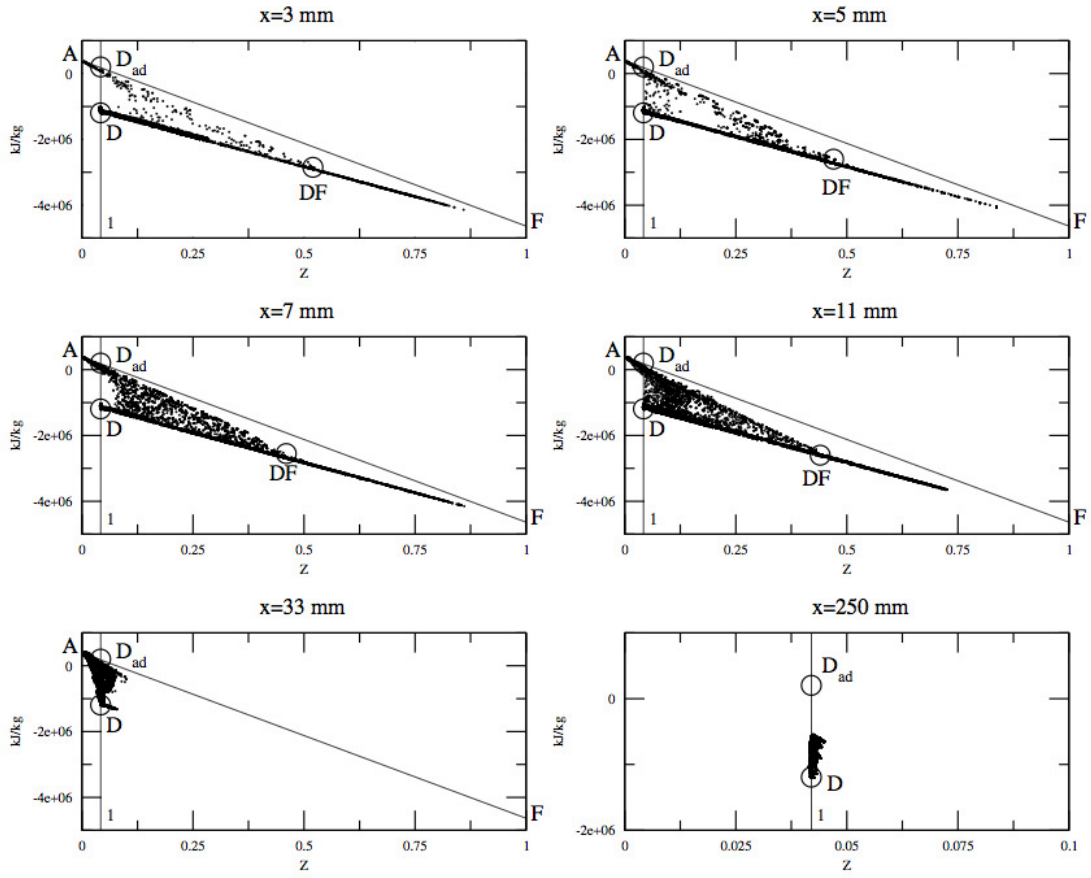

Figure 4.29 – *Scatter plots of the total enthalpy versus mixture fraction at various axial positions for the flameless case.*

der. This second hypothesis allows to consider simple homogeneous reactors for tabulation, composed of fuel, air and burnt gases at equilibrium.

It was first shown that this model allows to correctly reproduce the auto-ignition of a laminar counterflow diffusion flame ignited by a hot spot. It was then assessed on Flames D. For this flame, satisfactory results were obtained for passive scalars, temperature and major product mass fractions. A slight tendency to over-predict the mixture reactivity was observed due to the insensitivity of the model to the effect of scalar dissipation at the SGS level. Such an observation was already made by [70] with a different approach which also neglected scalar dissipation. The DHR model was finally evaluated on the flameless burner of Verissimo et al.[14]. The model correctly recovered the absence of temperature peak typical of flameless combustion. Close to the fuel and air inlets, an incoherence was suspected in the experiments between temperature and O_2 and CO_2 mass fractions. Therefore, it was not possible to conclude on the model predictivity in this region. Further downstream, temperature and species profiles were found in good agreement with the experiment. An additional DHR calculation was performed assuming adiabatic instead of under-adiabatic diluent gases. This calculation lead to an over-prediction of the mixture reactivity and temperature, therefore confirming the importance of the burnt gases under-adiabaticity for furnace applications. A mesh sensitivity analysis was also conducted using a refined mesh. Slightly improved results were obtained with the refined mesh compared to the reference mesh, showing that the reference mesh had already a correct resolution and that the DHR model has a correct sensitivity to mesh refinement. An analysis of scatter plots on a mixture fraction/total enthalpy plane allowed to figure out how the ternary mixing is taking place in this combustor. It was found that as expected in a flameless configuration, fuel is first strongly diluted with under-adiabatic burnt gases prior to its mixing with the air jet.

In the present version of the DHR model, the dilution fraction α is chosen in the LES as the lowest value α_{reac} allowing auto-ignition in the DHR look-up table. In the future, a more refined approach to determine α will be investigated, for instance by defining a model transport equation for α.

5 Pollutant modelling in flameless combustion

In this chapter, the article A tabulated, flamelet based NO model for Large Eddy Simulations of non premix turbulent jets with enthalpy loss *submitted to the journal* Flow Turbulence and Combustion *is reported. In the article, the diffusion flames - NO relaxation approach DF-NORA is presented: the model tracks the relaxation towards equilibrium of the NO source term as a function of mixture fraction, scalar dissipation and a progress variable. The model is compared to two pre-existent models, the NORA model [111] and the linear approach of Ihme et al.[112]. The article is divided into two parts. In the first part, the model is presented along with the other two approaches used; in the second part it is validated over the two 3D configurations, the Flame D of Sandia and the FC combustor from the works of Verissimo et al. In Appendix A, an analysis of the turbulence radiation interactions is presented. In Appendix B, an intermediate NO model based on ADF-PCM is presented. This model, which could be called "ADF-NORA", did not allow to recover correct NO profiles on a diffusion flame because of the approximated flamelet resolution used in ADF. It is presented to show why in the end the exact resolution of the laminar diffusion flame (DF) was retained in DF-NORA.*

5.1 ABSTRACT

Three LES models devoted to the NO prediction in under-adiabatic furnaces are evaluated in this paper: the NORA (NO relaxation Approach) of Vervisch et al., based on the NO relaxation towards equilibrium, the linear model (LM) of Ihme and Pitsch based on the equilibrium state of a laminar diffusion flame and a new model, DF-NORA, in which the linear approximation of the LM is replaced by a tabulation of the reaction rate as a function of a NO progress variable, following the idea of Zoller et al. To generate this table, NO relaxation complex chemistry calculations are used like in NORA, but the homogeneous reactor is replaced by a steady laminar diffusion flame. These models are validated on Sandia Flame D and on the flameless case of Verissimo et al. [14]. For both cases, NORA underpredicts the NO production due to its insensitivity to strain, while LM overpredicts NO by a factor 2 on Flame D and a factor 13 on the flameless case. DF-NORA presents the best prediction with a maximal underprediction of 30% on Flame D and an over-prediction of 30% on the final NO yield of the flameless case. The impact of a radiative source term is also assessed on Flame D, showing a local decrease of NO by less than 7% compared to the adiabatic calculation for the DF-NORA model.

5.2 Introduction

The environmental emergency has brought to increasingly stringent legislations to reduce global warming and pollutant related issues. The main responsible for these pernicious effects are the combustion systems, which supply approximately 80% of the worldwide energy produced [1]. In preventing global warming and pollution, efforts are addressed both towards

CO_2 and nitrogen oxides NO_x. If CO_2 is the main responsible for global warming, NO_x species have both local and global harmful effects. On a local scale, NO_x and SO_x formed during a combustion process convert into sulphuric and nitric acids. These acids modify the pH of the atmospheric precipitations and can have a strong impact on surface waters, forests and human health [113]. On a more global scale, NO_x converted into NO_2 react with the atmospheric ozone [114], yielding to ozone depletion which contributes to global warming worsening.
In a combustion process, several routes are identified for NO_x formation. The Zeldovitch's thermal route becomes predominant at high temperatures and lean mixtures [115]. It includes seven species:

$$O + N_2 \rightleftharpoons NO + N \tag{5.1}$$
$$N + O_2 \rightleftharpoons NO + O \tag{5.2}$$
$$N + OH \rightleftharpoons NO + H \tag{5.3}$$

The second major source of NO_x is the Fenimore or Prompt route [116], which is favored by rich conditions. Another important contribution to NO_x formation is the NO_2 path [117] for which there is experimental evidence that it is mostly originated in the reaction region [118, 119].
In most combustion devices like high-temperature burners, internal combustion engines or gas turbines, thermal NO is the major source of NO_x pollutants. For this reason, it is highly desirable to reduce temperature peaks and local O_2 rich regions, in order to mitigate the favoring factors of the thermal NO path. In this sense, flameless combustion is one of the more attractive technologies [13, 19] (FC in this manuscript) to reduce NO_x emissions. In FC, fuel and air are strongly diluted by burnt gases while oxidizer air is pre-heated to stabilize the process. This leads to a much less polluting and more efficient technology.
However, the favorable conditions to effectively reduce NO in the FC regime are not obtained systematically and easily: they highly depend on the fuel/air ratio, inlet temperatures and burner geometry. For this reason, analytical tools fail to predict the FC mode region in the parameter space of the burner. For this reason, CFD is a very attractive tool for studying FC, which is still in an early age. Numerous examples of numerical simulation of FC were already presented both using RANS [55, 40] and LES[48, 49, 92, 120]. With regard to NO prediction, a generic but expensive approach is to resolve and transport the entire fuel oxidation and NO mechanism in the CFD code, a methodology employed in all combustion models using a direct resolution of the chemical mechanism like CMC [121, 122]. To reduce computational costs for both combustion and NO, tabulated models represent an alternative approach. However, NO chemistry presents a different time scale with respect to fuel oxidation [123, 124, 125], so that its tabulation can not be tied to that of fuel oxidation. This aspect was clearly shown in [70], in the diffusion flames context, where the NO species was directly tabulated from the combustion manifold, yielding to a large overestimation with respect to experimental data. Also, it was shown a significant improvement, when the NO reaction rate was tabulated instead. In this sense, models with the NO reaction rate tabulated were developed both considering homogeneous reactors [126, 111, 127] and flamelet [112, 119] tabulations.
In FC the ternary mixing occurs in a turbulent environment, yielding to highly strained regions, whereas the strain rate observed in the surrounding recirculated burnt gases is negligible. For this reason, a comprehensive model which accounts for NO formation in both strained and non strained regions is proposed in this paper. For non strained regions, the NO relaxation approach (NORA) model presented in [111, 127] is considered. The model tabulates the NO characteristic time during its relaxation towards equilibrium. For strained regions a flamelet approach based on the model of Ihme et al. [112] is retained. In [112], NO reaction rates at equilibrium are considered to predict NO in a diffusion flame, introducing a linear relation for the backward NO reaction. This approach resulted in a large overestimation of the NO in non-premixed configurations. Zoller et al. [119] argued that this linear hypothesis was too strong, as species such as NO_2 and N_2O can yield to non-linearities during the relaxation towards equilibrium of NO. In the present work, the non-linearities of the NO relaxation in a flamelet structure are considered and included in a tabulated approach based on the Linear Model (LM) proposed in [112]. This model is called Diffusion Flames - NORA (DF-NORA). In

this work, DF-NORA was validated on both non-premixed and flameless configurations. For the combustion part of both test cases, the DHR model presented in [120] was employed.
This work is structured in five sections. In Section 5.3, the filtered LES equations, the combustion model DHR as well as the radiation modeling methodology are presented. In Section 5.4, DF-NORA is presented in more details along with the NORA and LM approaches. In Section 5.5, DF-NORA is validated on a non-premixed partially diluted configuration, Flame D. As widely explained in [120], although this flame does not meet the criteria of FC, the well documented experimental data is appropriate for modeling validation. Secondly, although dilution is not included in DF-NORA, the partial dilution of the fresh gases is a characteristic in common with FC from a combustion point of view. In Section 5.6, DF-NORA is employed to model NO formation in the flameless test case of Verissimo et al. [14]. Finally, in Section 5.7, the main conclusions and perspective from this work are outlined.

5.3 The DF-NORA pollutants model

5.3.1 The filtered LES equations

The reactive Navier-Stokes equations considered are those already described in Sec. 4.3.1 apart for Eq. 4.2, for which a source term $\tilde{S}_r$ is added:

$$\frac{\partial \bar{\rho}\tilde{E}}{\partial t} + \nabla \cdot \left((\bar{\rho}\tilde{E} + \bar{P})\tilde{u}\right) = -\nabla \cdot \left[-\overline{u\tau} + \bar{q} + \bar{q}^t\right] + \bar{\rho}\widetilde{\omega}_T + \tilde{S}_r + \bar{Q}_w \tag{5.4}$$

As already explained in the previous Chapter, $\widetilde{\omega}_k$ represents the species chemical reaction rate in the species equation 4.3. In this new section, two closures of $\widetilde{\omega}_k$ are considered depending on the species. For species that do not contain nitrogen atoms and species N_2, which we will note Y_m in the following, the DHR combustion model of Chapter 4 is used. The remaining species, which are noted Y_n, are directly involved in the NO_x chemistry. Although only the NO species is transported in the LES code, all the nitrogen species Y_n are included in the complex chemistry mechanism (GRI 2.11 [128] for these calculations) used to tabulate NO. This means that all the production as well as all consumption paths included in this mechanism are considered in the NO reaction rate: thermal or extended Zeldovitch pathway, prompt, N_2O, NNH and reburning pathways. These species play a minor role in fuel oxidation and their evolution is essentially decoupled from the fuel oxidation chemistry as shown in [111]. As a consequence, their reaction rates $\widetilde{\omega}_n$ are modeled with specific NO_x models, presented in Section 5.4.

Once the filtered equations for $\tilde{Z}$ (Eq. 4.4) and its variance (Eq. 4.5) are described, a scalar dissipation rate at stoichiometry can be calculated. This variable will be then used as an input for the models presented in Section 5.4. The filtered scalar dissipation rate is modeled as the sum of a resolved part χ_{RES} and sub-grid one χ_{SGR}, using the following expression:

$$\tilde{\chi} = 2(\tilde{\chi}_{RES} + \tilde{\chi}_{SGS}) \tag{5.5}$$

where χ_{RES} is calculated as

$$\tilde{\chi}_{RES} = D(\nabla \tilde{Z})^2 \tag{5.6}$$

where D is the molecular diffusivity, whereas χ_{SGS} is calculated following the expression proposed by Pierce et al. [129]:

$$\tilde{\chi}_{SGS} = C_0 \frac{\nu_t}{\Delta x^2} v_Z \tag{5.7}$$

The scalar dissipation rate at any mixture fraction Z is then calculated using the expression proposed by Peters [101]:

$$\chi(Z) = aF(Z) \tag{5.8}$$

$$F(Z) = \frac{exp\left(-2[erf^{-1}(1-2Z)]^2\right)}{2\pi} \tag{5.9}$$

where a is the strain rate deduced from $\tilde{\chi}$ by averaging Eq. (5.9) over mixture fraction:

$$\tilde{\chi} = aI(\tilde{Z}, S_Z) \tag{5.10}$$

$$I(\tilde{Z}, S_Z) = \int_Z F(Z)P(Z, \tilde{Z}, S_Z)dZ \tag{5.11}$$

In the above expression, a $\beta - PDF$ is used to represent the PDF of Z. This PDF depends on $\tilde{Z}$ and the segregation factor S_Z defined by:

$$S_z = \frac{\tilde{Z}_v}{\tilde{Z}(1-\tilde{Z})} \tag{5.12}$$

Using the above equations allows to deduce the scalar dissipation at stoechiometry Z_{st} which will be used in the NO_x modelling:

$$\tilde{\chi}_{st} = \tilde{\chi}\frac{F(Z_{st})}{I(\tilde{Z}, S_Z)} \tag{5.13}$$

5.3.2 Coupling of DHR model with radiative heat transfer

In the results of Section 5.5, the influence of radiation is investigated on NO_x prediction in a partially premixed diffusion flame. The radiative source term in Eq. (5.4) results from the resolution of the Radiative Transfer Equation (RTE) in the burnt gas as an absorbing and non−scattering medium, its equation reads :

$$s \cdot \nabla L_\nu(x,u) = k_\nu \left[L_\nu^0(x) - L_\nu(x,u)\right] \tag{5.14}$$

where ν is the wavenumber, L_ν^0 is the Planck equilibrium function, L_ν is the radiation intensity for a coordinate x in the direction of propagation u and k_ν is the absorption coefficient.

The source term S_r to insert in Eq. (5.4), is retrieved from a double integration of Eq. (5.14) over the solid angle and on the gas spectra. From this integration, S_r looses its dependency from the direction u and the frequency ν and is only function of the spatial coordinate x:

$$S_r(x) = \int_0^\infty k_\nu \left[4\pi L_\nu^0(x) - \int_{4\pi} L_\nu(x,u)d\Omega\right] d\nu \tag{5.15}$$

The resolution of the RTE and this double integration can be executed in several ways which has a strong impact on the time calculation.

From the works of Poitou et al. [130, 131], the following models where used for the calculations of Section 5.5:

- The spatial and the angular discretization : the Discrete Ordinate Method (DOM) ([132], [133]) is used, which is a finite volume formulation approach for the RTE. This strategy was already used in LES calculations as it represents a good compromise between CPU time and quality of the results. The angular integration was performed by the PRISSMA[1] code on $N_{dir} = 24$ directions with the S4 quadrature.

[1] http://www.cerfacs.fr/prissma

- The integration over frequencies : theoretically, it would consist in integrating the RTE over the entire wavelength of absorbing gas such as CO_2, CO and H_2O. The gas absorbing spectra contains several millions of lines and requires a spectral model. For the results of Section 5.5, the global and more common model WSGG [134] was here employed and presented a good compromise between accuracy and CPU time.
- LES filtering : following the work of Poitou et al. [130] and Roger et al. [135, 136] no subgrid scale model is used to performed radiative calculations in LES context such as $\overline{S_r(T;X_k)} \approx \widetilde{S_r}(\widetilde{T};\widetilde{X_k})$

The resolution of one iteration of the RTE is relatively time consuming due the double integration over direction and frequencies. For one time step, it lead to more important CPU time for the radiative solver than LES solver. A coupling strategy must be used to reach acceptable calculation times: the two codes are run simultaneously and in a synchronized way; furthermore the radiative iteration is performed only every N_{it} iterations of the CFD solver, corresponding to the characteristic convective time. This coupling strategy was already successfully used in [130] and [131], where the radiative code PRISSMA and the LES solver AVBP were coupled by means of a bridge, called o-PALM[2]. The same strategy was used for the results in Section 5.5.

5.4 NO models

In this study, three NO models are considered. The first one is the tabulated NORA model [111, 127] which considers the relaxation of NO towards equilibrium in a homogeneous reactor. The second approach is the linear model (LM) as proposed by Ihme and Pitsch [112]. In this model the effect of strain on the NO reaction rate is accounted for, based on equilibrium diffusion flames. The third approach is an improvement of the LM introducing the non linearity of the NO reaction rate as proposed by [119].

5.4.1 The NORA model

In the NORA model [111], the NO reaction rate is defined considering a homogeneous reactor at equilibrium, identified by its mixture fraction Z and enthalpy H. The choice of the equilibrium state implies that NORA is not able to account for NO paths related to the flame structure like the prompt NO. In this paper, only species NO is considered, although an extension to NO_2 and N_2O was proposed in [127]. If a perturbation of the NO mass fraction $\Delta Y_{NO}(t=0) = Y_{NO}(t=0) - Y_{NO}^{eq}(Z,H)$ is initially imposed in the reactor, an exponential relaxation of $Y_{NO}(t)$ is observed towards the equilibrium value $Y_{NO}^{eq}(Z,H)$. It was also observed that the complex chemistry NO reaction rate $\dot{\omega}_{NO}^{CC}$ during this relaxation lies on a one-dimensional manifold defined by solely by Z, H and $|\Delta Y_{NO}(t)|$. Instead of tabulating directly $\dot{\omega}_{NO}^{CC}$, a linear form is used in the CFD code:

$$\dot{\omega}_{NO} = \frac{Y_{NO}^{eq}(Z,H) - Y_{NO}}{\tau_{NO}(Z,H,|\Delta Y_{NO}|)} \tag{5.16}$$

where the relaxation time τ_{NO} is deduced from the complex chemistry homogeneous reactor calculations as $\tau_{NO} = \frac{Y_{NO}^{eq}(Z,H) - Y_{NO}(t)}{\dot{\omega}_{NO}^{CC}(t)}$. In practice, the variation of τ_{NO} with $|\Delta Y_{NO}|$ is smooth, therefore, only four values of τ_{NO} are tabulated for given values of Z and H.

In order to express the NORA reaction rate in a way similar to that of the LM and DF-NORA models presented in the following subsections, we introduce a normalized NO progress

[2]http://www.cerfacs.fr/globc/PALM_WEB/

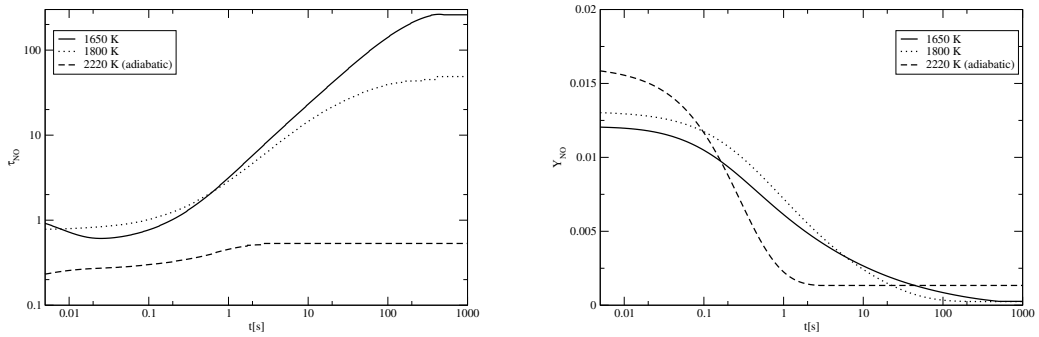

(a) (b)

Figure 5.1 – *NO relaxation towards equilibrium in a homogeneous reactor at Z_{st} for various enthalpy levels corresponding to temperatures (1650, 1800 and 2220 K) as used to generate the NORA table. A methane/air mixture is considered at ambient pressure. Fig.5.1(a): NO mass fraction as a function of time; Fig.5.1(b): NO relaxation time as a function of time.*

variable c_{NO} in place of the perturbation ΔY_{NO}:

$$c_{NO} = \frac{Y_{NO}}{Y_{NO}^{eq}(Z,H)} = 1 - \frac{\Delta Y_{NO}}{Y_{NO}^{eq}} \tag{5.17}$$

Besides, the NO reaction rate can be expressed as the sum of a positive and a negative contribution, which leads to :

$$\dot{\omega}_{NO}(Z,H,c_{NO}) = \dot{\omega}_{NO}^{+} + \dot{\omega}_{NO}^{-} \tag{5.18}$$

$$\dot{\omega}_{NO}^{+}(Z,H,c_{NO}) = \frac{Y_{NO}^{eq}(Z,H)}{\tau_{NO}(Z,H,c_{NO})} \tag{5.19}$$

$$\dot{\omega}_{NO}^{-}(Z,H,c_{NO}) = -\frac{Y_{NO}}{\tau_{NO}(Z,H,c_{NO})} \tag{5.20}$$

The NO relaxation in a homogeneous reactor at stoichiometry for methane ($Z_{st} = 0.055$) at $p = 1$ bar is shown in Fig. 5.1 using the GRI−MECH 2.11 mechanism [128]. In Fig. 5.1(a), NO trajectories are presented for an initial perturbation $\Delta Y_{NO} = 0.015$ and three enthalpy levels corresponding to equilibrium temperatures of 1600, 1800 and 2200 K respectively. The corresponding relaxation times are shown for each trajectory in Fig. 5.1(b). The relaxation towards equilibrium is clearly observed in each case. As temperature decreases, the relaxation time τ_{NO} increases exponentially while the equilibrium value Y_{NO}^{eq} decreases exponentially, illustrating the high sensitivity of thermal NO to temperature. Furthermore, as the trajectories come closer to their equilibrium values, the relaxation slows down and the relaxation times have the tendency to increase.

5.4.2 The linear model

In the LM proposed in [112], the NO reaction rate is also expressed as a linear relaxation like in Eq. (5.16). But this time, stretching effects on the NO reaction rate is accounted for by considering equilibrium diffusion flames instead of homogeneous reactors. The NO reaction rate is defined by its mixture fraction Z, the total enthalpy H and by the stoichiometric scalar dissipation rate χ_{st}.

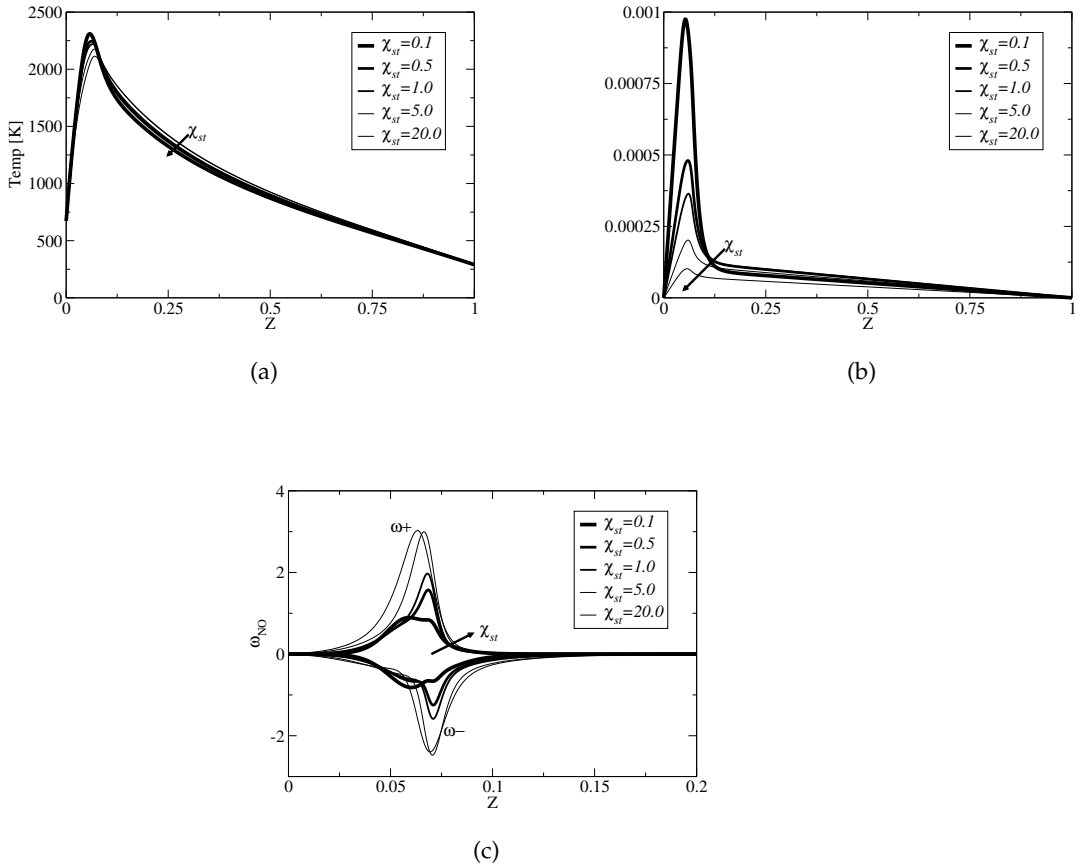

Figure 5.2 – *Equilibrium flamelet profiles for five values of χ_{st}. Fig.5.2(a): temperature versus mixture fraction; Fig.5.2(b): NO mass fraction versus mixture fraction; Fig.5.2(c): positive and negative contributions of the NO reaction rate.*

The NO reaction rate $\dot{\omega}_{NO}$ is divided into a productive part $\dot{\omega}_{eq}^{+}$ and destructive part $\dot{\omega}_{eq}^{-}$. Fig. 5.2 depicts the temperature, NO mass fraction Y_{NO} and reaction rates of five flamelets as a function of χ_{st}. The boundary conditions for these flamelets are the same as those of the Verissimo burner ($T_F = 298$ K for $Z = 1$ and $T_A = 673$ K for $Z = 0$) studied in Section 5.6. The GRI−MECH 2.11 mechanism [128] is employed and the FLAMEMASTER flamelet code [137] is used to run the calculations. It can be seen that as scalar dissipation increases, the NO level decreases as a consequence of the increased NO diffusion and decreased temperature. But at the same time, $\dot{\omega}_{NO}$ increases, showing that the net NO production rate increases with scalar dissipation. In order to account for the enthalpy variation at a given Z, additional flamelets are calculated using the FLAMEMASTER radiation model.

Fig. 5.3 shows a flamelet at equilibrium and $\chi_{st} = 0.01$ at different radiation times τ_{rad}. As τ_{rad} increases, $H(Z)$ decreases from its adiabatic value down to its minimum value obtained at $\tau_{rad} = \infty$. Radiation affects temperature, decreasing the peak of temperature around stoichiometry. Enthalpy lowers down as well. As temperature decreases, NO also decreases. This also influences the destructive and productive parts of $\dot{\omega}_{NO}$ which reduce with τ_{rad}. For this type of flamelets, Ihme and Pitsch showed that $\dot{\omega}_{NO}$ can be modeled as:

$$\dot{\omega}_{NO} = \dot{\omega}_{eq}^{+}(Z, H, \chi_{st}) + c_{NO}\dot{\omega}_{eq}^{-}(Z, H, \chi_{st}) \tag{5.21}$$

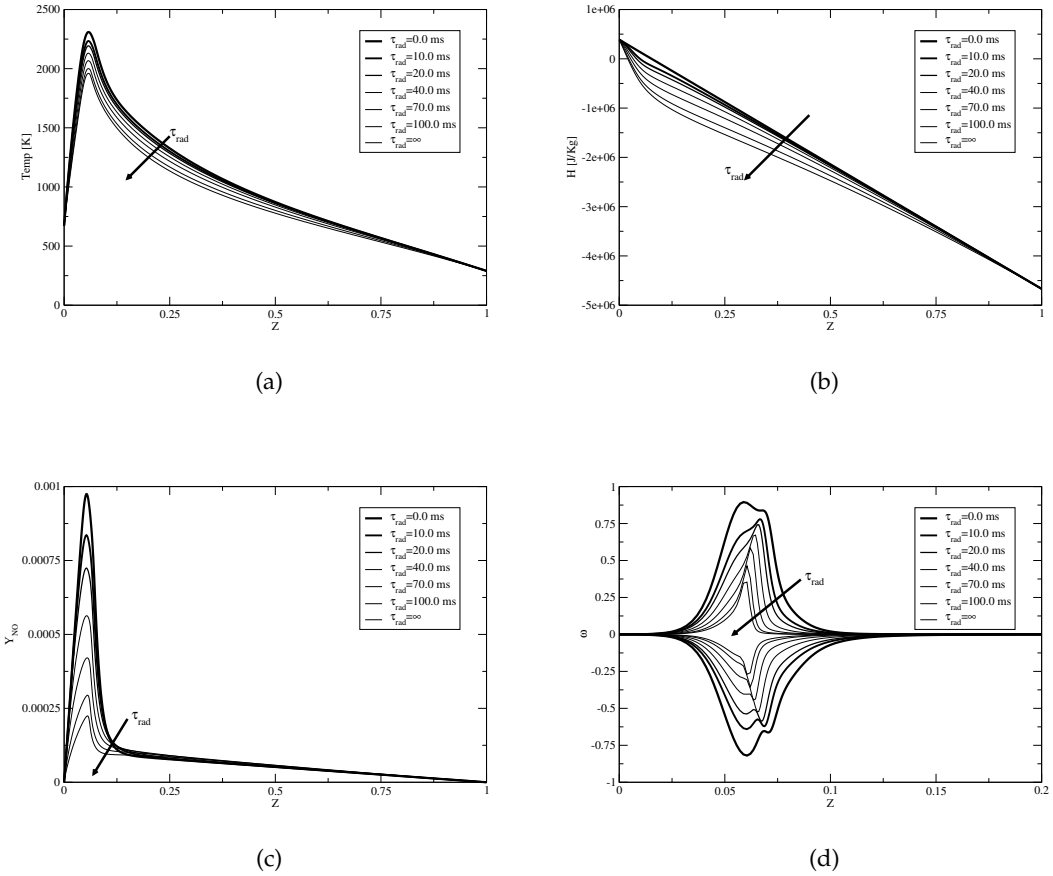

Figure 5.3 – *Equilibrium flamelets as a function of the radiative time τ_{rad}. Fig.5.3(a): temperature versus mixture fraction; Fig.5.3(b): enthalpy versus mixture fraction; Fig.5.3(c): NO mass fraction versus mixture fraction; Fig.5.3(d): positive and negative contributions of NO reaction rate versus mixture fraction;*

where the normalized NO mass fraction c_{NO} is defined by:

$$c_{NO} = \frac{Y_{NO}}{Y_{NO}^{eq}(Z, H, \chi_{st})} \tag{5.22}$$

where $Y_{NO}^{eq}(Z, H, \chi_{st})$ is the equilibrium NO mass fraction of the steady state flamelet. This model was applied to Flame D by the same authors and lead to a sensible overestimation of NO. Zoller et al.[119] argued that this overestimation is due to the linear approximation in the NO reaction rate model: the terms $\dot{\omega}_{eq}^{+}$ and $\dot{\omega}_{eq}^{-}$ are considered at $Y_{NO} = Y_{NO}^{eq}$, that is, they are assumed independent of Y_{NO}. As shown by Zoller et al. , this approximation is not sufficient when NO is far from equilibrium.

5.4.3 The DF-NORA model

NO reaction rate calculation

In order to account for the non linearity of $\dot{\omega}_{NO}$, Zoller et al. [119] tabulated $\dot{\omega}_{NO}$ as a function of the NO mass fraction using homogeneous reactors. These calculations were performed by

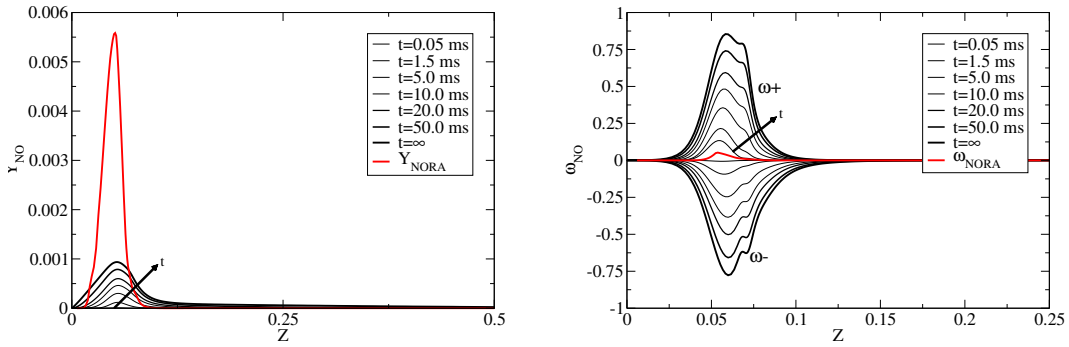

(a) (b)

Figure 5.4 – *NO temporal evolution during an unsteady flamelet calculation at $\chi_{st} = 0.1\ s^{-1}$ as used to generate DF-NORA table. Fig.5.4(a): NO mass fraction versus mixture fraction (black); equilibrium NO mass fraction from NORA table (red). Fig.5.4(b): positive and negative contributions of $\dot{\omega}_{NO}$ versus mixture fraction (black); NO reaction rate from the NORA table at $c_{NO} = 0$ (red).*

imposing the mass fraction of all species that contain no nitrogen atoms to their value obtained on a laminar diffusion flame. Only the nitrogen containing species were allowed to evolve, starting the simulations with $Y_{NO}(Z,t) = 0$.

In the present work, a similar approach called DF-NORA is retained but using an unsteady flamelet calculation to tabulate $\dot{\omega}_{NO}$. The procedure to obtain the NO reaction consists in two steps.

In a first step, a set of flamelets at equilibrium is built as a function of χ_{st} and Z. Two types of flamelets are used: the adiabatic flamelet corresponding to $H_{max}(Z)$ or $\tau_{rad} = 0$ and the flamelet at $\tau_{rad} = \infty$ corresponding to $H^{DF}_{min}(Z)$. Note that $H^{DF}_{min}(Z)$ is not necessarily equal to $H_{min}(Z)$ used in the DHR model. For this set of flamelet calculations the entire NO mechanism is deactivated, yielding zero reaction rates for all species Y_n.

In a second step, for each steady flamelet solution, the NO mechanism is activated at time $t = 0$ to let all species evolve towards equilibrium. This relaxation of the flamelet towards its new equilibrium is computed in time with the FLAMEMASTER code. The temporal evolutions of NO, $\dot{\omega}^+$ and $\dot{\omega}^-$ are shown in Fig. 5.4 for the same conditions as in the previous figure using $\tau_{rad} = 0$ and $\chi_{st} = 0.1$. It can first be observed that the growth of NO is strictly monotonic, therefore allowing the tabulation of $\dot{\omega}_{NO}$ as a function of c_{NO}. Besides, it can be seen that $\dot{\omega}^+$ and $\dot{\omega}^-$ evolve in time in a way which seems proportional to Y_{NO}. This behavior is reproduced by the LM for the negative term $\dot{\omega}^-_{eq}\frac{Y_{NO}}{Y^{eq}_{NO}}$ in Eq. (5.21). On the contrary $\dot{\omega}^+$ is assumed constant and equal to $\dot{\omega}^+_{eq}$ in the LM, which is not in agreement with the observations of Fig. 5.4. This explains why the LM overpredicts the NO reaction rate far from equilibrium, that is, when $Y_{NO} << Y^{eq}_{NO}$.

Unlike in the approach proposed by Zoller, the complete mechanism is solved during the second step therefore also the other species Y_m can evolve during this relaxation. To measure the perturbation induced by the introduction of the NO mechanism in the unsteady calculation of the second step, Fig. 5.5 presents the relative variation ϵ_Ψ defined as:

$$\epsilon_\Psi = \frac{\Psi^{wno} - \Psi^{wono}}{\Psi^{wono}} \tag{5.23}$$

Ψ^{wono} represents any flamelet quantity Ψ obtained from the steady flamelet calculation performed without NO_x reactions in step one. Ψ^{wno} represents the same quantity obtained at the

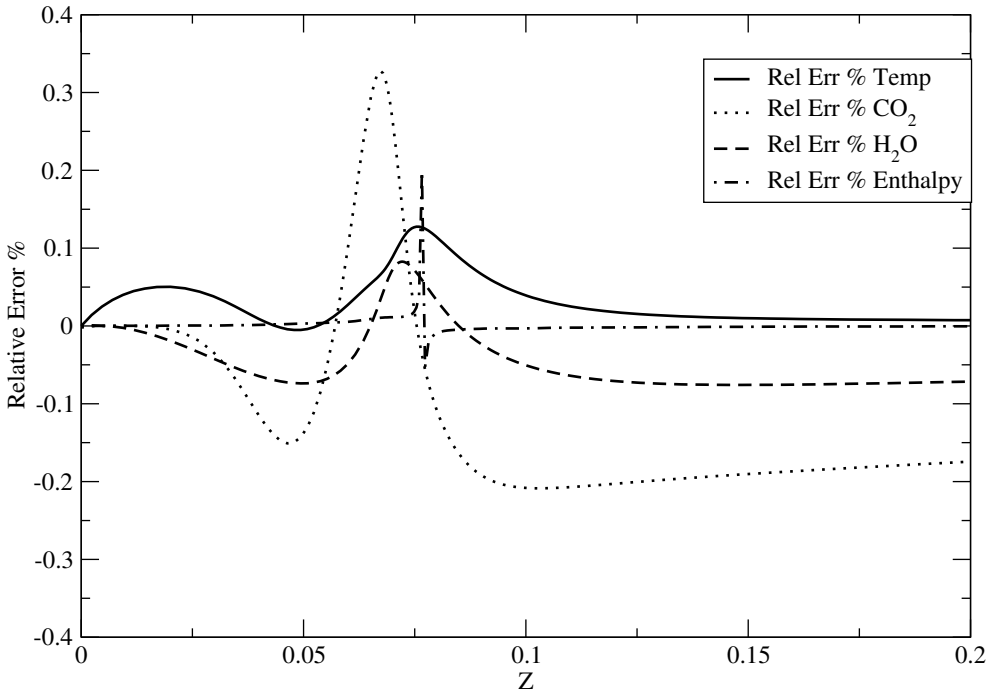

Figure 5.5 – *Relative variation ϵ_Ψ (see Eq. 5.23) of temperature, CO_2, H_2O and enthalpy, between the equilibrium flamelet with and without the NO mechanism.*

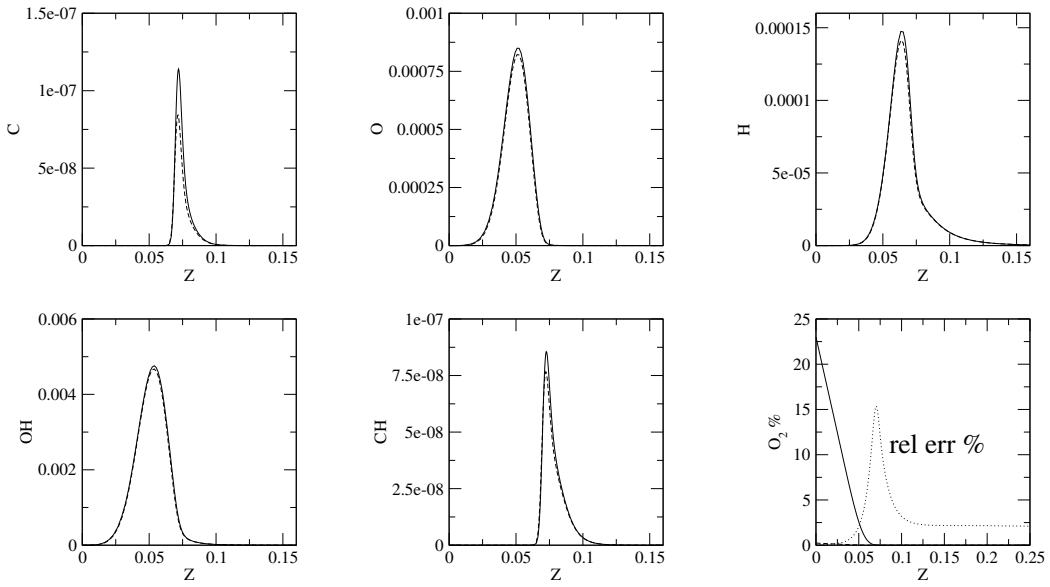

Figure 5.6 – *O, H, OH and O_2 mass fraction profiles in flamelets at $\chi_{st} = 0.1$. Dashed line: complete mechanism activated. Solid lines: NO mechanism deactivated.*

end of the unsteady flamelet calculation performed with the complete mechanism in step two. It can be noticed that for major species such as CO_2 and H_2O or for temperature and enthalpy, the relative difference remains always smaller than 0.4%. This confirms that the introduction of the NO reactions does not alter the major characteristics of the flamelet. Major differences are noticed on the contrary for radical species such as O which form the pool from which nitrogen containing species are formed. Fig.5.6 presents radicals C, O, H, OH, CH and O_2 profiles versus mixture fraction for the steady state solutions obtained with and without the NO mechanism. O_2 is affected by the formation of NO essentially on the rich side showing a 15% difference around $Z = 0.07$. This can be explained by the fact that the oxygen contained in species Y_n is essentially provided by O_2. These results show that assuming like in the model of Zoller that Y_m is constant during the relaxation of NO, is acceptable for major species but not for some minor species or for O_2. This assumption could consequently lead to possible deviations on the calculation of the NO reaction rate.

Finally, the NO reaction rates $\dot{\omega}^+$ and $\dot{\omega}^-$ are tabulated using an interpolation between the two flamelet calculations at $\tau_{rad} = 0$ and $\tau_{rad} = \infty$:

$$\begin{aligned} \dot{\omega}^{+/-}(Z, H, \chi_{st}, c_{NO}) \\ = c_H^{DF} \dot{\omega}^{+/-}(Z, H_{max}^{DF}, \chi_{st}, c_{NO}) \\ +(1 - c_H^{DF}) \dot{\omega}^{+/-}(Z, H_{min}^{DF}, \chi_{st}, c_{NO}) \end{aligned} \tag{5.24}$$

where c_H^{DF} is defined as:

$$c_H^{DF} = \frac{H - H_{min}^{DF}}{H_{max}^{DF} - H_{min}^{DF}} \tag{5.25}$$

In the case $c_{NO} \leq 1$, $\dot{\omega}^{+/-}$ is directly extracted from the unsteady flamelet calculations. In the case $c_{NO} > 1$ an approximation of the reaction rate is proposed in Section 5.4.3.

Table 5.1 summarizes the expressions used to compute the DF-NORA NO reaction rate depending on the value of χ_{st} and c_{NO}:

Table 5.1 – *Conditions of ignition*

	$\chi_{st} = 0$	$\chi_{st} \geq \chi_{st}^{min}$
$c_{NO} \leq 1$	Eq. (5.18)	unsteady flamelet computation
$c_{NO} > 1$	Eq. (5.18)	Eq. (5.28)

Comparison with LM and NORA models

In order to assess the difference between the LM and DF-NORA, Fig. 5.7 presents the ratios γ^+ and γ^- defined as:

$$\gamma^+ = \frac{\dot{\omega}^+}{\dot{\omega}_{eq}^+} \tag{5.26}$$

$$\gamma^- = \frac{\dot{\omega}^-}{\dot{\omega}_{eq}^- \frac{Y_{NO}}{Y_{NO}^{eq}}} \tag{5.27}$$

for three mixture fractions ($Z = 0.03$, $Z = Z_{st} = 0.055$ and $Z = 0.1$) and for the two enthalpy levels, as a function of c_{NO}. It can first be observed that in all cases γ^- remains very close to unity, confirming that the LM correctly represents the negative contribution of the reaction rate. On the contrary, γ^+ is nearly linear with c_{NO} starting with very small values at $c_{NO} = 0$ corresponding to 3%-8% of the equilibrium value, and ending at unity at $c_{NO} = 1$. This result confirms that the positive contribution γ^+ can not be approximated by $\dot{\omega}_{eq}^+$ and needs to be tabulated as a function of c_{NO}.

Fig. 5.4(a) presents Y_{NO}^{eq} used in the NORA model, which corresponds to $\chi_{st} = 0$, for the same enthalpy H and mixture fraction Z. It can be observed that due to the absence of diffusion in mixture fraction space, this equilibrium value is much larger than the one at $\chi_{st} = 0.1\,s^{-1}$ and it is also restricted to a narrower region around stoechiometry. Fig. 5.4(b) presents $\dot{\omega}_{NO}$ for NORA at $c_{NO} = 0$ corresponding to Eq. (5.19). Although the equilibrium NO mass fraction is larger for NORA, the reaction rate is smaller by at least a factor of two compared to DF-NORA. This difference is due to the fact that in NORA the NO reaction rate calculation is based on the equilibrium burnt gases state corresponding to a progress of reaction $c = 1$ (see Eq. 4.28). As shown by Nishioka [138] for premixed flames, the NO reactivity in the burnt gases of the flame, corresponding to $c = 1$, is essentially due to the thermal mechanism. On the contrary, in the diffusion flame used in DF-NORA, c remains lower than unity, leading to a predominance of the prompt mechanism as evidenced by Ihme and Pitsch [112] . This difference of reactivity between NORA and flamelet based NO models is clearly evidenced in the results Sections 5.5 and 5.6.

Reaction rate modelling for the case $c_{NO} > 1$

The unsteady flamelets used to tabulate the NO reaction rate in DF-NORA allow to cover the range $c_{NO} \in [0, 1]$. In practical devices, as shown in [111] for Diesel engines, c_{NO} can assume values larger than unity. In order to model $\dot{\omega}_{NO}$ for $c_{NO} > 1$, an unsteady flamelet calculation was performed with the following initial condition: $Y_{NO}(t = 0) = 2Y_{NO}^{eq}$. As expected, it was also observed in this case that Y_{NO} relaxes towards its equilibrium value Y_{NO}^{eq} exactly like when starting the flamelet calculation with $Y_{NO}(t = 0) = 0$. Fig. 5.7(b) presents (red curves) the coefficients γ^+ and γ^- for this case. It shows that γ^- remains close to unity, meaning that the LM model for the negative contribution, Eq. (5.21), remains a good approximation also for

$c_{NO} > 1$. It is therefore adopted for DF-NORA in this case. On the contrary, γ^+ shows the same linear increase as in the case $c_{NO} \leq 1$. For this reason, the positive contribution for $c_{NO} > 1$ is modeled by extrapolating the result obtained for $c_{NO} \leq 1$, which leads to the expression:

$$\dot{\omega}^+(Z, H, \chi_{st}, c_{NO}) = \dot{\omega}^+_{eq}(Z, H, \chi_{st}, c_{NO} = 1) + c_{NO} \frac{\partial \dot{\omega}^+}{\partial c_{NO}}(Z, H, \chi_{st}, c_{NO} = 1) \tag{5.28}$$

Note that for the validations presented in this paper, Y_{NO} remains always much smaller than its equilibrium value, therefore the modeling of the NO reaction rate for $c_{NO} > 1$ proposed here could not be evaluated yet.

Reaction rate modeling for the case $\chi_{st} < \chi_{st}^{min}$

The flamelet NO reaction rate can be defined solely for $\chi_{st} > \chi_{st}^{min}$ where χ_{st}^{min} is the minimum scalar dissipation rate that can be used in the flamelet code to run the simulation in an acceptable CPU time. The χ_{st}^{min} value depends on the boundary conditions of the flamelet used to build the table. In a real burner, or in the two flames investigated in this paper, very low strain regions satisfying $\chi_{st} < \chi_{st}^{min}$ can be found. The values of χ_{st}^{min} are reported in Sections 5.5 and 5.6. In these regions using χ_{st}^{min} might lead to an overestimation of the NO production rate. For this reason, we propose to include in DF-NORA the NORA table corresponding to $\chi_{st} = 0$. As shown in Section 5.4.1, the NORA reaction rate Eq. (5.18) can be cast in a positive and negative contribution like the flamelet reaction rate. This allows to express the final NO reaction rate as $\dot{\omega}^+(Z, H, \chi_{st}, c_{NO})$ whatever the value of χ_{st}.

For $0 < \chi_{st} < \chi_{st}^{min}$, an interpolation is performed between the reaction rate obtained at $\chi_{st} = 0$ and $\chi_{st} = \chi_{st}^{min}$.

5.4.4 Filtering of the NO models

Filtered reaction rate

The NO reaction rate needs to be filtered at the cell level. For this purpose, a filtered NO progress variable is defined as:

$$\tilde{c}_{NO} = \frac{\tilde{Y}_{NO}}{\tilde{Y}^{eq}_{NO}(\tilde{Z}, S_z, \tilde{c}^*_H, \tilde{\chi}_{st})} \tag{5.29}$$

where $\tilde{Y}_{NO}$ is given by the NO transport equation and the filtered equilibrium NO mass fraction $\tilde{Y}^{eq}_{NO}$ is defined as:

$$\tilde{Y}^{eq}_{NO} = \int_0^1 Y^{eq}_{NO}(Z, H, \chi_{st}) P(Z, H, \chi_{st}) dZ \tag{5.30}$$

In Eq. (5.29), $\tilde{c}^*_H$, given by Eq. (5.42), represents the mean normalized enthalpy used for the NO models. Its expression is given in the next Section for clarity's sake.

Like in the DHR model, we assume that the fluctuations of H for a given mixture fraction Z can be neglected. This allows to express H in the integral as a function of Z using Eq. (4.43) and $\tilde{c}^*_H$. In the same way, we neglect the fluctuations of χ_{st} allowing to write $\chi_{st} = \tilde{\chi}_{st}$ in the integral. $\tilde{Y}^{eq}_{NO}$ is thus defined as:

$$\tilde{Y}^{eq}_{NO}(\tilde{Z}, S_z, \tilde{c}^*_H, \tilde{\chi}_{st}) = \int_0^1 Y^{eq}_{NO}(Z, H(Z), \tilde{\chi}_{st}) P(Z) dZ \tag{5.31}$$

where $P(Z)$ is the presumed PDF of mixture fraction as defined in Section 4.3.1. In this equation $\tilde{Z}$ is retrieved from its transport equation Eq. (4.4) while S_Z is given by. Eq. (5.12). The

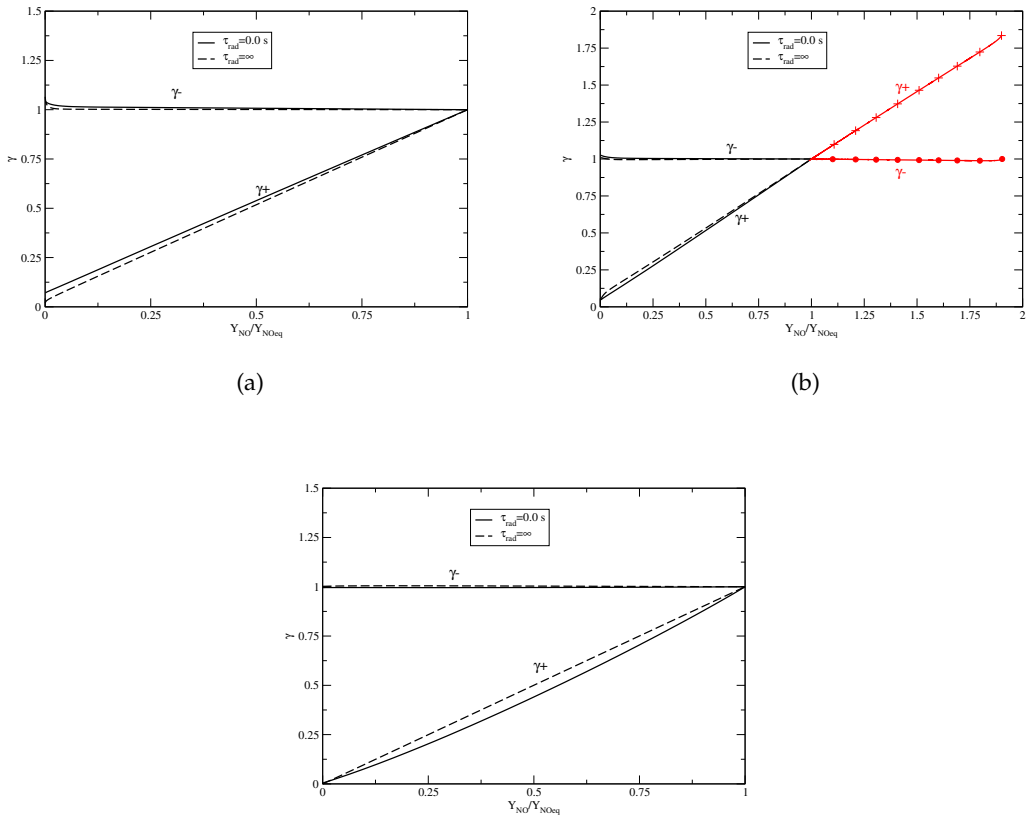

Figure 5.7 – *Evolution of γ^+ and γ^- versus c_{NO} calculated for a flamelet at $\chi_{st} = 0.1\ s^{-1}$ using Verissimo boundary conditions. Cases $\tau_{rad} = 0.0$ ms (solid lines) and $\tau_{rad} = \infty$ (dashed lines). Fig. 5.7(a): $Z = 0.03$; Fig. 5.7(b): $Z = Z_{st}$. Fig. 5.7(c): $Z = 0.1$. Black curves: calculation starting at $c_{NO} = 0$, red curves (Fig. 5.7(b) only): calculation starting at $c_{NO} = 2$.*

filtered stoechiometric scalar dissipation rate $\tilde{\chi}_{st}$ is given by Eq. (5.13). Note that if $\tilde{\chi}_{st} \geq \chi_{st}^{min}$, Y_{NO}^{eq} corresponds to steady state NO mass fraction of the laminar flamelet at $\tilde{\chi}_{st}$ and enthalpy $H(Z)$. If $\tilde{\chi}_{st} < \chi_{st}^{min}$, Y_{NO}^{eq} is interpolated between the chemical equilibrium NO mass fraction used in NORA and the flamelet value at χ_{st}^{min}, as done for the NO reaction rate.

The filtered NO reaction rates are computed for the three models neglecting the fluctuations of H, χ_{st} and c_{NO}. For the NORA model, this allows to write $Y_{NO}(Z) = \tilde{c}_{NO} Y_{NO}^{eq}(Z, H(Z))$, which is then used to filter the positive and negative reaction rates Eq. (5.19) and (5.20):

$$\tilde{\omega}_{NO}^{+}(\tilde{Z}, S_z, \tilde{c}_H^*) = \int_0^1 \frac{Y_{NO}^{eq}(Z, H(Z))}{\tau_{NO}(Z, H(Z), \tilde{c}_{NO})} P(Z) dZ \tag{5.32}$$

$$\tilde{\omega}_{NO}^{-}(\tilde{Z}, S_z, \tilde{c}_H^*, \tilde{c}_{NO}) = -\int_0^1 \frac{Y_{NO}}{\tau_{NO}(Z, H(Z), \tilde{c}_{NO})} P(Z) dZ \tag{5.33}$$

$$= -\tilde{c}_{NO} \tilde{\omega}_{NO}^{+}(\tilde{Z}, S_z, \tilde{c}_H^*, \tilde{c}_{NO}) \tag{5.34}$$

For the LM, the filtering proposed in [112] is retained, based on the same assumptions:

$$\tilde{\omega}_{NO}^{+}(\tilde{Z}, S_z, \tilde{c}_H^*, \tilde{\chi}_{st}) = \int_0^1 \omega_{eq}^{+}(Z, H(Z), \tilde{\chi}_{st}) P(Z) dZ \tag{5.35}$$

$$\tilde{\omega}_{NO}^{-}(\tilde{Z}, S_z, \tilde{c}_H^*, \tilde{\chi}_{st}, \tilde{c}_{NO}) = \tilde{c}_{NO} \int_0^1 \omega_{eq}^{-}(Z, H(Z), \tilde{\chi}_{st}) P(Z) dZ \tag{5.36}$$

For DF-NORA, two cases need to be considered. If $\tilde{c}_{NO} > 1$, we also have $c_{NO} = \tilde{c}_{NO} > 1 \quad \forall Z$. As seen previously, in this case the negative NO reaction rate is modeled as in the LM, therefore Eq. (5.36) is used, while the filtering of Eq. (5.28) leads to:

$$\tilde{\omega}_{NO}^{+}(\tilde{Z}, S_z, \tilde{c}_H^*, \tilde{\chi}_{st}) = \tilde{\omega}_{eq}^{+} + \tilde{c}_{NO} \int_0^1 \frac{\partial \omega^{+}}{\partial c_{NO}}(Z, H(Z), \tilde{\chi}_{st}, c_{NO} = 1) P(Z) dZ \tag{5.37}$$

For $\tilde{c}_{NO} < 1$, Eq. (5.24) is directly filtered yielding:

$$\tilde{\omega}^{+/-}(\tilde{Z}, S_z, \tilde{c}_H, \tilde{\chi}_{st}, \tilde{c}_{NO}) = \int_0^1 \omega^{+/-}(Z, H(Z), \tilde{\chi}_{st}, \tilde{c}_{NO}) P(Z) dZ \tag{5.38}$$

For all flamelet based reaction rates Eq. (5.35), (5.36), (5.37) and (5.38), the reaction rate in the integral is evaluated at enthalpy $H(Z)$. As only two flamelet solutions (adiabatic and non-adiabatic) are tabulated, the reaction rate at $H(Z)$ is interpolated between these two solutions according to Eq. (5.24). In this equation $c_H^{DF}(Z)$ is given by Eq. (5.25) where H is defined by Eq. (4.43).

Effective enthalpy $\tilde{c}_H^*$ for the NO models

In the DHR combustion model, the gas mixture spans all compositions from the fresh gases state at $\tilde{c} = 0$ up to the equilibrium state at $\tilde{c} = 1$. On the other side, the NO models described above all assume gases at thermodynamical equilibrium (for NORA) or at the equilibrium state of a diffusion flame (for LM and DF-NORA). This means that these NO models allow to describe the NO reaction rate only at $\tilde{c} = 1$. A reaction rate modeling needs therefore to be proposed for $\tilde{c} < 1$.

For this purpose, we consider a reactive mixture at $0 < \tilde{c} < 1$ defined by its enthalpy $\tilde{H}$, its temperature $\tilde{T}$ and its composition $\tilde{Y}_i$. This mixture also corresponds to an equilibrium state at the same total enthalpy, defined by its temperature $\tilde{T}_{eq}$, and composition $\tilde{Y}_i^{eq}(\tilde{H})$. This allows to write:

$$\tilde{H} = h_s(\tilde{Y}_i, \tilde{T}) + h_0(\tilde{Y}_i) = h_s(\tilde{Y}_i^{eq}, \tilde{T}_{eq}) + h_0(\tilde{Y}_i^{eq}) \tag{5.39}$$

where $h_s(Y_i, T) = \sum_i Y_i h_s^i(T)$ is the sensible enthalpy of the mixture and $h_0(Y_i) = \sum_i Y_i h_0^i$ is the formation enthalpy of the mixture. As the NO models are based on an equilibrium state, we assume the above mixture at $\tilde{c}$ can be approximated by the equilibrium state at temperature $\tilde{T}$. This allows to define the effective enthalpy $\tilde{H}^*$ that is seen by the NO models, which satisfies the implicit equality:

$$\tilde{H}^* = h_s(\tilde{Y}_i^{eq}(\tilde{H}^*), \tilde{T}) + h_0(\tilde{Y}_i^{eq}(\tilde{H}^*)) \tag{5.40}$$

$\tilde{H}^*$ is finally obtained by an iterative method. In order to understand the link between $\tilde{H}^*$ and the progress of reaction $\tilde{c}$, an approximate expression of $\tilde{H}^*$ can be deduced from Eq. (5.40):

$$\tilde{H}^* = \tilde{H} + (1 - \tilde{c})\Delta h_0 \tag{5.41}$$

where Δh_0 is the enthalpy variation between burnt and fresh gases: $\Delta h_0 = h_0(\tilde{Y}_i^{eq}) - h_0(\tilde{Y}_i^{u})$. Eq. (5.41) shows that $\tilde{H}^* = \tilde{H}$ at $\tilde{c} = 1$, that is, when the burnt gases state is reached, the enthalpy does not need to be corrected, in coherence with the assumption of an equilibrium state in the NO models. For $\tilde{c} < 1$, $\tilde{H}^*$ decreases linearly with $\tilde{c}$, which reflects the nearly linear relation between $\tilde{T}$ and $\tilde{c}$.

$\tilde{H}^*$ allows to calculate the effective normalized enthalpy $\tilde{c}_H^*$ used as an input parameter in the filtered NO reaction rate expressions. Following the same derivation as for $\tilde{c}_H$ (see Eq. (4.44)), it reads:

$$\tilde{c}_H^* = \frac{\tilde{H}^* - \tilde{H}_{min}(\tilde{Z}, S_z)}{\tilde{H}_{max}(\tilde{Z}, S_z) - \tilde{H}_{min}(\tilde{Z}, S_z)} \tag{5.42}$$

5.5 Evaluation of the NO models on Flame D

5.5.1 Experimental and numerical setup of Flame D

The DF-NORA model is validated on Flame D already described in Sec.4.5 The numerical setup is the same, but for the radiation part, a coarser mesh with a cell size increased by a factor of two approximately is used, leading to 6 millions grid cells. It was verified that this coarsening did not impact the quality of the radiative calculation. With regard to the coupling, 24 processors were used for the PRISSMA solver and 240 for the AVBP code. The wall temperature was set equal to 300 K, corresponding to the fresh air temperature and to the temperature of the laboratory environment seen by the flame. Compared to the non-coupled simulation, computational times were increased by a factor of 1.5. The DHR table is the same as the one used in Chapter 4, excepted that four values of ΔH_d are considered instead of one in order to account for the non adiabaticity of the flame. The minimum value of ΔH_d corresponds to a ΔT_d of -120 K, which is well below the temperature variations observed in the simulation. With regard to the DF-NORA table, it is described in Table 5.2. The DF-NORA calculations were performed with the flamelet solver FLAMEMASTER whereas the NORA calculations were performed with the SENKIN homogeneous reactor of the CHEMKIN-II package [139]. Both calculations were performed with the GRI 2.11 mechanism [128]. It is underlined that the GRI 2.11 mechanism was only used for the NO modeling as the GRI 3.0 is known to be less predictive, yielding an excessive NO production [70]. In order to assess the influence of the under-adiabaticity on NO, adiabatic NO predictions were also acquired by setting $c_H^{DF} = 1$ in the models.

5.5.2 Combustion results

Before presenting the NO results, the results of the DHR model coupled with the radiation code are presented. The radial profiles of the mean and RMS of mixture fraction are presented in Fig. 5.8 for six measurement positions, from $x/D = 3$ to $x/D = 60$.

Table 5.2 – *Description of the DF-NORA table for the Flame D calculations of Section 5.5*

Quantity	Number of tabulated values	Minimal value	Maximal value
χ_{st}	9	5	200
Z	200	0	1
c_{NO}	100	0	1
S_z	20	0	1
c_H^{DF}	2	0	1 (adiabatic flamelet)

The mean mixture fraction is found in good agreement with experiment as observed in the adiabatic calculations [120]. Concerning the RMS of mixture fraction, it tends to be over-predicted, in particular at location $x/D = 45$. Compared to the adiabatic calculation, the prediction of the RMS is still largely improved by taking radiation into account. As explained by Coelho [140] in his review about the works on the turbulence radiation interaction (TRI), radiation acts as a dissipative mechanism which tends to smooth fluctuations. Mean and RMS velocity radial profiles are presented in Fig. 5.9. As for mixture fraction, velocity is predicted accurately, apart from some deviation for the RMS, still observed at $x/D = 45$. Finally, the mean radial profiles of temperature, presented in Fig. 5.10, show an overall good agreement with the experiment. An overestimation of temperature on the centerline can still be observed between $x/D = 15$ and $x/D = 30$. It was attributed in [120] to the absence of scalar dissipation modeling in DHR. Temperature is well predicted further downstream, a region where the scalar dissipation rapidly decreases. With regard to the effects of radiation on temperature, a maximum decrease of the order of 20 K is obtained in the simulations at $x/D = 75$. This order of magnitude for the temperature variation was also obtained in the simulations in [119] (private communication). Because of this small variation, the adiabatic temperature is not shown here. Although this decrease is small, it corresponds to a total radiative heat loss fraction of 5.3% of the total power of the flame, which is very close to the 5.1% experimental value [109].

5.5.3 NO_x results

The results for the NO mass fraction are presented for the three models on the jet axis in Fig. 5.11 and on radial profiles in Fig. 5.12. It can be first noticed that the NORA model performs poorly as it underestimates the experimental value by a factor of three approximately. By contrast, NORA gave very good results on Diesel engine calculations in [111, 127, 141]. This result can be explained as follows. In Flame D, the high temperature region (roughly defined as $T > 1500K$) corresponds to the heat release region limited to $x/D < 60$. In this region, the strain rate is high enough to promote the NO production rate (see Fig. 5.2(c)). As NORA does not account for the impact of the strain rate on the NO production rate, it underpredicts the NO formation in this region. Outside this heat release region, the high temperature jet is rapidly diluted with the ambient air coflow, leading to a freezing of NO reactions. By contrast, in a Diesel engine the injection duration is limited in time, which leads to a rapid decrease of the strain rate after the end of the injection, as shown in [141]. Also, unlike in Flame D, the Diesel jet mixes with high temperature air/diluent gases. As a consequence, and as shown in [111], the NO formation proceeds away form the spray region and after the end of the injection, in a large portion of the chamber characterized by a high temperature and a low strain rate. The fact that NORA could reproduce quite accurately the final NO yield over thirty engine operating conditions [141], certainly means that in Diesel engines NO is essentially formed outside the high strain rate region. On the other side, the LM over-predicts NO by a factor of two approximately, although the shape of the experimental NO profile is well reproduced. This

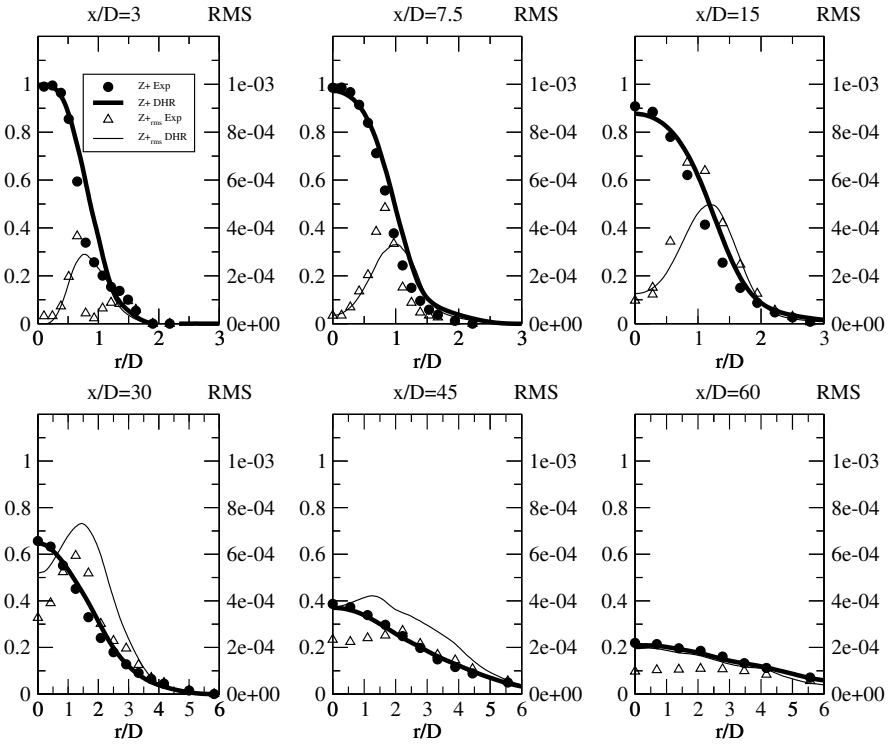

Figure 5.8 – *Mixture fraction radial profiles for Flame D. Experimental (symbols) and LES (solid line) mean mixture fraction. Experimental (triangles) and LES (dashed line) RMS mixture fraction.*

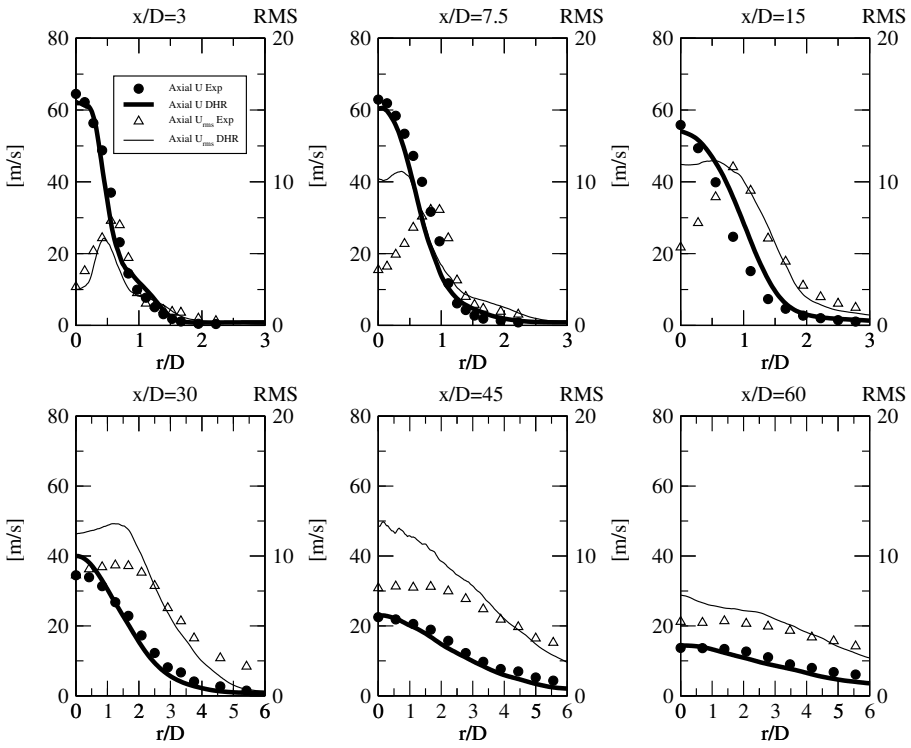

Figure 5.9 – *Axial velocity radial profiles for Flame D. Experimental (sympols) and LES (solid line) mean axial velocity. Experimental (triangles) and LES (dashed line) RMS axial velocity.*

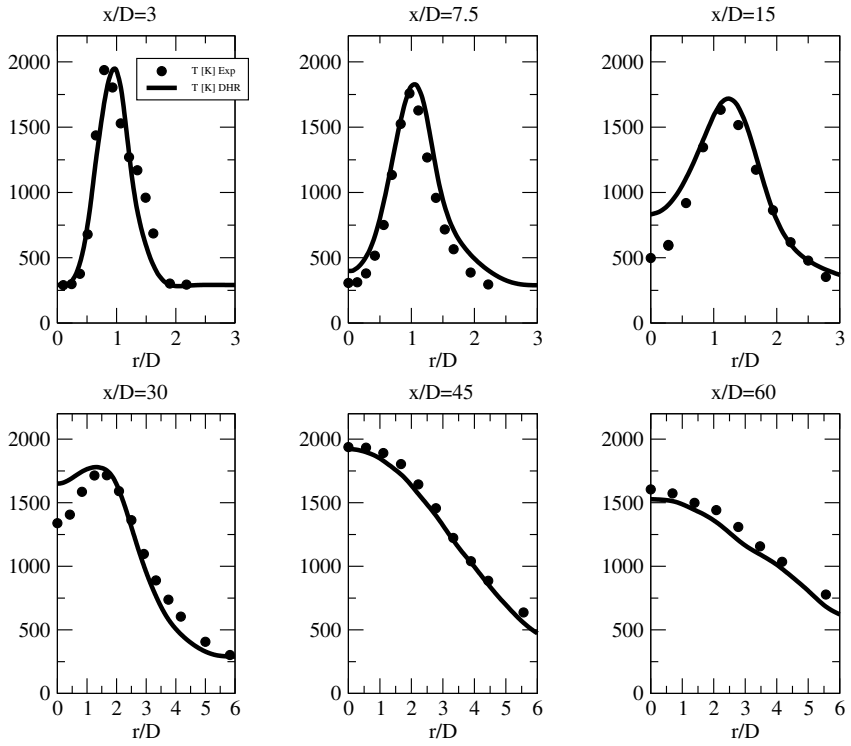

Figure 5.10 – *Mean experimental (symbols) and LES (solid line) temperature radial profiles for Flame D.*

result is coherent with the results of Ihme and Pitch [112] and Zoller et al. [119]. The DF-NORA model improves the NO prediction with respect to both previous models. The position of the NO peak value is correctly reproduced at $x/D \simeq 50$, as well as the final level at $x/D = 75$. At the same time, NO is under-predicted by 30% approximately in the region corresponding to $30 < x/D < 50$. No obvious explanation can be found for this under-prediction. Zoller et al. [119] did not observe such an under-prediction with their model which is also based on a non linear NO reaction rate tabulation and on the same GRI−MECH 2.11 mechanism. The first difference between DF-NORA and Zoller's model lies in the procedure used to tabulate the NO reaction rate: in DF-NORA the complete flamelet is solved in time while in Zoller et al., a homogeneous reactor calculation is performed in which all nitrogen-free species are frozen. As stressed by Zoller, this procedure does not allow to recover the equilibrium composition of the flamelet as diffusion in mixture fraction space is suppressed in these homogeneous reactor calculations. As a consequence, the unsteady flamelet calculations used in DF-NORA should be more accurate, especially when Y_{NO} approaches the equilibrium value. A second major difference is that in Zoller's model a transported PDF method is used to define the input parameters Z, χ_{st}, τ_{rad} and Y_{NO}, while in DF-NORA presumed PDF are used to evaluate these parameters (τ_{rad} being replaced by the total enthalpy H). As the former approach is more accurate, it can be hypothesized that it is this aspect of the model that makes the major difference in the results obtained with the two models. As temperature only decreases by a maximum of 20 K in the non-adiabatic calculation compared to the adiabatic one, the NO mass fraction only decreases by a maximum of 6.5% around $x/D = 50$. By comparison, in the work of Ihme et al. [112], NO dropped by $25 - 30\%$ due to a temperature decrease of $100 - 150$ K at the final measurement positions. The same order of magnitude for the temperature decrease was also obtained by Coehlo et al. in [109]. Conversely, Zoller et al. [119] obtained a temperature decrease around ~ 20 K like in the present study, although the NO difference from the adiabatic calculations was larger than in our results, by approximately 15%. This limited NO reduction obtained with DF-NORA could be explained by the fact that radiative

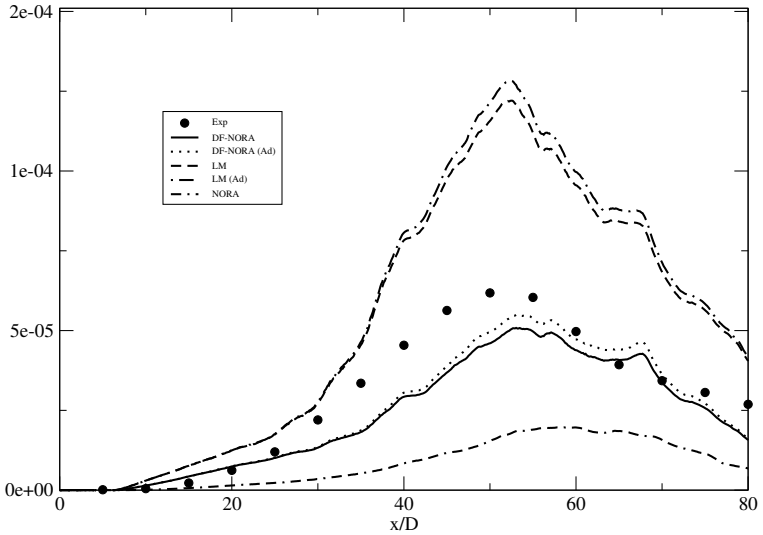

Figure 5.11 – *Axial NO mass fraction profiles for flame D. Symbols: experiments; Linear model LM (Adiabatic: Dash-dot; Full model: Dash); DF-NORA (Adiabatic: Dot; Full model: Solid); NORA (Full model: Dash-Dash-Dot).*

heat losses are treated in very different ways in both NO tabulations, but more probably, by the difference in the procedure used to tabulate the NO reaction rate as discussed for the adiabatic results above.

5.6 NO prediction in a flameless combustor

5.6.1 Experimental and numerical setup

After the academic evaluation of DF-NORA on Sandia Flame D, the laboratory configuration of Verissimo et al. [14] is considered as a step forward towards the simulation of an industrial flameless burner. The LES of this configuration with the DHR combustion model was already presented in details in Chapter 4.

Although this aspect was not explained in the [120], that is the article reported in Chapter 4, we believed to further justify why the coupling was not used for the combustion calculation in this second part. As a matter of fact, the authors of the experiment estimate the total heat losses (radiative and convective) as approximately equal to 50% of the burner power, that is 5 kW. As the maximum flame temperature is close to 1790 K, it can be assumed that radiative heat losses are negligible compared to wall heat losses. To evaluate this hypothesis, decoupled radiative heat transfer (RHT) simulations were performed, using an arbitrary instantaneous LES temperature and composition field as an input. As the wall temperature T_w is not known in this experiment, various RHT simulations were performed with T_w ranging from 700 to 1000 K. In this simulations, the radiative heat loss never exceeds 1.2 kW, which corresponds to approximately 20% of the burner heat losses, which confirms that wall heat losses are predominant in this configuration. For this reason, it was decided not to include radiative heat losses in this case unlike in Flame D. Anyway, as the temperature field is quite homogeneous (unlike in Flame D), it is legitimate to consider that radiative heat losses can be approximately included in the wall heat losses if a correct wall temperature is chosen. For this reason, the following strategy was employed: the wall temperature, which is unknown, was fitted in order to recover approximately the experimental temperature profile at the last measurement position $x = 310$ mm. This strategy led to $T_w = 700$ K, finally yielding a total heat loss of 5.3

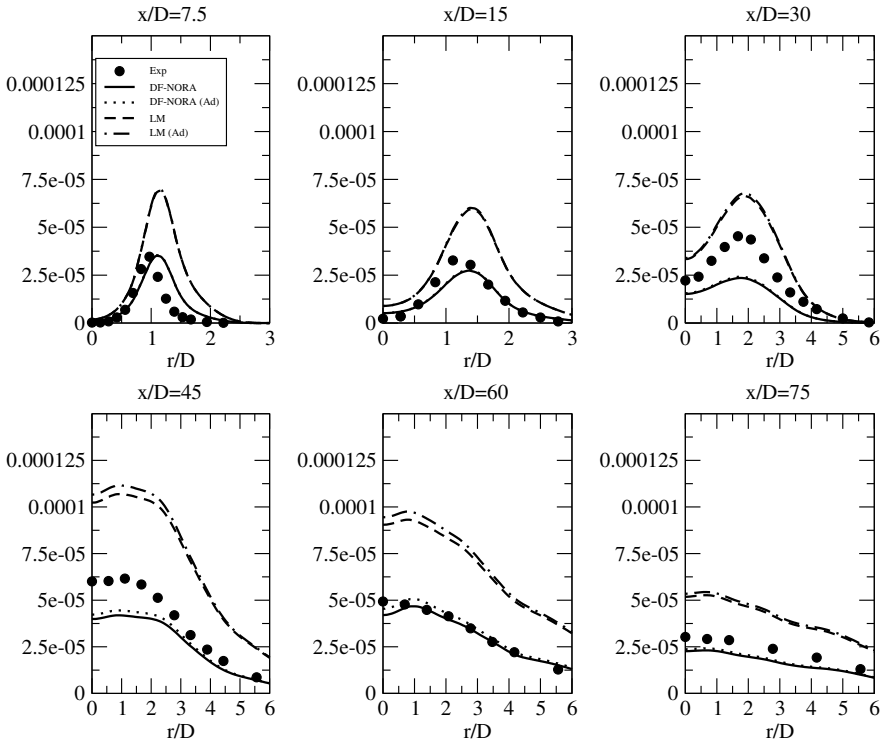

Figure 5.12 – *Radial NO mass fraction profiles for flame D. Symbols: experiments; Linear model LM (Adiabatic: Dash-dot; Full model: Dash); DF-NORA (Adiabatic: Dot; Full model: Solid).*

kW, in good agreement with the experimental estimation. In the recent work of Lamouroux et al. [142] on the same configuration, radiation effects were also neglected invoking the low temperature of the process and the small residence time.
The discretization of the DHR table is the same as in [120]. With regard to the DF-NORA table, the same type of refinement as in Flame D is employed. The range of χ_{st} is adapted to this burner, leading to a minimum value of 0.005 s^{-1} and a maximum of 50 s^{-1}.

5.6.2 NO results

In [120] , the ability of the DHR model to correctly predict temperature and main species such as CO_2 and O_2 was shown. Temperature profiles are presented in Fig. 5.13 at six measurement positions.

A good agreement with the experiment is obtained, excepted for a strong underprediction close to the injector exit at $x = 11$ mm. As outlined in [88] and [120], experimental temperature, CO_2 and O_2 measurements at this location might not be coherent, therefore making the evaluation of LES results difficult at this location.

The mean axial NO volume fraction profiles are presented in Fig. 5.14 for the three NO models considered and for the experiment. The corresponding radial profiles are presented in Fig. 5.15 at different axial locations for DF-NORA. With respect to the final experimental value of 20 ppm at $x = 310$ mm, the LM, NORA and DF-NORA models predict respectively 272 ppm, 2.52 ppm and 31 ppm. Although none of the three models correctly predicts the final value of NO, the DF-NORA performs better than the other two models. Qualitatively, axial and radial NO profiles look quite similar between the three models with a sharp increase of NO between $x = 0$ and $x = 50$ mm approximately which corresponds to the beginning of the dilution of

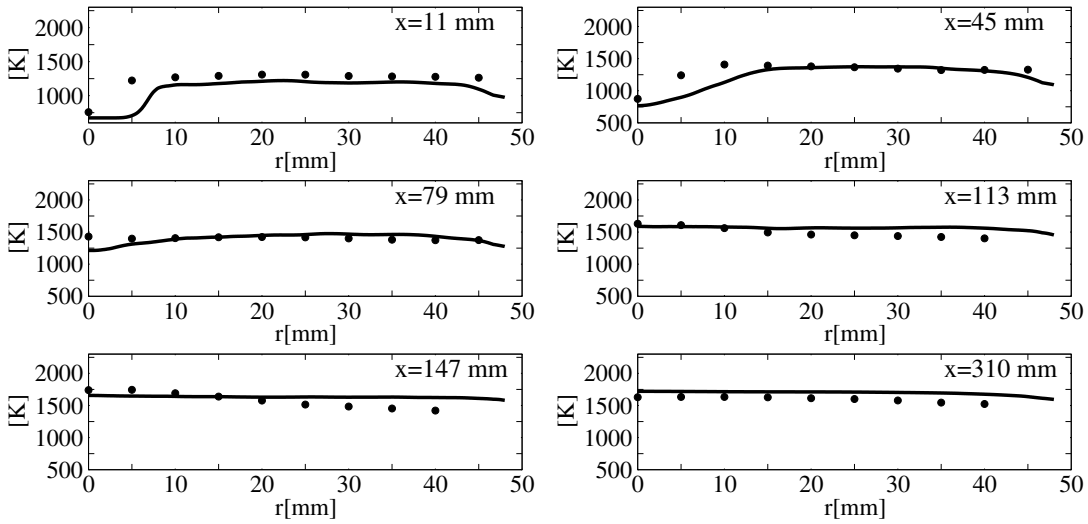

Figure 5.13 – *Radial profiles of the mean temperature for the flameless case: experiments (symbols), LES (solid line).*

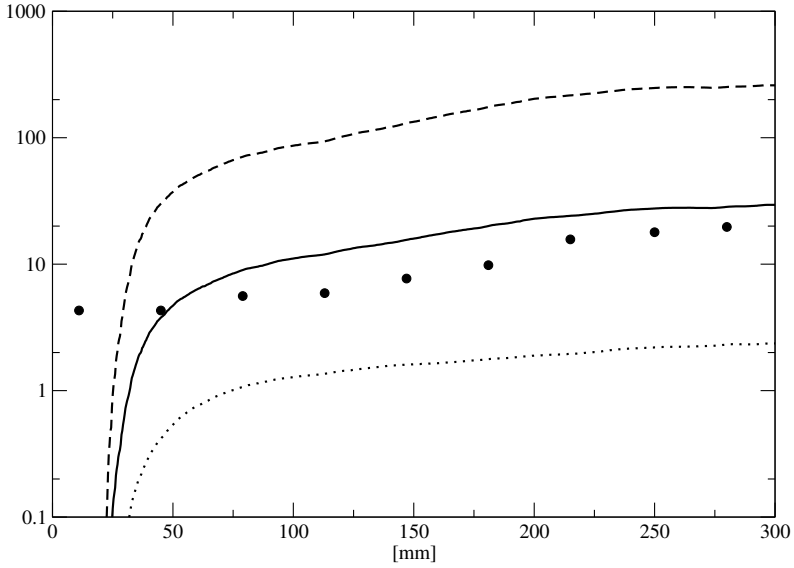

Figure 5.14 – *NO axial profiles for the Verissimo test case. Symbols: experiments; Linear model LM: Dash; DF-NORA: Solid; NORA: Dot.*

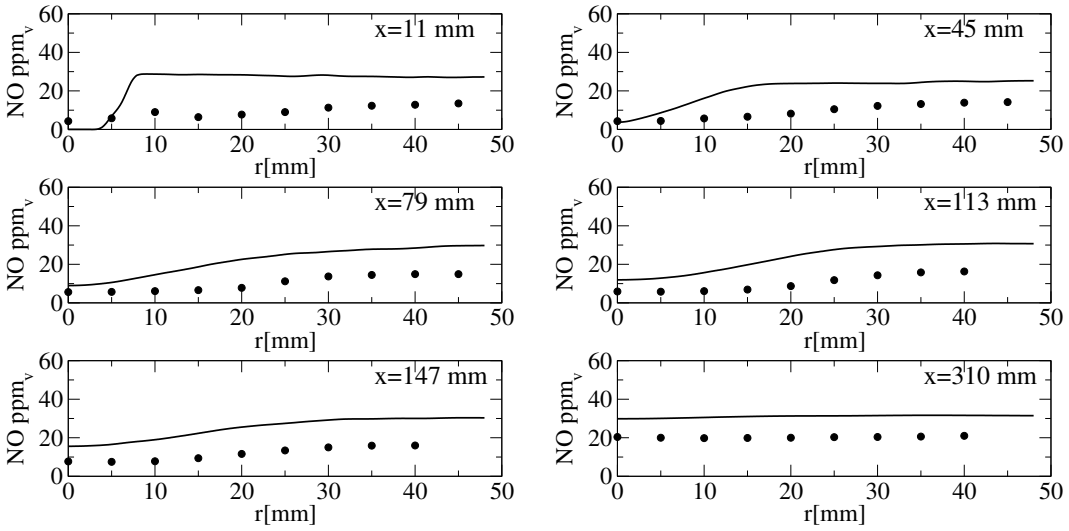

Figure 5.15 – *Radial profiles of the mean NO concentration for the Verissimo configuration. Symbols: experiments. Solid line: DF-NORA.*

the fresh mixture with burnt gases. On the contrary, the experiment presents a much larger initial value of 4 ppm at $x = 11$ mm with a more progressive increase downstream. This rather high initial NO value could be explained by the presence of recirculated burnt gases close to the injector at $x = 11$ mm which would bring back part of the NO formed in the flame. At the same time, this hypothesis would not be consistent with the CO_2 and O_2 measurements at this location, which are equal to zero. As the LES predicts the presence of nearly fresh gases at $x = 11$ mm (see Fig. 5.13 for instance), this recirculation of NO can not be observed there.

The radial profiles of DF-NORA compare qualitatively well with the experiment with a flattening of the profiles for $x > 113$ mm. The corresponding radial profiles for LM and NORA look qualitatively similar to those of DF-NORA (not shown), excepted that they are shifted like on the axial profiles Fig. 5.14.

The major difference between experiment and LES lies in the upstream part of the recirculation at $x = 11$ mm (at large radii). In the experiment, the NO concentration at large radii, that is in the recirculation, decreases from 20 ppm at $x = 310$ mm to 13 ppm at $x = 11$ mm. In the LES, the NO level is nearly identical at both locations which is explained by the freezing of reactions in the recirculation zone which presents temperatures lower than in the flame region. Further analysis would certainly be necessary to assess if the recycling mechanism which was previously shown to play a major role in diluted combustion [143] could play a role in this configuration. This is clearly outside the scope of this study since the GRI mechanism was shown to be not well suited for reburning prediction [144].

The radial profiles of the mean NO reaction rate are presented in Fig. 5.16 for the three models. All the models present a negligible reaction rate at $x = 11$ mm due to a too low temperature. NO starts to form at $x \sim 45$ mm on the border of the air jet due to the presence of recirculated burnt gases which surround the central jet of the flame. This is evidenced looking at an instantaneous LES field of $\tilde{T}$, $\tilde{\chi}_{st}$ and $\tilde{c}$ in Fig. 5.17. Scalar dissipation is the largest close the air jet axis for $x < 45$ mm, but temperature is too low there to favor NO production. This is reflected in the NO models by the fact that as $\tilde{c} << 1$, the effective enthalpy $\tilde{H}^*$ is much lower than $\tilde{H}$. On the contrary, at $x = 45$ mm on the side of the air jet, $\tilde{c}$ is close to unity do to the recirculation of burnt gases and NO production can start. The NO reaction rate is the largest for

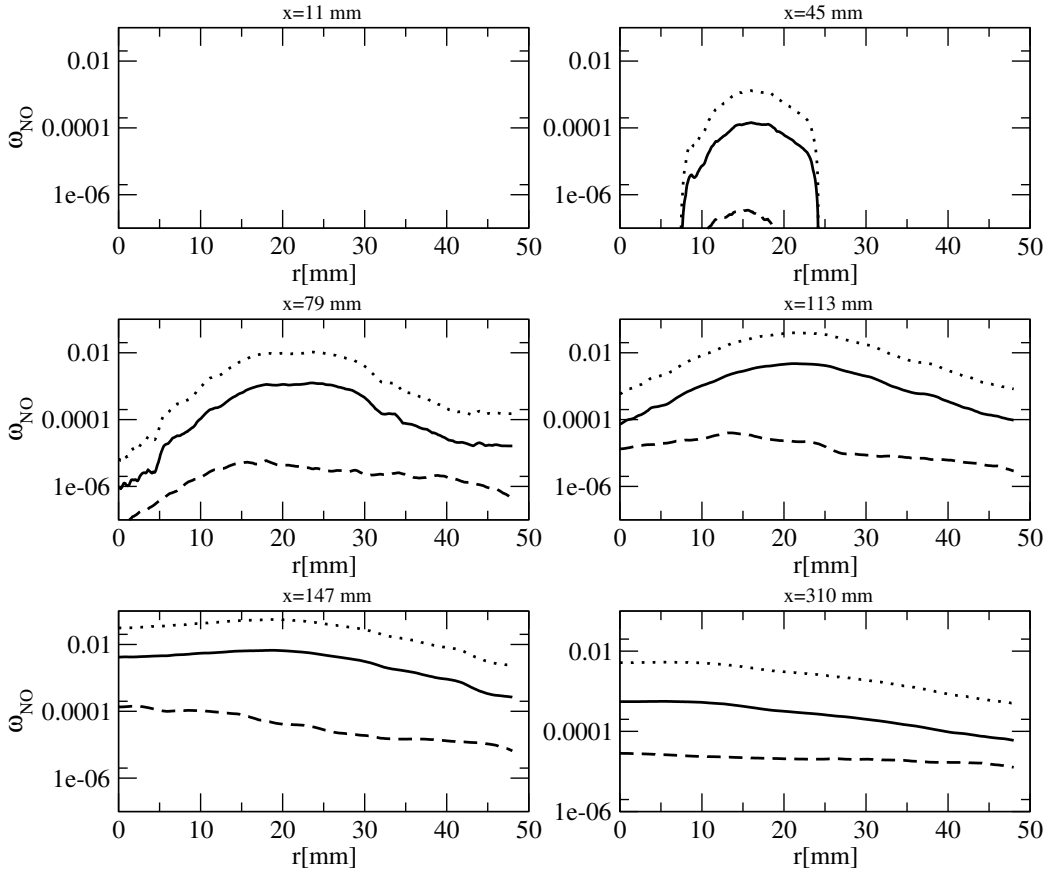

Figure 5.16 – *Radial profiles of the mean NO reaction rate $\tilde{\omega}_{NO}$ for the Verissimo configuration. Dots: LM. Solid line: DF-NORA. Dashed line: NORA.*

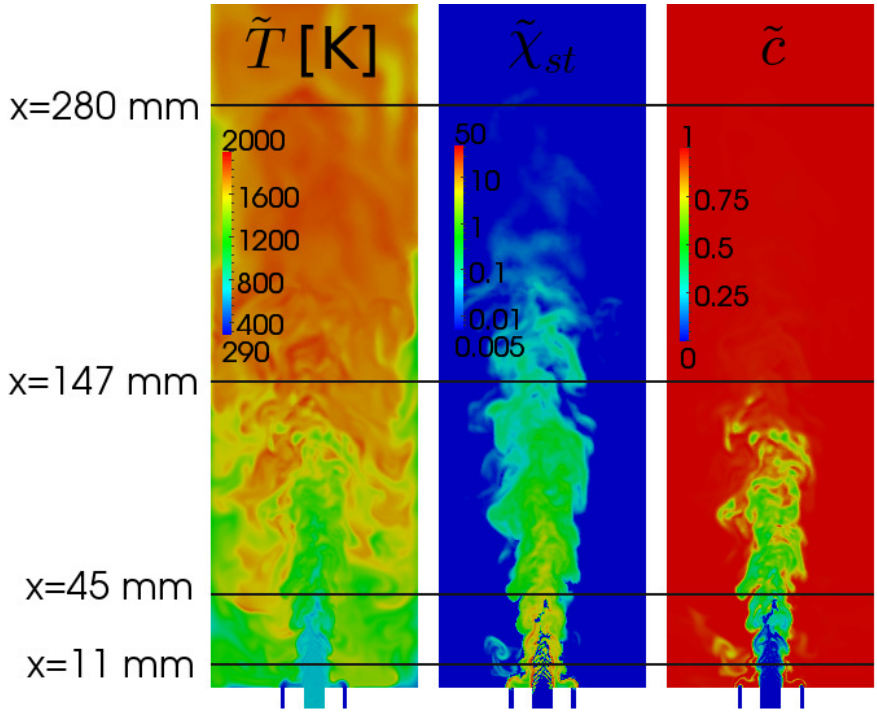

Figure 5.17 – *Instantaneous LES fields of temperature $\tilde{T}$ (left), scalar dissipation $\tilde{\chi}_{st}$ (center) and progress variable advancement $\tilde{c}$ (right).*

$79 \leq x \leq 147$ mm where temperature is the largest and $\tilde{\chi}_{st}$ still presents relatively large values. On overall, the LM and DF-NORA reaction rates, like for NO concentration profiles, look qualitatively similar with a difference of approximately an order of magnitude. For $x \leq 113$ mm, these reaction rates decrease towards the axis ($r = 0$ mm) because scalar dissipation is lower and the mixture is leaner. They also decrease towards walls ($r = 48$ mm) because scalar dissipation and temperature decrease there. DF-NORA and LM reaction rates are much larger than that of NORA due to their sensitivity to strain. At $x = 310$ mm, as explained before, scalar dissipation has decreased by more than an order of magnitude, so reducing the relative difference between the three models. In order to better understand the NO formation in this combustor, the normalized axial profiles of mixture fraction, temperature, χ_{st} and $\dot{\omega}_{NO}$ are presented in Fig. 5.18 for DF-NORA.

The presented profiles are normalized by their highest value on the jet axis. This figure shows a first increase of mixture fraction from zero at the air injector exit, up to values close to $0.9Z_d$ at $x \simeq 125$ mm, which is a consequence of the air jet mixing with recirculated burnt gases and with the injected methane. The increase of the NO concentration on the axial profile prior to the onset of NO reactions (see Fig. 5.14) is explained both by the onset of reactions at larger radii (see Fig. 5.16) and by the dilution by burnt gases which already contain NO at a concentration close to 30 ppm. The increase of mixture fraction is followed by an increase of temperature corresponding to the oxidation of the fuel/air mixture thus formed. The NO reaction rate $\dot{\omega}_{NO}$ presents a sharp rise in the interval $125 < x < 175$ mm when both $\tilde{Z}$ and temperature become large enough. Note that although the mixture is quite lean in average, the SGS mixture fraction fluctuations lead to a non negligible contribution of mixtures close to stoechiometry. χ_{st} presents a peak value at $x = 50$ mm, while it decreases to approximately 2.5% of this peak value at the NO reaction rate peak value. This percentage corresponds to $\chi_{st} = 0.038$ s^{-1} which is larger than the minimum DF-NORA value $\chi_{st}^{min} = 0.005$ s^{-1}. This means that the NO reaction rate in DF-NORA is essentially given by the diffusion flame at this location, and not by NORA. This explains the large discrepancy between NORA and

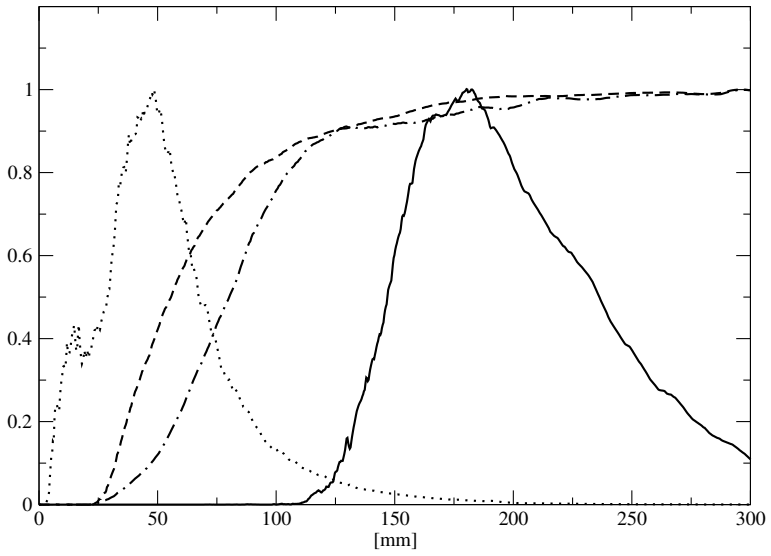

Figure 5.18 – *Axial mean normalized profiles for the Verissimo configuration. Dots:* $\tilde{\chi}_{st}/2.58$*. Dashed line:* $\tilde{Z}/0.042$*. Dashed-dot line:* $\tilde{T}/1580$*. Solid line:* $\tilde{\omega}_{NO}/0.083$ *for DF-NORA.*

DF-NORA in the final NO yield. Further downstream, $\dot{\omega}_{NO}$ sharply decreases in the region $165 < x < 300$ mm. This decrease is not explained neither by temperature nor by mixture fraction which remain large, but by the rapid decrease of χ_{st} which strongly affects the NO reaction rate.

5.7 Conclusions

Three LES models devoted to the NO prediction in under-adiabatic furnaces were evaluated in this paper: the NORA model [111], based on the NO relaxation towards equilibrium, the linear model (LM) [112] based on the equilibrium state of a laminar diffusion flame and a new model, DF-NORA, in which the linear approximation of the LM is replaced by a tabulation of the reaction rate as a function of a NO progress variable, following the idea of [119]. To generate this table, NO relaxation complex chemistry calculations are used like in NORA, but this time, the homogeneous reactor is replaced by a steady laminar diffusion flame.

These models were first employed in the partially premixed diffusion Flame D of Sandia. The NORA model underpredicted the NO production due to its insensitivity to strain which promotes NO formation. On the other hand, results consistent with those of Ihme and Zoller [112, 119] were obtained for the LM, presenting an overprediction of the experimental results. The DF-NORA presented the best prediction of the three models with an underprediction of 30 % in the region $30 < x/D < 50$. The impact of a radiative term source was also assessed, showing a local decrease of NO by less than 7% compared to the adiabatic calculation for the DF-NORA model.

The same models were then applied to the flameless configuration of Verissimo et al. [14] showing strong heat losses and strong dilution by burnt gases like in a real furnace. The NORA and LM approaches underestimated, respectively over-estimated, the final NO

yield by an order of magnitude. The best results where obtained with DF-NORA, with an overestimation of 30%. An analysis was carried out for this configuration in order to identify the NO formation mechanism. In this flameless configuration, fuel oxidation starts quite far downstream at $x \simeq 50$ mm, when fresh gases, fuel and burnt gases have already partially mixed. As a consequence, unlike in an attached flame like flame D, the NO peak reaction rate is located further downstream at $x \simeq 175$ mm. At this location, the filtered mixture fraction is already close to the mean combustor mixture fraction $\Phi = 0.77$. Although this value is not favorable to NO production, mixture fraction fluctuations are large enough to include close to stoechiometric mixtures in the filtered NO reaction rate. For DF-NORA and LM, the NO reaction rate highly depends on scalar dissipation, which peak is found close to the air injector exit at $x \simeq 50$ mm. At the peak of NO reactions, scalar dissipation is only 2.5% of its peak value, but it is found sufficient to highly promote NO formation compared to a zero strain (or homogeneous) mixture, like used in NORA. This result shows that although flameless combustion takes place in a quite homogeneous, low strain region, the presence of a residual strain and inhomogeneity are sufficient to promote NO formation. This promotion still remains limited compared to a conventional combustion mode as proved by the final experimental NO yield of 20 ppm.

Conclusions and perspectives 6

6.1 Main conclusions and resume

In this thesis, the numerical modeling of flameless combustion was investigated. The environmental emergency has pushed the combustion community to develop more efficient and less polluting technologies. It was observed that among these technologies, FC offers an interesting combination of a more efficient and less polluting technology [13, 19], as well as a more diffused temperature field, which can be exploited in the steel, glass and ceramic industry [28]. In order to investigate and deepen the physical aspects tied to the technology, numerical techniques represent an interesting tool, due to their reduced cost, compared to laboratory experimental setups. It was argued that the three streams turbulent mixing of FC can be challenging for numerical techniques [63, 49]. For this reason, in this thesis, the choice of using Large Eddy Simulations (LES) was made, in order to have a more qualitative and quantitative prediction of turbulence, compared to RANS. This thesis was developed in two main parts. In the first, the combustion DHR model, suitable for FC modelling, was developed. In the second part, the research was addressed towards the *NO* pollutant modelling. In the following section, the two models are presented.

6.1.1 The combustion model DHR and the pollutant model DF-NORA

A combustion model suitable for LES simulations of FC was developed in this thesis. The characteristics sought for the model, were the following:

- large enthalpy losses taken into account;
- three stream mixing description;
- minimal time consumption.

These characteristics were included in the Diluted Homogeneous Reactors model (DHR). In particular, a fresh gases state in a reactor, is diluted with hot burnt gases at equilibrium. The consequent auto-ignition is tabulated as a function of a progress variable. An enthalpy loss is introduced by reducing the equilibrium temperature of the diluting burnt gases. In order to introduce a radiation loss, the AVBP LES code was coupled with the PRISSMA-oPALM (employed in [130, 131]) numerical setup, along with the WSGG model [134]. With regard to pollutant modelling, the DF-NORA was developed instead. The starting observation to develop the model was that in a FC combustor, high and low strain regions can be found. *NO* production can have a radically different reaction rate in these regions. With regard to the strained regions, the DF-NORA model was developed. In the model the productive/destructive division for the *NO* reaction rate of Ihme et al.[48] was used. However, with respect to their model, the linear hypothesis was left aside because, as argued by Zoller et al.[119], it can yield to an overprediction of *NO*. As a matter of fact, nitrogen species such as NO_2 or N_2O can yield to

non-linearities during NO relaxation towards equilibrium. In this sense, the DF-NORA tabulation is developed in two steps:

- a set of steady flamelets at equilibrium without the NO mechanism is created;
- the NO mechanism is activated at time $t = 0$, and its relaxation towards equilibrium is tabulated as a function of a progress variable c_{NO}, based on unsteady flamelet calculations.

With regard to the non-strained regions, the NORA model [111], was used. It consists in tabulating the NO relaxation towards equilibrium of a burnt gases mixture as a function of a progress variable c_{NO}, for which NO mass fraction was augmented of a ΔY_{NO} quantity.

6.1.2 Flame D simulations

The DHR model was first validated on a partially premixed diffusion flame Flame D from Sandia laboratories. Results of the model were found in agreement with the experimental data, although CO was overestimated in a precise range of mixture fractions, due to the use of homogeneous reactors ([65, 70]). The absence of the strain notion in the model was evident when using the model with the Flame F, a more strained flame than Flame D. With regard to pollutant NO modelling, results were found in good agreement with the experimental results, although an underestimation of NO was found in the region $30 < x/D < 45$. It was also shown that the NORA model is not able to predict correctly the NO production for Flame D, showing an underestimation of the experimental results by a factor of 3.

6.1.3 Verissimo flameless combustor simulations

After being validated on the Flame D, the DHR model was then employed in a real flameless combustor, from Verissimo et al.[14]. Results were found in correct agreement with experimental data. A discordance was observed in the temperature (well predicted), O_2 (underestimated) and CO_2 (overestimated) results in the upstream part of the flame, which can be attributed to experimental uncertainty as well as to a lack of precision of the model. The results on the two configurations for the DHR model, were reported in an article submitted to *Flow Turbulence and Combustion* [120]. DF-NORA was then used for the Verissimo configuration. It was observed that the model overestimated the final quantity of NO by a factor of 3. However, with respect to the linear approach LM and NORA, its results were the closest to the experimental data. Results on NO prediction in FC and for the Flame D, were reported in an article submitted to *Flow Turbulence and Combustion*.

6.2 Main Perspective in combustion and pollutant modeling in FC

The DHR combustion and the pollutant DF-NORA models for non-premixed flamed and in particular for FC were developed in this thesis. The two models performed quite well for the two configurations presented above. Of course, some points for the two models are still to be developed and investigated.

6.2.1 Perspectives on DHR

Accounting for the strain rate

In the SANDIA Flame D temperature profiles at $x/D = 15$ were slightly overestimated. This point was further investigated on Flame F. In this case, the temperature overestimation was more remarkable. In [70], a comparison between premixed and non-premixed manifolds was shown for Flame D and F, presenting a net improvement when using the latter manifolds. An improvement in this direction can be also sought for DHR. Exactly as done for the DHR model, where a fresh gases reactor is diluted with burnt gases, it could be possible to dilute a mixing line of fuel and air with burnt gases at equilibrium, to provoke auto-ignition. The enthalpy losses can be introduced by decreasing the enthalpy of the diluting burnt gases. In this case, the model would account for the enthalpy loss and the strain rate.

Modelling of the dilution rate

In the first modelling of the DHR model proposed in this thesis, α was set equal to α_{reac} the first dilution rate value allowing auto-ignition. It was observed that this modelling could be responsible for some discrepancies with the experimental data. This approach could be improved, by including a transport equation for α. Its source term should be built in order to individuate the diluent burnt gases.

6.2.2 Perspectives for DF-NORA

Effects of dilution on DF-NORA

The DF-NORA, although presenting improved results with respect to NORA and the linear model, overestimated the final level of NO for the Verissimo test case. A possible explanation for this overprediction lies in the fact that the diffusion flames do not account for diluent gases in the fuel and air streams. A possible way to improve both this model and tge DHR model would be to consider dilution in the flamelet structure. In this case, it should be investigated how dilution impacts the forward/backward reaction rates of NO.

Subgrid model influence

Improving the SGS models could be investigated for DF-NORA. In particular, the influence of strain rate fluctuation could be investigated. Moreover, this modification should not significantly the computational costs, because the NO model has a negligible computational cost, compared to the total simulation CPU time.

Annexes

I Radiations aspects

In the article presented above, the influence of radiation on the NO species for the Flame D was investigated. In this complementary part, the effects of radiation on turbulent combustion is illustrated in more detail. In the calculations presented in the article, the WSGG was employed. In order to choose the appropriate radiation model for Flame D, preliminary a priori tests were first performed on one iteration of the radiative solver for a randomly chosen simulation time t, with different models. These tests are reported in table 6.1.

Table 6.1 – *Preliminary tests for radiation models for Flame D for one radiative iteration for a one randomly chosen time t. Power of the flame calculated* 10850 *W*

Model	Power Loss	Power Loss Fraction
SNB-CK	602	5.54%
SNB-FSCK	864	7.9%
WSGG	575 W	5.3%

The SNB-CK model is considered as a reference, but its usage in the coupled calculations is computationally too expensive. The SNB-FSCK model [145] is a tabulated model in which the gas spectrum bands are grouped together and described by analytical functions. It can be seen in table 6.1 that the WSGG presents a power loss closer to the reference SNB-CK compared to the SNB-FSCK. This test proved that the WSGG, despite its simplicity, is a good approach to describe radiation for this configuration. The fact that WSGG performs better than the more sophisticated SNB-FSCK model might be explained by the fact that WSGG was designed exactly for methane/air non premixed combustion.

The adiabatic and the coupled calculations can now be compared. The axial profiles of the two flames are presented in Fig.6.1.

It can be noticed that radiation tends to reduce the RMS of mixture fraction, which leads to a better agreement with the experiment compared to the adiabatic simulation. The reason why radiation is able to reduce the turbulent fluctuations was reported in [131]. When radiation is considered, an energy exchange between hot and fresh gases occurs, thus homogenizing the energy distribution and consequently smoothing the turbulent fields and reducing turbulent fluctuations.

The difference in mixture fraction RMS prediction has an effect on temperature and progress variable $\tilde{Y}_c$ predictions. It can be noticed that in the downstream part of the flame, the progress variable is underpredicted in the adiabatic calculations, whereas it is quite well reproduced by the coupled simulation. Note that velocity is only slightly different between the two different simulations. As the two calculations present two different profiles of average mixture fraction, it is difficult to calculate the temperature variation ΔT due to radiation.

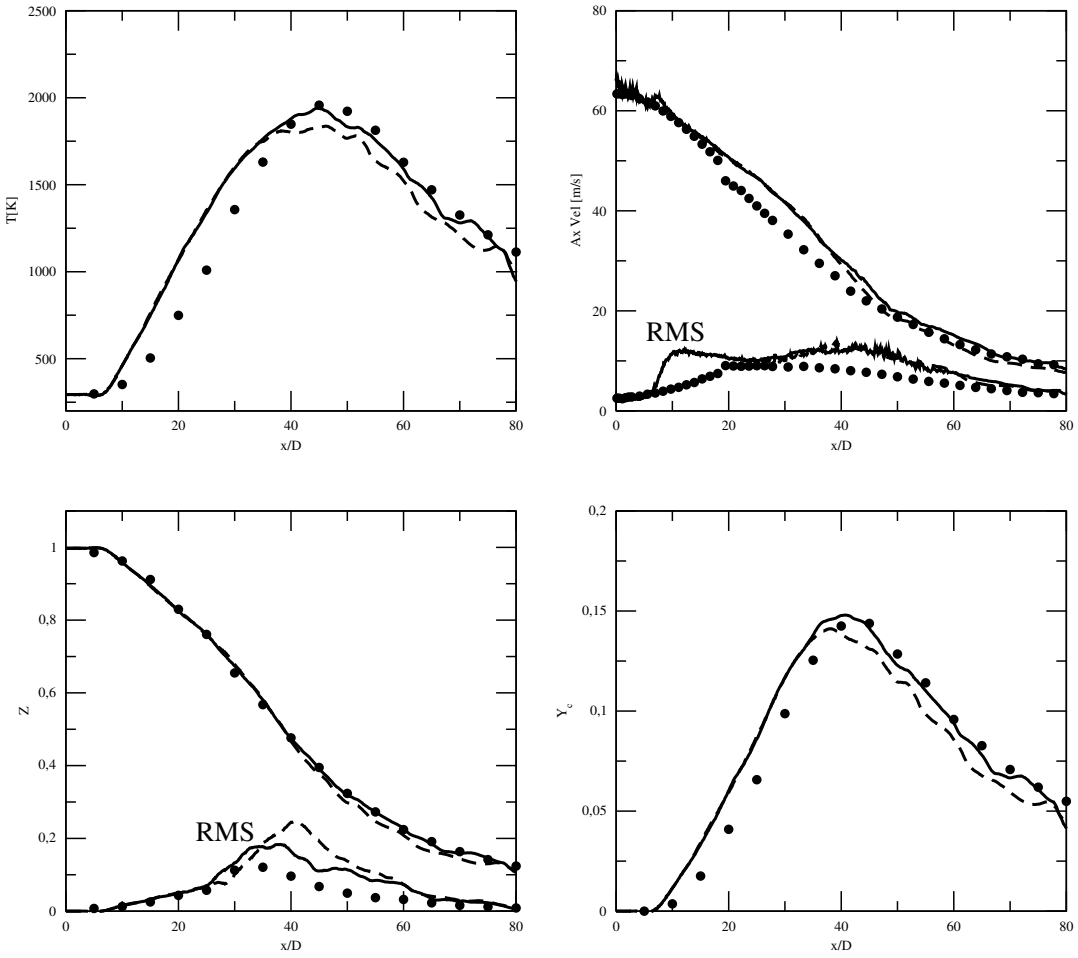

Figure 6.1 – *Temperature, velocity, mixture fraction and progress variable axial profiles for Flame D. Solid lines: coupled calculations. Dashed lines: adiabatic calculations.*

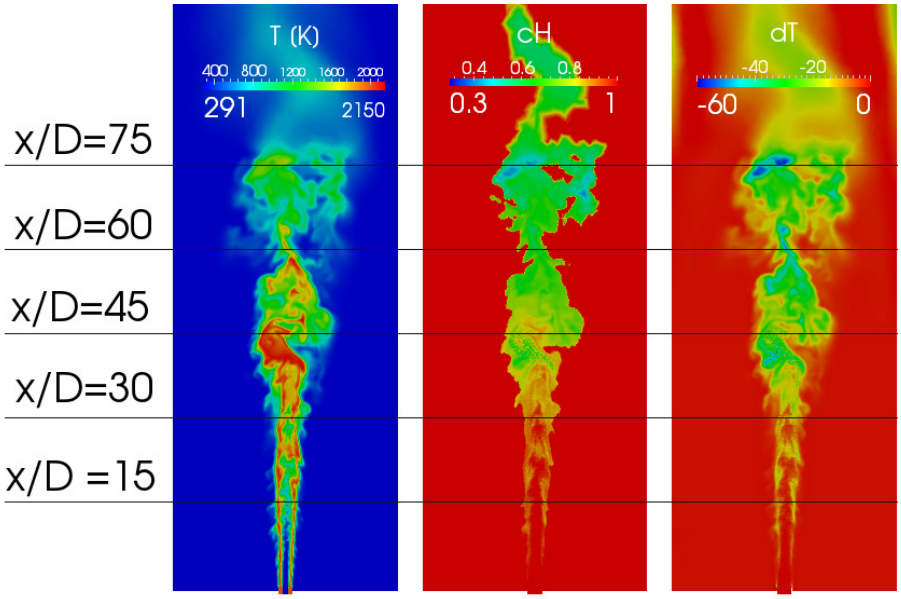

Figure 6.2 – *Temperature, $\tilde{c}_H$ and ΔT for the coupled simulations for the Flame D*

In Fig. 6.2, fields of temperature, $\tilde{c}_H$ and ΔT are shown. ΔT is estimated as $\frac{\tilde{H}-\tilde{H}^u}{\tilde{C}_p}$ where $\tilde{H}^u$ is the total fresh gases enthalpy and $\tilde{C}_p$ is the specific heat at constant pressure. It can be seen that on average ΔT is close to -20 K, which corresponds to a value of $\tilde{c}_H$ around 0.75. These calculations show that the DHR model allows the observation of the turbulence radiation interaction (TRI) in this flame, even if the enthalpy loss is very moderate. Much larger effects of TRI can be expected on the flame of a furnace undergoing radiative heat losses of the order of hundreds of Kelvins.

II The DHR-NORA model

This model was meant to improve the NORA model in predicting NO in diffusion flames. In this model, called DHR-NORA model, a homogeneous reactor at mixture fraction Z and enthalpy H is diluted with burnt gases. The diluting burnt gases are a mixture of gases at equilibrium, without the NO mechanism activated. In this way, at the instant $t = 0$ before auto-ignition, no nitrogen species are present in the reactor. In the second phase, the entire chemistry mechanism is activated. During auto-ignition, the nitrogen species relax towards equilibrium. This is shown in Fig.6.3(a), where the progress variable Y_c, which tracks the auto-ignition, is represented along with Y_{NO} as a function of time. It can be also noticed that the NO relaxation time is much larger than the one of combustion. This clearly shows the impossibility of comprehending the NO species directly in the combustion table. It is possible to calculate the NO reaction rate and the relaxation time as:

$$\dot{\omega}_{NO}(t) = \frac{Y_{NO}(t+dt) - Y_{NO}}{dt} \qquad \tau_{NO} = \frac{Y^{eq}_{NO} - Y_{NO}(t)}{\dot{\omega}_{NO}(t)} \tag{6.1}$$

The relaxation time is plotted as a function of time in Fig.6.3(b).

It can be noticed that in the first part of auto-ignition, τ_{NO} presents very low values; as relaxation continues, a net peak of τ_{NO} can be distinguished; then it relaxes towards a steady value. τ_{NO} is then plotted as a function of c in Fig.6.3(c). The relaxation time shows the lowest value for $c < 1$, around $c = 0.85$. The peak of τ_{NO} is reached when the reactor is at equilibrium

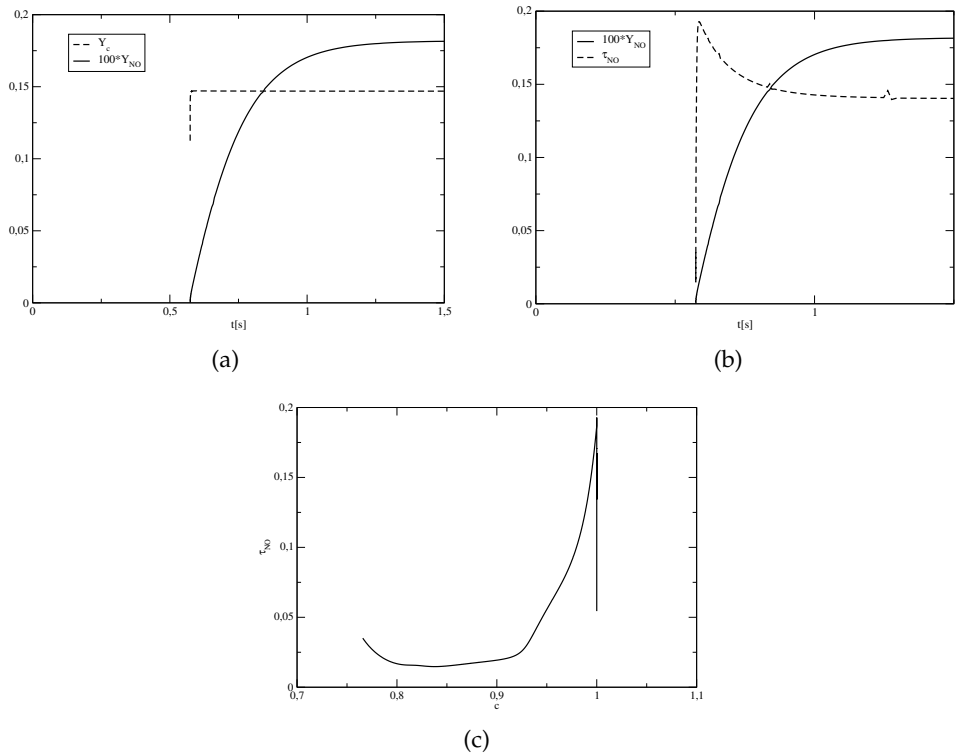

Figure 6.3 – *Auto igniting diluted reactor NO variables. Fig.6.3(a): Progress variable and Y_{NO} as a function of time; Fig.6.3(b): Relaxation time and Y_{NO} as a function of time; Fig.6.3(c): Relaxation time as a function of progress variable advancement c.*

around $c = 1$. It was also observed that, if $c = 1$, for a given Z and H, τ_{NO} was extremely close to the τ_{NORA}, i.e. the relaxation time of the NORA model, for the same Z and H. This means that this model for $c = 1$ is equivalent to NORA. In this sense and in order to exploit the model for the Flame D calculations, if the c_{DHR} were used as an input parameter for the DHR-NORA table, this would have yielded to the same results of NORA. As a matter of fact, the c_{DHR} relax towards a unitary value very fast, which is typical of homogeneous reactors tabulation. On the contrary, a table of c from a flamelet library can be created. For each flamelet, for a given Z and for a given H, c_{DF} is calculated as:

$$c_{DF}(Z, H, \chi_{st}) = \frac{Y_{CO}(Z, H, \chi_{st}) + Y_{CO_2}(Z, H, \chi_{st})}{Y_c^{eq}(Z, H)} \tag{6.2}$$

where Y_c^{eq} is calculated from the homogeneous reactors. Using c_{DF} as an input parameter is more convenient to improve the NORA results, as it is theoretically always lower than 1, apart from non-strained regions. The model was not further investigated for some inconsistencies with the flamelet structure for the richer Z. In Fig.6.4, the reaction rate and the Y_{NO} as a function of mixture fraction and time are represented. The reaction rate is calculated by using a set of τ_{NO} calculated with adiabatic reactors for 20 mixture fraction in the interval $0 \leq Z \leq 0.2$. For the calculations a constant profile of c_{DF} from a flamelet with $\chi_{st} = 10$ and boundary conditions from the Flame D was used. It can be noticed that at $t = 0$ the reaction rate presents two peaks, one place around $Z = Z_{st}$ and another one much larger for the richer Z. Due to these not regular distribution of the reaction rate around Z, NO relaxes towards equilibrium presenting two distinguished peaks. The reason for this behavior is due to the different compositions of the DH reactors and the flamelets, for a given Z, with the same c.

Table 6.2 presents the relative difference of CO, CO_2 and O_2 for two different Z and for the same c. It can be noticed that, around stoichiometry, the flamelet and the homogeneous

Table 6.2 – *Differences in major species for the DHR-NORA reactors and flamelet for a given Z and c.*

	c	ΔCO	ΔCO_2	ΔO_2
$Z = Z_{st}$	0.93	4.3%	2.2%	5.1%
$Z = 0.07$	0.98	4.9%	5.1%	16.6%

reactors present very close values of the species. On the contrary, for a rich value of Z, CO and CO_2 are still very close, whereas O_2 is much higher in the homogeneous reactors than in the flamelet. For this reason, it is possible that the NO relaxation is somehow accelerated by a high presence of O_2, which causes the peak of ω_{NO} of Fig.6.4.

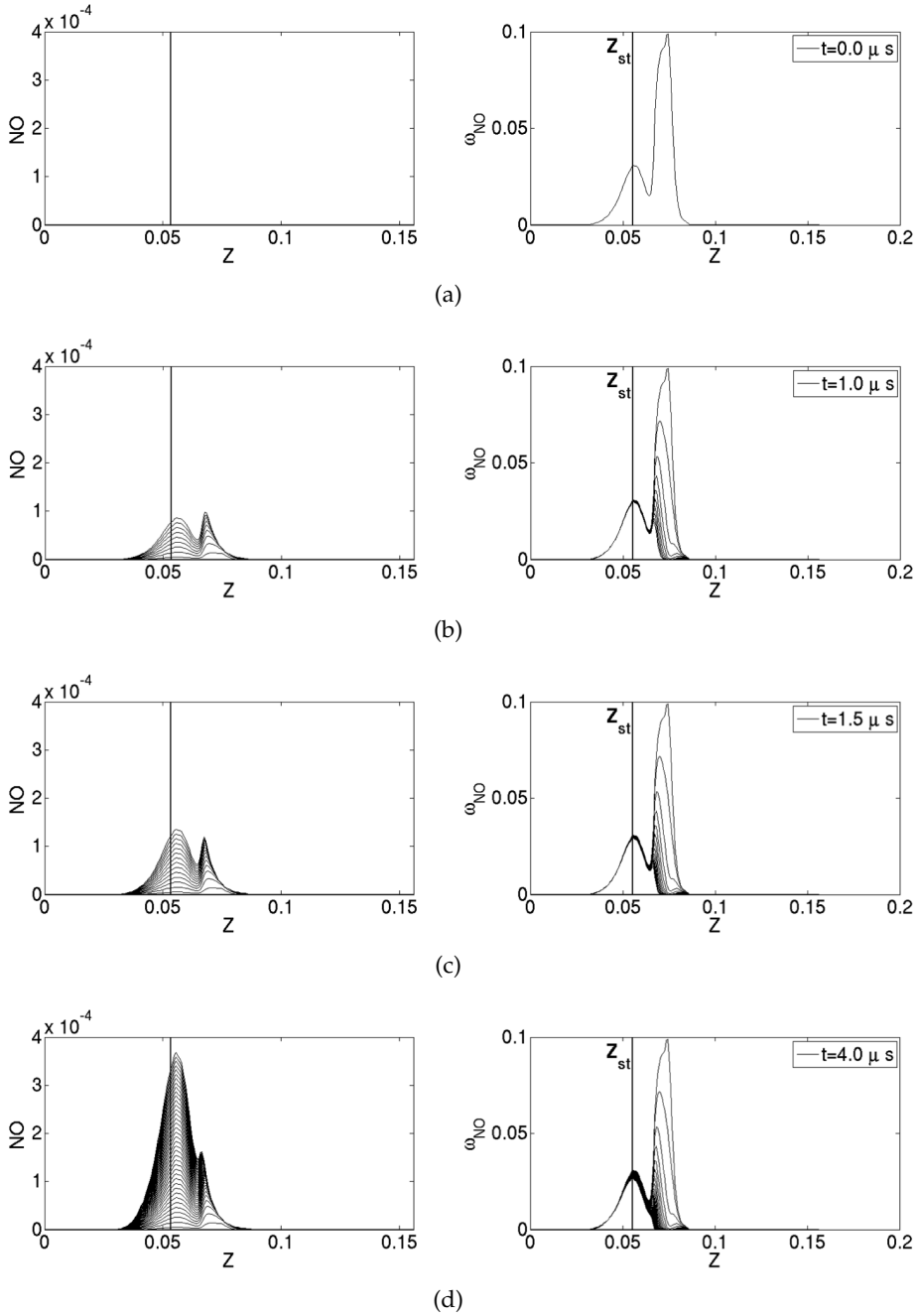

Figure 6.4 – *Calculations with the DHR-NORA model: NO growth and reaction rate as a function of mixture fraction and as a function of time t. c_{DF} obtained from a flamelet at $\chi_{st} = 10$ and boundary conditions of Flame D.*

List of Figures

List of Tables

Bibliography

[1] Internation Energy Agency. Key world energy statistics. 2012. (Cited in pages 1, 75 et 113.)

[2] J.P. Tomain. Ending dirty energy policy: Prelude to climate change. *Cambridge Press*, 2011. (Cited in page 1.)

[3] U.S. energy information energy. Annual energy outlook. 2011. (Cited in pages 2 et 113.)

[4] European commision. Energy mix fact sheet. 2007. (Cited in pages 2 et 113.)

[5] Asia pacific energy research centre. Energy in china: transportation, electric power and fuel markets. 2004. (Cited in pages 2 et 113.)

[6] Green Car Reports. *www.greencarreports.com*, 2014. (Cited in page 2.)

[7] N. Stern. Stern review on the economics of climate change. 2007. (Cited in page 2.)

[8] J.M. Deutch. The crisis in energy policy. *Harvard University Press*, 2011. (Cited in page 2.)

[9] T. Nicolai. Urban traffic and pollutant exposure related to respiratory outcomes and atopy in a large sample of children. *Europ. Resp. Jour.*, 21:956–963, 2003. (Cited in page 2.)

[10] A. Lovins. Available at www.ccnr.org/amory.html. 1989. (Cited in page 3.)

[11] O. Zehner. Green illusions. *University of Nebraska Press*, 2012. (Cited in pages 3 et 4.)

[12] Strategic Energy Technologies Information System. setis.ec.europa.eu. (Cited in pages 5 et 113.)

[13] J.A. Wunning; J.G. Wunning. Flameless oxidation to reduce thermal no-formation. *Prog. Energy Combust. Sci.*, 23:81–94, 1997. (Cited in pages 4, 7, 9, 10, 11, 12, 14, 18, 19, 21, 35, 37, 38, 76, 103 et 113.)

[14] A.S. Verissimo; A.M.A Rocha; M. Costa. Operational, combustion, and emission characteristics of a small-scale combustor. *Ener. Fuel.*, 25:2469–2480, 2011. (Cited in pages 5, 20, 21, 33, 34, 35, 38, 59, 63, 64, 65, 67, 71, 74, 75, 77, 94, 100, 104, 114, 115 et 117.)

[15] T. Plessing; N. Peters; J.G Wunning. Laseroptical investigation of highly preheated combustion with strong exhaust gas recirculation. *Proc. Combust. Inst.*, 27:3197–3204, 1998. (Cited in pages 8, 12, 18, 21, 26, 32, 35, 38 et 113.)

[16] B. Özdemir; N. Peters. Characteristics of the reaction zone in a combustor operating at mild combustion. *Exper. Fluid*, 30:683–695, 2001. (Cited in pages 8, 19, 21, 26 et 113.)

[17] R. Borghi. On the structure and morphology of premixed flames. *Rec. Adva. Aerospace Sci.*, 117-138, 1985. (Cited in page 9.)

[18] T. Poinsot; D. Veynante. Theoretical and numerical combustion. 3rd edition. 2012. (Cited in pages 9, 32 et 55.)

[19] A. Cavaliere; M. de Joannon. Mild combustion. *Prog. Energy Combust. Sci.*, 30:329–366, 2004. (Cited in pages 10, 11, 23, 37, 76, 103 et 113.)

[20] M. Oberlack; R. Arlitt; N. Peters. On stochastic damköhler number variations in a homogeneous flow reactor. *Combust. Theor. Model.*, 4:495–509, 2000. (Cited in page 10.)

[21] E. Malfa; J. Niska; S.M. Almeida; M. Fantuzzi; M. Fernandez; H.P. Gitzinger; M. Mortberg. Minimizing nox emissions from reheating furnaces. *Combust. Colloq.*, 32:2009. (Cited in page 12.)

[22] J.G. Wunning. Energy saving potentials for gas fired industrial furnaces. *Thermprocess Symposium*, 2007. (Cited in pages 13 et 113.)

[23] M.Flamme; A.A Halbouni; J.G. Wunning; V. Scherer; M. Schlieper. Low emission gas turbine combustor based on flameless oxidation. *14th IFRF Member Conference*, 2004. (Cited in page 13.)

[24] C. Fielenbach; T. Holfeld; C. Petery; U. Renz; J.G. Wunning. Nox−reduction in a pressurized pulverized coal flame by flue gas recirculation. *Pittsburgh Coal Conference*, 2003. (Cited in page 13.)

[25] C. Villermaux. Innovative and efficient technologies for industry. *International Gas Union Research Conference*, 2011. (Cited in page 13.)

[26] A. Milani; J.G. Wunning. Radiant tube technology for strip line furnaces. *IFRF Combustion Journal*, 200405, 2004. (Cited in pages 14 et 113.)

[27] J.G. Wunning. Flox flameless combustion. *Thermprocess Symposium*, 2003. (Cited in page 14.)

[28] C. Galletti; A. Parente; L. Tognotti. Numerical and experimental investigation of a mild combustion burner. *Combust. Flame.*, 151:649–664. (Cited in pages 14, 19, 20, 21, 35, 103 et 113.)

[29] Flox site. *www.flox.com*. (Cited in pages 15, 21 et 113.)

[30] L. Ballarino; M. Fantuzzi; M. Senarega. Low nox flameless burners: development and industrial applications. *Millenium Steel India*, 2008. (Cited in pages 15 et 21.)

[31] J. von Scheele; M. Gartz; R. Paul; M.T. Lantz; J.P. Riegert; S. Soderlund. Flameless oxyfuel combustion for increased production and reduced co_2 and no_x emissions. *Stahl und Eisen*, 128, 2008. (Cited in pages 15 et 21.)

[32] Linde Group. *www.lindeus.com*. (Cited in pages 15 et 21.)

[33] H. Kass; S. Tappe; H. Krautz. The combustion of dry lignite under oxy-fuel process conditions in a 0.5 mwth test plant. *Physics Procedia*, 2008. (Cited in page 15.)

[34] B.T. Burggraaf; B. Lewis; P.D.J. Hoppesteyn; N. Fricker; S. Santos; B.K. Slim. Towards industrial application of high efficiency combustion. *IFRF Combustion Journal*, 200704, 2008. (Cited in pages 17 et 21.)

[35] V. Battaglia; E. Malfa; M. Stazi; M. Fantuzzi. Flameless combustion modelling using detailed chemistry mechanism. *Proceedings of the European Combustion Meeting*, 2011. (Cited in pages 17, 21 et 35.)

[36] I.O. Awosope; F.C. Lockwood. Prediction of combustion and nox emission characteristics of flameless oxidation combustion. *IFRF Combustion Journal*, 200501, 2005. (Cited in pages 17, 21 et 35.)

[37] R. Weber; A. Verlaan; S. Orsino; N. Lallemant. On emerging furnace design methodology that provides substantial energy savings and drastic reductions in co2, co and nox emissions. *Journ. Inst. Ener.*, 72:77–83, 1999. (Cited in pages 17 et 21.)

[38] M. Mancini; R. Weber; U. Bollettini. Predicting nox emissions of a burner operated in flameless oxidation mode. *Proc. Combust. Inst.*, 29:1155–1163. (Cited in pages 17, 21, 25, 35 et 113.)

[39] N. Krishnamurthy; P.J. Paul; W. Blasiak. Studies on low-intensity oxy-fuel burner. *Proc. Combust. Inst.*, 32:3139–3146. (Cited in pages 18, 21, 25, 26, 35 et 113.)

[40] B.B. Dally; E. Riesmeierb; N. Peters. Effect of fuel mixture on moderate and intense low oxygen dilution combustion. *Combust. Flame.*, 137:418–431, 2004. (Cited in pages 19, 26, 28, 32, 35, 76 et 113.)

[41] G.G. Szegoe; B.B. Dally; G.J. Nathan. Scaling of nox emissions from a laboratory-scale mild combustion furnace. *Combust. Flame.*, 154:281–295, 2008. (Cited in pages 19, 21 et 113.)

[42] G.G. Szegoe; B.B. Dally; G.J. Nathan. Operational characteristics of a parallel jet mild combustion burner system. *Combust. Flame.*, 156:429–438, 2009. (Cited in pages 19, 20, 21 et 113.)

[43] B.B. Dally; A.N. Karpetis; R.S. Barlow. Structure of turbulent non-premixed jet flames in a diluted hot coflow. *Proc. Combust. Inst.*, 29:1147–1154, 2002. (Cited in pages 20, 21, 22, 29, 35, 38, 39 et 113.)

[44] M. Jianchun; L. Pengfei; B.B. Dally; R.A. Craig. Importance of initial momentum rate and air-fuel premixing on moderate or intense low oxygen dilution (mild) combustion in a recuperative furnace. *Ener. Fuel.*, 23:5349–5356, 2009. (Cited in page 20.)

[45] M. Jianchun; L. Pengfei; B.B. Dally; R.A. Craig. Numerical simulation of flameless premixed combustion with an annular nozzle in a recuperative furnace. *Chin. Journ. Chem. Eng.*, 18:10–17, 2010. (Cited in page 20.)

[46] M. Ayoub; C. Rottier; S. Carpentier; C. Villermaux A.M. Boukhalfa; D. Honore. An experimental study of mild flameless combustion of methane/hydrogen mixtures. *Intern. Journ. Hydr. Ener.*, 37:6912–6921. (Cited in page 20.)

[47] K. Maruta; K. Muso; K. Takeda; T. Niioka. Reaction zone structure in flameless combustion. *Proc. Combust. Inst.*, 28:2117–2123, 2000. (Cited in page 20.)

[48] M. Ihme; Y.C. See. Les flamelet modeling of a three-stream mild combustor: Analysis of flame sensitivity to scalar inflow conditions. *Proc. Combust. Inst.*, 33:1309–1317, 2011. (Cited in pages 20, 29, 32, 34, 35, 36, 37, 38, 39, 76 et 103.)

[49] M. Ihme; J. Zhang; G. He; B. Dally. Large-eddy simulation of a jet-in-hot-coflow burner operating in the oxygen-diluted combustion regime. *Flow Turbul. Combust.*, 89:449–464, 2012. (Cited in pages 20, 32, 34, 35, 38, 39, 76 et 103.)

[50] N. Peters. Laminar diffusion flamelet models in non-premixed turbulent combustion. *Prog. Ener. and Combust. Sci.*, 10:319–339, 2004. (Cited in pages 23, 25 et 31.)

[51] D.B. Spalding. Mixing and chemical reaction in steady confined turbulent flames. *Proc. Combust. Inst.*, 1970. (Cited in page 24.)

[52] B. Magnussen; B. Hjertager. On mathematical modeling of turbulent combustion with special emphasis on soot formation and combustion. *Int. Flame. Res. Found.*, 1989. (Cited in page 24.)

[53] H.I. Kassem; K.M. Saqr; H.S. Aly; M.M. Sies; M.A. Wahid. Implementation of the eddy dissipation model of turbulent non-premixed combustion in openfoam. *Intern. Commun. Heat Mass Transf.*, 38:363–367, 2011. (Cited in page 24.)

[54] B. Magnussen. Modeling of nox and soot formation by the eddy dissipation concept. *Proc. Combust. Inst.*, 1977. (Cited in page 24.)

[55] P.J. Coelho; N. Peters. Numerical simulation of a mild combustion burner. *Combust. Flame.*, 124:444–465, 2001. (Cited in pages 26, 27, 35, 38, 76 et 113.)

[56] H. Pitsch; M. Chen; N. Peters. Unsteady flamelet modeling of turbulent hydrogen/air diffusion flames. *Proc. Combust. Inst.*, 27:1057–1064. (Cited in page 26.)

[57] A.Y. Klimenko. Conditional moment closure and fluctuations of scalar dissipation. *Fluid Dynam.*, 28:630–637, 1993. (Cited in page 28.)

[58] R.W. Bilger. Conditional moment closure for turbulent reacting flow. *Phys. Fluids*, 5:436–444, 1993. (Cited in page 28.)

[59] M. Kostka A. Kronenburg. Modeling extinction and reignition in turbulent flames. *Combust. Flame.*, 143:342–356, 2005. (Cited in page 29.)

[60] S. Navarro-Martinez; A. Kronenburg. Les-cmc simulations of a lifted methane flame. *Proc. Combust. Inst.*, 32:1509–1516. (Cited in page 29.)

[61] S.H. Kim; K.Y. Huh; B. Dally. Conditional moment closure modeling of turbulent non-premixed combustion in diluted hot coflow. *Proc. Combust. Inst.*, 30:751–757. (Cited in pages 29 et 38.)

[62] C.D. Pierce; P. Moin. Progress-variable approach for large-eddy simulation of non-premixed turbulent combustion. *Jour. Fluid Mech.*, 504, 73-97. (Cited in pages 29 et 39.)

[63] M.Ihme and Y.C. See. Prediction of autoignition in alifted methane/air flame using an unsteady flamelet/progress variable model. *Combust. Flame.*, 157:1850–1862, 2010. (Cited in pages 29 et 103.)

[64] O. Gicquel; N. Darabiha; D. Thevenin. Laminar premixed hydrogen/air counterflow flame simulations using flame prolongation of ildm with differential diffusion. *Proc. Combust. Inst.*, 28:1901–1908, 2000. (Cited in pages 30, 43 et 45.)

[65] B. Fiorina; R. Baron; L. Gicquel; D. Thevenin; S. Carpentier; N. Darabiha. Modeling non-adiabatic partially premixed flames using flame-prolongation of ildm. *Combust. Theory Modell.*, 7:449–470, 2003. (Cited in pages 30, 43 et 104.)

[66] J. Galpin; C. Angelberger; A. Naudin; L. Vervisch. Large-eddy simulation of h2-air autoignition using tabulated chemistry. *Turb. Journ.*, 9:1–21, 2008. (Cited in pages 30 et 31.)

[67] J. Van Oijen; F. Lammers; L. DeGoey. Modeling of complex premixed burner systems by using flamelet generated manifolds. *Combust. Flame*, 127:2124–2134, 2001. (Cited in page 30.)

[68] J. Van Oijen; L. DeGoey. Modelling of premixed counterflow flames using the flamelet-generated manifold method. *Combust. Theo. Model.*, 6:463–478, 2002. (Cited in page 30.)

[69] J. Van Oijen; L. DeGoey. A numerical study of confined triple flames using a flamelet-generated manifold. *Combust. Theo. Model.*, 8:141–163, 2004. (Cited in page 30.)

[70] A.W. Vreman; B.A. Albrecht; J. van Oijen; L.P.H. de Goey; R.J.M Bastiaans. Premixed and nonpremixed generated manifolds in large-eddy simulation of sandia flame d and f. *Combust. Flame.*, 153:394–416, 2008. (Cited in pages 30, 57, 59, 74, 76, 90, 104 et 105.)

[71] L. Vervisch; R. Hauguel; P. Domingo; R. Rullaud. Three facets of turbulent combustion modeling: Dns of premixed v-flame, les of lifted nonpremixed flame and rans of jet-flame. *Journ. Turb.*, 5:1–36, 2004. (Cited in pages 30, 47, 48 et 113.)

[72] K.N.C. Bray. The challenge of turbulent combustion. *Proc. Combust. Inst.*, 26:1–26, 1996. (Cited in page 30.)

[73] J.B. Michel; O. Colin; C. Angelberger; D. Veynante. Using the tabulated diffusion flamelet model adf-pcm to simulate a lifted methane-air jet flame. *Combust. Flame.*, 156:1318–1331, 2009. (Cited in pages 31, 32, 38, 39, 41 et 52.)

[74] B. Fiorina; O. Gicquel; L. Vervisch; S. Carpentier; N. Darabiha. Approximating the chemical structure of partially premixed and diffusion counterflow flames using fpi flamelet tabulation. *Combust. Flame.*, 140:147–160, 2005. (Cited in pages 31 et 59.)

[75] P. Domingo; L. Vervisch; D. Veynante. Large-eddy simulation of a lifted methane jet flame in a vitiated coflow. *Combust. Flame.*, 152:415–432, 2008. (Cited in page 31.)

[76] J.B. Michel; O. Colin; D. Veynante. Modeling ignition and chemical structure of partially premixed turbulent flames using tabulated chemistry. *Combust. Flame.*, 152:80–99, 2008. (Cited in pages 31, 32, 38, 39, 43, 51 et 52.)

[77] J. Tillou. Phd thesis. *Ecole Centrale Paris*, 2013. (Cited in pages 32 et 41.)

[78] J. Tillou; J.B. Michel; C. Angelberger; D. Veynante. Assessing les models based on tabulated chemistry for the simulation of diesel spray combustion. *Combust. Flame.*, 161:525–540, 2014. (Cited in page 32.)

[79] O. Colin; F. Ducros; D. Veynante; T. Poinsot. A thickened flame model for large eddy simulations of turbulent premixed combustion. *Phys. Fluid.*, 12:1843–1863, 2000. (Cited in page 32.)

[80] S. Richard; O. Colin; O. Vermorel; A. Benkenida; C. Angelberger; D. Veynante. Towards large eddy simulation of combustion in spark ignition engines. *Proc. Combust. Inst.*, 31:3059–3066, 2007. (Cited in page 32.)

[81] R.Vicquelin. Calcul les d'une combustion sans flamme. *CERFACS*, Master of Science Thesis, 2006. (Cited in page 33.)

[82] G.P. Smith; D.M. Golden; M. Frenklach; N.W. Moriarty; B. Eiteneer; M. Goldenberg; C.T. Bowman; R.K. Hanson; S. Song; W.C. Jr. Gardiner; V.V. Lissianski; Z. Qin. http://www.me.berkely.eud/gri_mech/. (Cited in pages 33, 44 et 57.)

[83] K. Netzell; H. Lehtiniemi; F. Mauss. Calculating the soot particle size distribution function in turbulent diffusion flames using a sectional method. *Proc. Combust. Inst.*, 31:667–674, 2007. (Cited in page 34.)

[84] A. Verissimo; R. Oliveira; P.J. Coelho; M. Costa. Numerical simulation of a small-scale mild combustor. *Journ. Phys.*, 395, 2012. (Cited in pages 35 et 71.)

[85] F.C. Christo; B.B. Dally. Modeling turbulent reacting jets issuing into a hot and diluted coflow. *Combust. Flame*, 142:117–129, 2005. (Cited in page 38.)

[86] A.S. Verissimo; A.M.A. Rocha; M. Costa. Importance of the inlet air velocity on the establishment of flameless combustion in a laboratory combustor. *Exp. Therm. Fluid Sci.*, 44:75–81, 2012. (Cited in pages 38, 63 et 64.)

[87] S.B. Pope. Pdf methods for turbulent reactive flows. *Prog. Ener. Combust. Sci.*, 11:119–192, 1985. (Cited in page 38.)

[88] A. Cuoci; A. Frassoldati; A. Stagni; T. Faravelli; E. Ranzi; G. Buzzi-Ferraris. Numerical modeling of nox formation in turbulent flames using a kinetic post−processing technique. *Ener. Fuel.*, 27:1104–1122, 2013. (Cited in pages 38, 68, 71 et 95.)

[89] J. Smagorinsky. General circulation experiments with the primitive equations. *Mon. Wea. Rev.*, 91:99–164, 1963. (Cited in pages 38 et 40.)

[90] A. Eyssartier; B. Cuenot; L. Gicquel; T. Poinsot. Using les to predict ignition sequences and ignition probability of turbulent two-phase flames. *Combust. Flame.*, 160:1191–1207, 2013. (Cited in page 38.)

[91] S. Hermeth; G. Staffelbach; L. Gicquel; T. Poinsot. Les evaluation of the effects of equivalence ratio fluctuations on the dynamic flame response in a real gas turbine combustion chamber. *Proc. Combust. Inst.*, 34:3165–3173, 2013. (Cited in page 38.)

[92] C. Duwig; R.Z. Szasz; L. Fuchs. Modeling of flameless combustion using large eddy simulation. *Proc. GT2006, ASME Turbo Expo Power for Land, Sea and Air*, GT2006-90063, 2006. (Cited in pages 38, 39 et 76.)

[93] K. Wang; G. Ribert; P. Domingo; L. Vervisch. Self-similar behavior and chemistry tabulation of burnt-gas diluted premixed flamelets including heat-loss. *Combust. Theor. Model.*, 14:541–570, 2012. (Cited in pages 39 et 41.)

[94] da Cruz A.P. Jay S. Colin, O. Detailed chemistry-based auto-ignition model including low temperature phenomena applied to 3-d engine calculations. *Proc. Combust. Inst.*, 30:2649–2656, 2005. (Cited in page 41.)

[95] S. Chevillard; J.B. Michel; C. Pera; J. Reveillon. Validation of turbulent combustion models based on homogeneous-reactor tabulated chemistry. (Cited in page 48.)

[96] E.M. Doran; H. Pitsch; D.J. Cook. A priori testing of a two-dimensional unsteady flamelet model for three-feed combustion systems. *Proc. Combust. Inst.*, 34:1317–1324, 2013. (Cited in page 48.)

[97] B. Fiorina; O. Gicquel; L. Vervisch; S. Carpentier; N. Darabiha. Premixed turbulent combustion modeling using tabulated detailed chemistry and pdf. *Proc. Combust. Inst.*, 30:867–874, 2005. (Cited in page 49.)

[98] V. Moureau; G. Lartigue; Y. Sommerer; C. Angelberger; C. Colin; T. Poinsot. High-order methods for dns and les of compressible multi-component reacting flows on fixed and moving grids. *J. Comput. Phys.*, 202:710–736, 2005. (Cited in page 50.)

[99] J.B. Michel; O. Colin; C. Angelberger. On the formulation of species reaction rates in the context of multi-species cfd codes using complex chemistry tabulation techniques. *Combust. Flame.*, 157:701–714, 2010. (Cited in pages 50 et 51.)

[100] Cosilab. rotexo software, bochum. 2010. (Cited in page 51.)

[101] N. Peters. Turbulent combustion. *Cambridge University Press*, 2000. (Cited in pages 51, 52, 55 et 78.)

[102] J. Luche. Luche elaboration of reduced kinetic models of combustion. application to a kerosene mechanism. *PhD Thesis, Université d'Orléans*, 2003. (Cited in page 51.)

[103] R.S. Barlow; J.H. Frank. Effects of turbulence on species mass fractions in methane air jet flames. *Proc. Combust. Inst.*, 27:1087–1095, 1998. (Cited in page 56.)

[104] W. Meier; R.S. Barlow; Y.L. Chen. Raman/rayleigh/lif measurements in a turbulent ch4/h2/n2 jet diffusion flame: experimental techniques and turbulenceâchemistry interaction. *Combust. Flame.*, pages 326–343, 2000. (Cited in page 56.)

[105] C. Schneider; A. Dreizler; J. Janicka; E. Hassel. Flow field measurements of stable and locally extinguishing hydrocarbon-fuelled jet flames. *Combust. Flame*, 135:185–190, 2003. (Cited in page 56.)

[106] A. Smirnov; S. Shi; I. Celik. Random flow generation technique for large-eddy simulations and particle-dynamics modeling. *J. Fluids Eng.*, 123:359–371, 2001. (Cited in page 57.)

[107] R. Kraichnan. Diffusion by a random velocity field. *Phy. Fluids.*, 13:22–31, 1970. (Cited in page 57.)

[108] T. Poinsot; S.K. Lele. Boundary conditions for direct simulations of compressible viscous flow. *J. Comput. Phys.*, 101:104–129, 1992. (Cited in page 57.)

[109] P.J. Coelho; O.J. Teerling; D. Roekaerts. Spectral radiative effects and turbulence/radiation interaction in a non-luminous turbulent jet diffusion flame. *Combust. Flame.*, 133:75–91, 2003. (Cited in pages 57, 91 et 93.)

[110] P. Sagaut. Large eddy simulation for incompressible flows. *Springer Berlin Heidelberg*, 1998. (Cited in page 68.)

[111] P.E. Vervisch; J.B. Michel; O. Colin; N. Darabiha. No relaxation approach (nora) to predict thermal no in combustion chamber. *Combust. Flame.*, 158:80–99, 2011. (Cited in pages 75, 76, 77, 79, 86, 91, 100 et 104.)

[112] M. Ihme; H. Pitsch. Modeling of radiation and nitric oxide formation in turbulent nonpremixed flames using a flamelet/progress variable formulation. *Phys. Fluids*, 20:055110, 2008. (Cited in pages 75, 76, 79, 80, 86, 89, 93 et 100.)

[113] J. Liang. Chemical modeling for air resources fundamentals, applications, and corroborative analysis. *Elsevier.Inc*, ISBN: 978-0-12-408135-2, 2013. (Cited in page 76.)

[114] P.J. Crutzen. The role of no and no2 in the chemistry of the troposphere and stratosphere. *Ann. Rev. Earth Planet. Sci.*, 7:443–472, 1979. (Cited in page 76.)

[115] Y.B. Zeldovich. *Acta. Physicochim.*, 21:577–628, 1946. (Cited in page 76.)

[116] C.P. Fenimore. Formation of nitric oxide in premixed hydrocarbon flames. *Symp. (Int.) Combust.*, 13:373–380, 1971. (Cited in page 76.)

[117] J. Miller; C. Bowman. Mechanism and modeling of nitrogen chemistry in combustion. *Prog. Energy Combust. Sci.*, 15:287–338, 1989. (Cited in page 76.)

[118] C.P. Fenimore. The ratio no2-no in fuel-lean flames. *Combust. Flame.*, 25:85–90, 1975. (Cited in page 76.)

[119] B.T. Zoller; J.M. Allegrini; U. Maas: P. Jenny. Pdf model for no calculations with radiation and consistent no-no2 chemistry in non-premixed turbulent flames. *Combust. Flame.*, 158:1591–1601, 2011. (Cited in pages 76, 79, 82, 91, 93, 100 et 103.)

[120] C. Locci; O. Colin; J.B. Michel. Large eddy simulations of a small-scale flameless combustor by means of diluted homogeneous reactors. (Cited in pages 76, 77, 91, 94, 95 et 104.)

[121] S.H. Kim; K.Y. Huh. Second-order conditional moment closure modeling of turbulent piloted jet diffusion flames. *Combust. Flame.*, 138:336–352, 2004. (Cited in page 76.)

[122] S. Navarro-Martinez; A. Kronenburg. Les-cmc simulations of a turbulent bluff-body flame. *Proc. Combust. Inst.*, 31:1721–1728, 2007. (Cited in page 76.)

[123] S.C. Hill; L.D. Smoot. Modeling of nitrogen oxides formation and destruction in combustion systems. *Prog. Energ. Combust.Sci.*, 26:417–458, 2000. (Cited in page 76.)

[124] F. Biagioli; F. Guthe. Effect of pressure and fuelâair unmixedness on nox emissions from industrial gas turbine burners. *Combust. Flame.*, 151:274–288, 2007. (Cited in page 76.)

[125] A. Frassoldati; S. Frigerio; E. Colombo; F. Inzoli; T. Faravelli. Determination of nox emissions from strong swirling confined flames with an integrated cfd-based procedure. *Chem. Eng. Sci.*, 60:2851–2869, 2005. (Cited in page 76.)

[126] G. Godel; P. Domingo; L. Vervisch. Tabulation of no_x chemistry for large-eddy simulation of non-premixed turbulent flames. *Proc. Combust. Inst.*, 32:1555–1561, 2009. (Cited in page 76.)

[127] V. Knop; A. Nicolle; O. Colin. Modelling and speciation of nitrogen oxides in engines. *Proc. Combust. Inst.*, 34:667–675, 2013. (Cited in pages 76, 79 et 91.)

[128] C. Bowman; R. Hanson; D. Davidson; W. Gardiner; V. Lissianski; G. Smith; D. Golden; M. Frenklach; M. Goldenberg. http://www.me.berkeley.edu/gri_mech/. 1995. (Cited in pages 77, 80, 81 et 90.)

[129] C. Pierce; P. Moin. A dynamic model for subgrid scale variance and dissipation rate of a conserved scalar. *Phys. Fluids*, 10:3041–3044, 1998. (Cited in page 77.)

[130] D. Poitou; M.E. Hafi; B. Cuenot. Analysis of radiation modeling for turbulent combustion : development of a methodology to couple turbulent combustion and radiative heat transfer in les. *J. Heat Transfer*, 133:062701, 2010. (Cited in pages 78, 79 et 103.)

[131] D. Poitou; J. Amaya; M.E. Hafi; B. Cuenot. Analysis of the interaction between turbulent combustion and thermal radiation using unsteady coupled les/dom simulations. *Combust. Flame.*, 159:1605–1618, 2012. (Cited in pages 78, 79, 103 et 107.)

[132] K.A. Jensen; J. Ripoll; A. Wray; D. Joseph; M.E. Hafi. On various modeling approaches to radiative heat transfer in pool fires. *Combust. Flame.*, 148:263–279, 2007. (Cited in page 78.)

[133] D. Joseph; M.E. Hafi; R. Fournier; B. Cuenot. Comparison of three spatial differencing schemes in discrete ordinates method using three-dimensional unstructured meshes. *Int. J. Therm. Sci.*, 44:851–864, 2005. (Cited in page 78.)

[134] A. Soufiani; E. Djavdan. A comparison between weighted sum of gray gases and statistical narrow-band radiation models for combustion applications. *Combust. Flame.*, 97:240–250, 1994. (Cited in pages 79 et 103.)

[135] M. Roger; C.B.D. Silva; P.J. Coelho. Analysis of the turbulenceâradiation interactions for large eddy simulations of turbulent flows. *Int. J. Heat Mass Transf.*, 52:2243–2254, 2009. (Cited in page 79.)

[136] M. Roger; C.B.D. Silva; P.J. Coelho. The influence of the non-resolved scales of thermal radiation in large eddy simulation of turbulent flows. a fundamental study. *Int. J. Heat Mass Transf.*, 53:2897–2907, 2010. (Cited in page 79.)

[137] H. Pitsch. Flamemaster, a c++ computer program for od combustion and 1d laminar flame calculations. (Cited in page 81.)

[138] M. Nishioka; Y. Kondoh; T. Takeno. Behavior of key reactions on no formation in methane-air flames. *Proc. Combust. Inst.*, 26:2139–2145, 1996. (Cited in page 86.)

[139] R.J. Kee; F.M. Rupley; J.A. Miller. Chemkin-ii : a fortran chemical kinetics package for the analysis of gas phase chemical kinetics. *Sandia Nation. Labor. Report.*, pages SAND89–8009B, 1994. (Cited in page 90.)

[140] P.J. Coelho. Numerical simulation of the interaction between turbulence and radiation in reactive flows. *Progr. Energy Combust. Sci.*, 33:311–383, 2007. (Cited in page 91.)

[141] L. Martinez; J.B. Michel; S. Jay; O. Colin. Evaluation of different tabulation techniques dedicated to the prediction of the combustion and pollutants emissions on a diesel engine with 3d cfd. *SAE*, 2013-01-1093, 2013. (Cited in page 91.)

[142] J. Lamouroux; M. Ihme: B. Fiorina; O. Gicquel. Tabulated chemistry approach for diluted combustion regimes with internal recirculation and heat losses. *Combust. Flame*, in press, 2014. (Cited in page 95.)

[143] A. Nicolle; P. Dagaut. Occurrence of no-reburning in {MILD} combustion evidenced via chemical kinetic modeling. *Fuel*, 85:2469–2478, 2006. (Cited in page 97.)

[144] M. Braun-Unkhoff; P. Frank; S. Koger; W. Leuckel; D. Stapf. Evaluation of no x reburning models under large-scale conditions. *Clean Air*, 3:273–303, 2002. (Cited in page 97.)

[145] F. Liu; H. Guo; G.J. Smallwood M. El Hafi. Effects of gas and soot radiation on soot formation in counterflow ethylene diffusion flames. *J. Quant. Spectrosc. Radiat. Transfer*, 84:501–511, 2004. (Cited in page 107.)